

A Tethered And Navigated Air Blimp (TANAB) for observing the microclimate over a complex terrain

Response to Reviewers

Nambiar et al.

September 4, 2019

Dear Dr. Mike Rose,

Thank you for the assessment of our manuscript and encouraging submission of a revised manuscript after incorporating reviewer comments. We are pleased to inform you that we have improved the manuscript by addressing all reviewer comments to the best of our ability. Please see below our point-by-point responses. In brief, we have elaborated and reported the wind tunnel calibration of the ultrasonic anemometer in more detail, analyzed the wind measurements in a new *along-wind* reference frame, performed and reported FLIR camera calibration, and enhanced the literature review by adding more text and references relevant to the field. We hope that this new revised version will satisfy the journal requirements and standards. We will be pleased to include any more changes toward the improvement of the manuscript

Regards,

Amir A. Aliabadi

On behalf of all co-authors

Note: The reviewer comments are listed in **red font**, our responses to reviewer comments are listed in black font, and the changes in the manuscript are listed in **blue font**.

1 Reviewer 1

1. This paper is not suitable for publication in its present form due to two significant shortfalls.

Response: Thank you for your constructive review. The concerns have been addressed to the best of our ability to improve the quality of the manuscript. We hope this revised version will be suitable for publication.

2. Lack of suitable literature review outside of the authors' own papers and standard atmospheric boundary-layer (ABL) references. Specifically the wealth of literature on near-surface micro-meteorological observations from tethered systems is missing, be they via kite, tethered balloon, or kite-balloon. BL Profile data have been collected in this manner for over a century, and even the more exacting challenge of measuring ABL turbulence has a history starting in the 1970s.

Response: We appreciate your comments. We have included a detailed literature survey and references in the revised version of the manuscript as the following in Sect. 1.1.

Airborne systems are increasingly being used for atmospheric measurements (Martin et al., 2011; Palomaki et al., 2017) although recently their use is being regulated more restrictively. For instance, rotary or fixed-wing drones are not permitted to fly in complex environments such as busy urban areas and airports. On the other hand, tethered balloon-based atmospheric measurement techniques have been used widely for obtaining the turbulence structure as well as the mean vertical profiles of the ABL in complex environments (Thompson, 1980). One of the main advantages of a tethered balloon system is its ability to profile a significant portion of the planetary boundary layer starting from the surface, which is not possible or economical by ground-based or aircraft-based atmospheric measurement techniques (Egerer et al., 2019). The use of ultrasonic anemometers in tethered balloons have been reported in many studies (Stevens et al., 2013; Canut et al., 2016). In comparison, one of the disadvantage of Pitot tubes is their inability to measure the low wind speeds. So they require a fast flying probe which cannot fly in a complex environment for safety and logistic reasons. Ultrasonic anemometers, on the other hand, are popular because of their continuous measurement characteristics, high accuracy, and their ability to be levitated to measure low velocities (Martikainen et al., 2010; Casten et al., 1995). In addition, studies have shown that tethered balloon-based probes can be used for continuous measurement of the important parameters in the ABL without influencing the flow compared to tower-mounted instruments, where the tower structure can perturb the flow measurement, or presence of complex topography or nearby buildings that can influence the measurement (Haugen et al., 1975; Stevens et al., 2013).

Tethered balloon-borne atmospheric turbulence measurements have a long history of observations over the land (Smith, 1961) and sea (Thompson, 1972) to measure fluxes of heat and moisture at heights up to a few hundred metres. The most notable tethered balloon systems deployed

collected data in campaigns in the late 1960s and 1970s including the Barbados Oceanographic and Meteorological Experiment (BOMEX) (Davidson, 1968; Garstang and La Seur, 1968; Friedman and Callahan, 1970), the Joint Air-Sea Interaction (JASIN) Experiment (Pollard, 1978), and the Global Atmospheric Research Programme (GARP) Atlantic Tropical Experiment (GATE) (Berman, 1976). In BOMEX a tethered balloon system was operated from the deck, which measured temperature, wind, and humidity continuously, at different levels in the range of 0 to 600 m in the ocean area north and east of the Island of Barbados. In JASIN tethered balloons were used to measure the structure of ABL to understand the air-sea interaction in the North Atlantic. In the recent past, tethered balloon systems have been used in Boundary-Layer Late Afternoon and Sunset Turbulence (BLLAST) field campaign that was conducted in southern France (Lothon et al., 2014). Canut et al. (2016) used an ultrasonic anemometer mounted on a tethered balloon system for turbulent flux and variance measurements. Egerer et al. (2019) used the BELUGA (Balloon-borne modular Utility) tethered balloon system for profiling the lower Atmosphere by turbulence and radiation measurements in the Arctic.

3. More recently, ultrasonic anemometers (rather than say Gill anemometers) on tethered systems were first made in the 1990s, and in the last 5 years remotely pilot aircraft systems (RPAS) have become the standard platforms for ABL turbulence, and this has been reported in dozens of publications.

Response: Thank you for your comments. We have incorporated more information about the use of ultrasonic anemometers on airborne measurements and the associated advantages. Please refer to the previous comment.

4. Lack of instrumental rigour. Both the ultrasonic anemometer data and the remote sensed surface temperatures are not suitably calibrated. I could not find any mention of the means to convert the anemometer wind measurements of $[u,v,w]$ into the reference of the earth: this requires a very significant effort in both analysis of the platform movement (via Inertial Navigation Unit (IMU), not solely from three-axes tilt) and calibration of the resulting variances and co-variances. The wind tunnel data are not suitable for this analysis as both units (I assume) were static.

Response: Thank you for pointing out the fact that the ultrasonic anemometer data calibration section were missing important details. Now we have added the gondola motion as well as the calibration experimental set-up in detail in Sect. 2.1 and Sect. 3.1 of the revised manuscript, respectively. We have considered separate calibration equations for both mean and turbulence statistics of the flow. We did not require to convert TriSonicaTM Mini's measurement of flow statistic to a fixed reference frame of the earth. We only required to understand the flow statistics in the *along-wind*, *cross-wind*, and *vertical-wind* directions. As shown below, the gondola turns against the mean wind most of the time and it is level within $\pm 5^\circ$ in both the pitch and roll angles more than 90% of the time. The gondola only rotates in the yaw direction when the main wind direction changes. This enables us to interpret the flow statistics in the three directions mentioned. Sect. 2.1 of the manuscript now contains the following text.

The gondola is a part of the tethered balloon system controlled by multiple ropes on the ground. The acting forces on the system are 1) the lift force due to the helium-filled balloon, 2) the force of gravity, 3) the tension forces due to the ropes, and 4) the drag forces due to the wind. In the

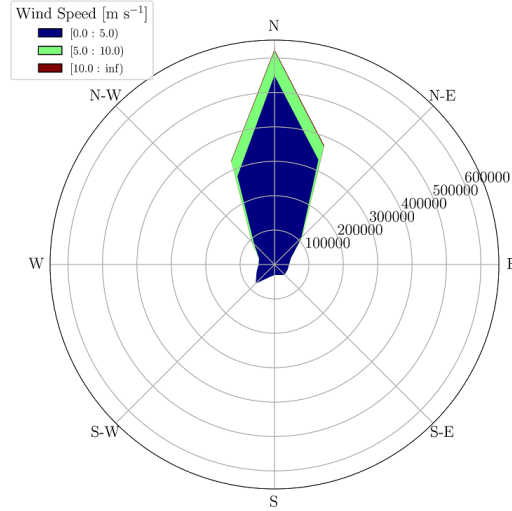


Figure 1: The wind-rose corresponding to 56 hours of flight, reported in the local coordinate system of the sensor. The numbers on the plot indicate sampling records collected at 10 Hz.

absence of the drag force the remaining forces are acting in the vertical direction and the system ascends up or down, but the presence of the drag force displaces the system in the horizontal direction. At all times these forces are balanced so that the TANAB is in a quasi-stationary position.

The balloon is equipped with a net that helps facing the balloon against the main wind direction at any moment. The net guides the air on one side, and the pressure force stops the balloon from rotating. In case of wind direction changing, the pressure force builds up on the net creating a torque around the centre of rotation that repositions the balloon facing the main wind. Up to three ropes are used to tether the balloon to help with stabilizing the system, especially during high winds associated with convective boundary layers. The ropes, however, impose extra weight on the system so that the vertical range of the system reduces when three ropes are used as opposed to one.

The evidence that the net mechanism succeeds in aligning the balloon against the main wind direction can be found in Fig. 1. The wind-rose shows the wind direction records by TriSonica™ Mini (at TriSonica™ Mini's coordinate) for over 56 hr of flight. According to the wind-rose the gondola mostly faces against the main wind direction because wind direction is recorded from the local north direction most of the time. Note that TriSonica™ Mini's north axis is the sensor local coordinate. If desired, this reading can be converted into the fixed inertial body of reference. For this to occur, the sensor yaw, pitch, and roll angles need to be used. This conversion, however, was not desired in the present analysis.

Figure 2 (left) shows the balloon operation in an unstable atmosphere with high winds when three ropes are used to stabilize it. A sudden drag force on the gondola may drive the system out of its stable position momentarily. Hence it may affect the quality of measurements by creating instabilities. Such phenomenon can be prevented by deploying extra ropes connecting the gondola



Figure 2: TANAB at different atmospheric stability conditions; left: TANAB and three stabilizing ropes deployed at the mining facility; right: TANAB and two stabilizing ropes deployed at the mining facility.

directly to ground operators. The tension in these ropes balances the sudden drag force exerted on the system. This arrangement places the gondola in a quasi-stationary position in the air that indeed helps the stability of measurement in gusty conditions. Figure 2 (right) shows the balloon operation in a stable atmosphere with low winds when only two ropes are used to stabilize it.

A T-connector connects the balloon to the gondola using ropes allowing the gondola to hang freely while minimizing the pitch and roll angles to result in better measurements from a levelled gondola. Figure 3 shows the distributions for pitch and roll angles recorded by TriSonicaTM Mini’s compass over 56 flight hours. According to the bar charts, the gondola is level within $\pm 5^\circ$ of pitch and roll angles more than 90% of the time. The gondola only rotates in the yaw direction when the main wind direction changes. The gondola is positioned 2 m below the balloon, so the effects of the balloon motion on the gondola are reduced.

Figure 4 shows the wind tunnel used for ultrasonic anemometer calibration onboard of TANAB, which is an open circuit tunnel designed for turbulent boundary layer research. The reference sensor for calibration was a pitot tube which was used to calibrate an R.M. YOUNG 81000 ultrasonic anemometer and the ultrasonic anemometer onboard of TANAB while all three components of wind were considered from the R.M. YOUNG 81000 ultrasonic anemometer. The azimuth angle, elevation angle, and wind levels were changed, independently, to derive calibration coefficients for both mean and turbulence statistics as measured by the TriSonicaTM Mini and calibrated against the R.M. YOUNG 81000. Figures 5 and 6 show the set-up for R.M. YOUNG 81000 and gondola calibration, respectively. Note that the gondola was hung from the tunnel with rope attachments to simulate its motion in the real atmosphere. Section 3.1 of the manuscript now contains the following text.

All the experiments were conducted in the University of Guelph’s wind tunnel, which is an open circuit tunnel designed for turbulent boundary layer research. The cross sectional area is 1.2 m \times 1.2 m. The tunnel is 10 m long. The tunnel’s air speed is controlled by a gauge that sets the fan speed. The tunnel achieves wind speeds up to 10 m s⁻¹. The turbulence intensity is typically

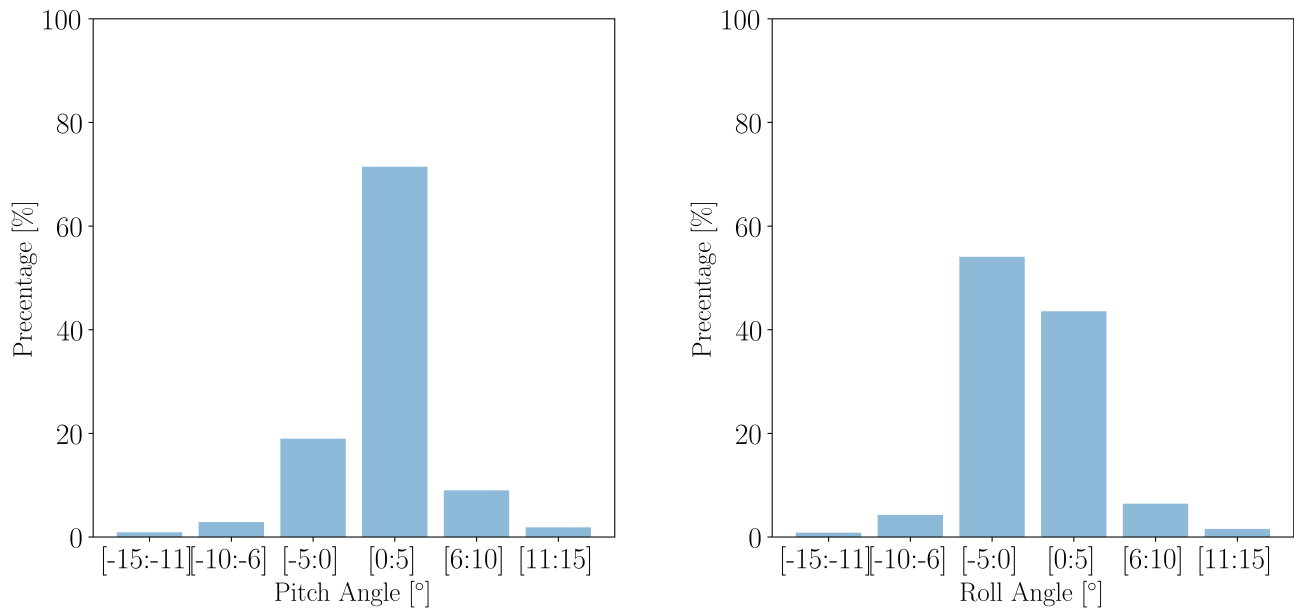


Figure 3: Left: the distribution of pitch angles recorded by TriSonicaTM Mini's compass; right: the distribution of roll angles recorded by TriSonicaTM Mini's compass.

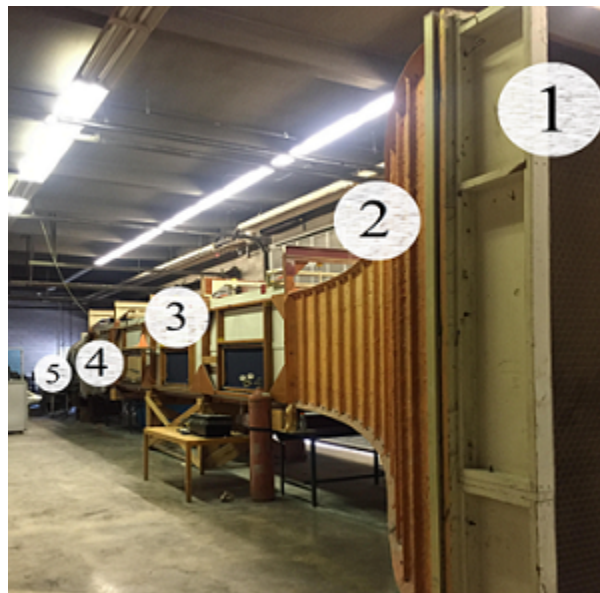


Figure 4: Wind tunnel at the University of Guelph: 1=honeycomb, 2=contraction, 3=test section, 4=diffuser, and 5=fan.



Figure 5: The view of the R.M. YOUNG 81000 (left) and pitot tube (right) at the wind tunnel.



Figure 6: The view of gondola (left) and pitot tube (right) at the wind tunnel.

less than 2 % if no roughness blocks are placed upstream of the flow. The Reynolds number characterizes the turbulence level of the fluid flow and is defined as the ratio of the inertial to viscous forces given by $Re = \frac{\rho \times U \times L}{\mu}$, where U is the flow velocity, L is the characteristic length scale of the system (commonly, the hydraulic diameter of the wind tunnel), and μ and ρ are the dynamic viscosity and density of the fluid, respectively. In the present study, the wind tunnel's Re number varied between 150,000 and 1,100,000. Considering the size of the wind tunnel, it is capable to generate eddies as large as its physical dimensions.

The performance of the gondola (or the effects of the frame on TriSonica™ Mini measurements) in reading the mean and turbulence statistics of the flow field is studied with respect to the R.M. YOUNG 81000 anemometer, which is already calibrated, and used for cross comparison to derive the calibration coefficients for the TriSonica™ Mini using line fits. By adding multiple degrees of freedom, the set-up for this test was designed to further simulate the gondola's movements in real cases. The gondola is attached to the ceiling with tow ropes (featuring the ropes to the balloon) and a single rope to the bottom floor (resembling the ground controller). Now, the gondola faces the main flow (as it does in the real atmosphere), but it has some degrees of freedom to slightly wobble. The azimuth angle, elevation angle, and wind levels were changed, independently, to derive calibration coefficients for both mean and turbulence statistics as measured by the TriSonica™ Mini and calibrated against the R.M. YOUNG 81000. Both sensors were set up at similar airflow condition while wind speed was varied at few wind levels in the range 2-10 m s⁻¹. At each wind speed level, data recording continued for 5 min. Each recording was time averaged to calculate mean and turbulence statistics.

5. Similarly, the over-complex calibration of the FLIR camera's land Surface Temperature (LST) using Plank's Law is inappropriate. These cameras are bolometers, and give an output with a response related to the overall incoming thermal radiation according to Stefan-Boltzmann law, which is far simpler and with fewer coefficients. It is then a matter of calibrating the camera against a known temperature with a known emissivity: using a certificated thermometer in a large lake for instance.

Response: Thank you for your comments regarding the operation and use of the thermal camera onboard the TANAB. The DJI Zenmuse XT was included in the TANAB platform to record Earth surface temperature variation within the mining facility perimeter. Using the default camera constants does not provide absolute surface temperature measurements. Therefore, if one does not calibrate the sensor with known surface temperatures, the relative surface temperatures of the mine, tailings pond, the facility to the East of the mine, and the forest beyond the facility, will be reported. To be able to measure absolute temperatures, we have calibrated the camera constants against known surface temperatures. This method has improved the accuracy of our method. In addition, we added more literature review to address the use of uncooled thermal cameras for numerous similar applications. The following text has been added in the revised manuscript in Sect. 1.1.

From literature, the use of uncooled thermal cameras for quantification of relative surface temperatures have been documented many times for a variety of applications. Improvements in Unmanned Aerial System (UAS) and thermal imaging technology have allowed waterbodies to be mapped with a high spatiotemporal resolution. Specifically, understanding the spatial and temporal vari-

ation of thermal plumes from sources, such as influent stormwater or geothermal activity, on waterbodies is of significant importance for many hydrological applications (Baker et al., 2019). Water temperature is also a parameter used to quantify water quality as it is known to impact aquatic organisms (Caldwell et al., 2019). Localized areas of higher surface water temperature were effectively identified by using a DJI Zenmuse XTR uncooled thermal camera without additional radiometric calibration (Caldwell et al., 2019). Mallast and Siebert (2019) utilized a UAS-based FLIR Tau2 thermal camera to spatially map submarine groundwater discharge in the Dead Sea, Israel. The intrusion of cooler groundwater rising to the surface of the Dead Sea was captured by the thermal camera, and the variation of spatial perturbations with respect to time were represented. Similarly, uncooled microbolometer thermal imaging systems have been employed to quantify the spatial distribution of surface temperatures of glaciers (Aubry-Wake et al., 2015). This data can be used to increase the accuracy of energy budget models developed for glaciers (Aubry-Wake et al., 2015). Luo et al. (2018) used a Zenmuse XT uncooled thermal camera to spatially map surface temperature variations of permafrost slopes. Understanding the variation of surface temperature of permafrost slopes is very important for infrastructure management and planning of railways, pipelines, and roads constructed on permafrost (Luo et al., 2018).

Uncooled microbolometer thermal cameras have also been used extensively in the agricultural industry, especially in the emerging precision agriculture sector. Poblete et al. (2018) used a FLIR Tau 2 640 uncooled thermal camera to quantify plant water stress which is a measure of water availability for crops (Alderfasi and Nielsen, 2001). A FLIR Tau 2 640 uncooled microbolometer thermal camera was used by Cao et al. (2018) to image plant leaf temperatures to identify *Sclerotinia sclerotiorum* on the leaves of oilseed rape plants.

UAS-based microbolometer thermal imaging cameras have also been noted to have some niche applications in literature. For example, Murray et al. (2018) successfully conducted a study using the FLIR Systems Vue Pro to identify relative temperature variations between human remains and the surrounding environment. Gallardo-Saavedra et al. (2018) detailed numerous studies where uncooled microbolometer thermal cameras were used to inspect photovoltaic panels and quantify performance of photovoltaic plants. Zhong et al. (2019) completed a study using a FLIR Tau 2 640 to assist in identifying pipeline leakages within a district heating system.

It is well reported in literature that uncooled microbolometer temperature measurements are impacted by variation of sensor and camera/ambient temperatures (FLIR-Systems, 2012; Budzier and Gerlach, 2015; Lin et al., 2018). Considering these three sources of measurement error, it is not acceptable to consider calculated surface temperatures from uncooled microbolometers to be absolute without a calibration. Conversely, cooled thermal cameras are designed to measure temperatures with a high degree of accuracy such that absolute temperatures could be determined (Ribeiro-Gomes et al., 2017). Although cooled thermal cameras are very accurate, they are significantly heavier, more expensive, and require more power to operate (Sheng et al., 2010; Ribeiro-Gomes et al., 2017). As a result, cooled thermal cameras are not commonly used for small UAS (such as drones and blimps) (Sheng et al., 2010).

The following information has been added in Sect. 2.3.1 of the revised manuscript.

Although the camera utilized in this paper used an uncooled microbolometer to record thermal

energy, it was calibrated against known surface temperatures. The use of the Stefan-Boltzmann Law is not applicable because the DJI Zenmuse XT is based on FLIR radiometric thermal imaging technology where the recorded microbolometer value is represented as a signal value comprising energy recorded from the surface, reflected energy from the surface, and atmospheric radiation energy (Zeise et al., 2015). Furthermore, it should be noted that many FLIR radiometric thermal imaging cameras (including the DJI Zenmuse XT) have a 14-bit radiometric resolution capable of recording pixel signal values derived from the camera’s A/D converter between 0 and 16383 (FLIR-Systems, 2012; Sagan et al., 2019).¹ The radiometric image pixel signal values can be converted to temperature in Kelvin by performing a radiometric calibration between the recorded pixel signal values and corresponding object surface temperatures (Budzier and Gerlach, 2015). The relationship between the radiometric signal value and the object temperature can be approximated with a Planck curve, as noted by Horny (2003) and similar to Martiny et al. (1996), in Eq. 1 (Budzier and Gerlach, 2015)

$$U_{\text{Obj}} = \frac{R}{\exp\left(\frac{B}{T_{\text{Obj}}}\right) - F} - O, \quad (1)$$

where U_{Obj} represents the radiometric pixel signal value, T_{Obj} represents the surface temperature of the object, R represents the uncooled camera system response, B is a constant derived from Planck’s Radiation Law, F accounts for the non-linear nature of the thermal camera system, and O represents an offset (Budzier and Gerlach, 2015). Eq. 1 is rearranged to solve for T_{Obj} as per Eq. 2 (Budzier and Gerlach, 2015; Tempelhahn et al., 2016)

$$T_{\text{Obj}} = \frac{B}{\ln\left(\frac{R}{U_{\text{Obj}} + O} + F\right)}. \quad (2)$$

These four values, R , B , F and O were calculated by the camera manufacturer through the completion of a non-linear regression from the radiometric calibration data (the blackbody surface temperature and the corresponding radiometric pixel signal value) (Budzier and Gerlach, 2015). However, the authors of this study performed a non-linear regression to fit the $R = R_1/R_2$, B , O , and F constants based on land use type and known surface temperatures in an off-site calibration activity. Note that the complex mining environment did not allow an on-site calibration activity due to access restrictions and safety measures. The raw signal value (U_{Tot}) recorded by the camera is governed by Eq. 3 as described by Usamentiaga et al. (2014)

$$U_{\text{Tot}} = \epsilon\tau U_{\text{Obj}} + \tau(1 - \epsilon)U_{\text{Reff}} + (1 - \tau)U_{\text{Atm}}, \quad (3)$$

where U_{Obj} is the raw output voltage of a blackbody recorded in a laboratory calibration experiment in the absence of reflection and atmospheric influence in the measured signal. To back calculate U_{Obj} , U_{Reff} and U_{Atm} must be determined. U_{Reff} is the theoretical camera output voltage for a blackbody of temperature T_{Reff} according to the calibration. T_{Reff} is the effective temperature of the object surroundings or the reflected ambient temperature. U_{Atm} is the theoretical raw output voltage of a blackbody based on the assumed atmospheric temperature. ϵ is the emissivity of the object and τ is the atmospheric transmissivity. The transmissivity of the atmosphere is generally close to 1.0 (Usamentiaga et al., 2014) under clear weather conditions, so U_{Atm} does not

¹<https://www.dji.com/ca/zenmuse-xt>, last access: 15 February 2019

have to be calculated. From the camera metadata, the assumed reflective temperature (T_{Reff}) was 22 °C. This value was extracted using ExifTool. The U_{Reff} value was calculated using the same Eq. 1 (Zeise and Wagner, 2016)

$$U_{\text{Reff}} = \frac{R}{\exp\left(\frac{B}{T_{\text{Reff}}}\right) - F} - O, \quad (4)$$

where $R = R_1/R_2$, B , F and O are Planck constants of the camera that could be extracted through ExifTool (default constants) or set using fitted constants separately as detailed in Sect. 3.3.

The emissivity of the land surface was determined to be a function of geographic position. The Moderate Resolution Imaging Spectroradiometer (MODIS) instrument MOD11B3 data product was used to derive Land Surface Emissivity (LSE) (Wan et al., 2015). The monthly data product with a resolution of 6 km was used to derive LSE for data collected during the observation campaign in May 2018. The emissivity values were calculated using bands 29, 31, and 32. Since the thermal camera used a Longwave Infrared Radiation (LWIR) detector, radiation within the 7.5 μm to 13.5 μm spectral range was included in the camera voltage output.² MODIS band 29 records radiation within the 8.4 μm to 8.7 μm spectral range, band 31 records radiation within the 10.78 μm to 11.28 μm spectral range, and band 32 records radiation within the 11.77 μm to 12.27 μm spectral range. These three bands are used in conjunction with the BroadBand Emissivity (BBE) derivation to calculate emissivity as a function of geographical area (Wang et al., 2005). The BBE formula used is

$$BBE = a\epsilon_{29} + b\epsilon_{31} + c\epsilon_{32}, \quad (5)$$

where a , b , and c are constants that vary based on the land surface material. Wang et al. (2005) determined that the constants a , b , and c do not vary significantly between soil, vegetation, or anthropogenic materials. However, water, ice, and snow resulted in noticeably different BBE coefficients. Based on Wang et al. (2005), the BBE coefficients for a , b , and c were chosen to be 0.2122, 0.3859, and 0.4029, respectively. After quantifying U_{Reff} , it is possible to back calculate U_{Obj} by rearranging Eq. 3 and finally calculate T_{Obj} via Eq. 2.

The following paragraphs about the calibration are added in Sect. 3.3 of the revised manuscript.

In an attempt to quantify surface temperature measurement inaccuracies of DJI Zenmuse XT, an experiment was conducted to fit the R , B , O and F parameters as per Eq. 2. Three radiometric images were recorded approximately thirty seconds apart every hour between 0600 Local Daylight Time (LDT) and 2300 LDT over a two day period for four distinct surfaces including water, soil, developed land (urban surfaces), and grass. Each radiometric image captured included a certified thermometer, which measured a corresponding temperature for each land surface. The time delay of approximately thirty seconds between each consecutive image was chosen as Olbrycht and Więcek (2015) noted that uncooled thermal cameras without recent calibration experienced temperature drift as much as 1 °C per minute.

FLIR Tools was used to calculate surface temperatures from the radiometric images recorded by the DJI Zenmuse XT on top of the certified thermometer. For each hourly interval, the average of

²<https://www.dji.com/zenmuse-xt/info/>, last access: 15 February 2019

the surface temperatures from the thermal camera were calculated and were used in the following calculations and figures. The pixel value (U_{Obj}) was calculated using Eq. 1, where constants R , B , O and F were defined during camera factory calibration and stored in the metadata of each image. As per Table 1 these values are referred to as the default camera constants. The temperatures recorded by the calibrated thermometer were scaled appropriately as the outdoor field test occurred in Guelph, Ontario, Canada which is 334 m above sea level.

The empirical line method as described by Smith and Milton (1999) was used to relate A/D Counts to the corresponding certified temperatures to calibrate (fit) the R , B , O and F constants as in Fig. 7. Using the Non-Linear Least-Squares Minimization and Curve-Fitting for Python (LMFIT) library,³ the constants were fitted and residuals were minimized for each specific surface material imaged during the calibration experiment using Eq. 2. The default and calibrated camera constants are detailed in Table 1. Fig. 7 displays the experimental, default, and calibrated temperatures as a function of camera pixel signal value for water, soil, developed land, and grass, respectively. The non-linear curve fitting library used the certified temperature obtained during the experiment, the corresponding pixel signal value, and Eq. 2 to derive the calibrated camera parameters.

Table 1: Default and calibrated camera constants.

Camera Parameters	R	B	O	F
Default	366545	1428	-342	1
Calibrated Water	549789	1507	-171	1.5
Calibrated Soil	549800	1510	-171	1.5
Calibrated Developed Land	247614	1322	-513	1.5
Calibrated Grass	314531	1391	-513	1.5

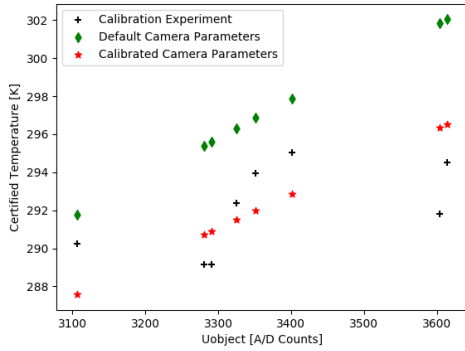
Fitting of the camera constants for each material resulted in reduced bias and Root Mean Square Error (RMSE) values for water, soil, developed land, and grass, respectively, as compared to the bias and RMSE values considering default camera constants, as shown in Table 2. Gallardo-Saavedra et al. (2018) reported that the manufacturer stated accuracy of the FLIR Vue Pro 640 thermal camera was ± 5 K. Kelly et al. (2019) also used the empirical line calibration method for a FLIR Vue Pro 640 thermal camera and determined that the accuracy of the thermal camera was ± 5 K, which is in agreement with our findings.

Table 2: Error statistics in temperature measurement associated with default and calibrated camera constants.

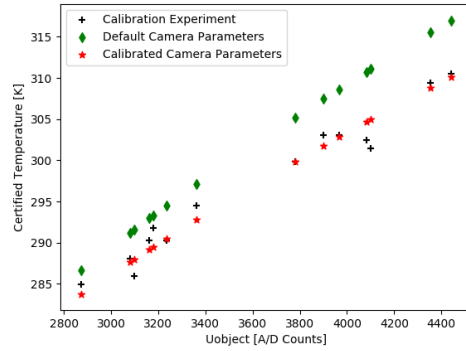
Surface	Water	Soil	Developed Land	Grass
Default Bias	5.18	4.81	1.83	2.07
Default RMSE	5.83	5.34	3.91	2.34
Calibrated Bias	0.27	-0.09	0.13	-0.24
Calibrated RMSE	2.40	1.57	3.31	1.11

The fitted R , B , O and F constants for water, soil, developed land, and grass were applied to surfaces in the actual mining facility with coordinates corresponding to the closest land use categories. Furthermore, the emissivity of the surface was considered by applying the BBE Eq. 5

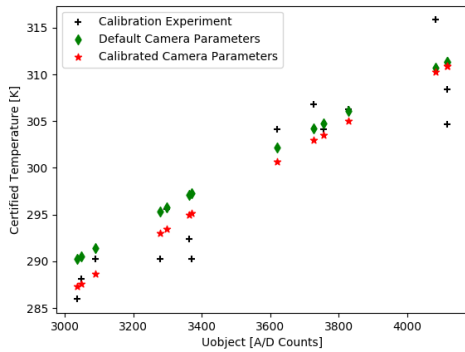
³<https://lmfit.github.io/lmfit-py/index.html>, last access: 10 April 2019



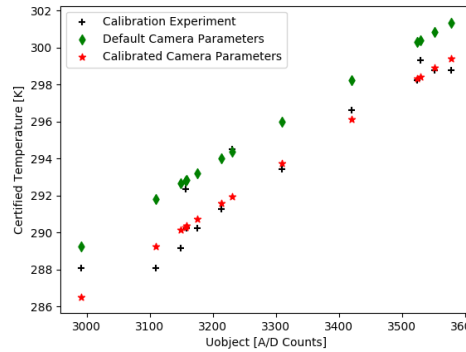
(a) Water



(b) Soil



(c) Developed Land



(d) Grass

Figure 7: Certified temperature compared to radiometric image pixel signal value for Water, Soil, Developed Land, and Grass.

derived by Wang et al. (2005). The boundaries for each land use type were determined by visually inspecting the Landsat 8 Operational Land Imager image recorded on May 17, 2018 with a pixel resolution of 30 m. In QGIS, land use type corresponding to geographic coordinates with a spatial resolution of 1 km were applied and the surface temperatures were calculated according to Fig. 8.

The updated land surface temperature maps for each four-hour time period, the corresponding box plots for each four-hour time period, and the comparison of median surface temperatures between the data collected via the TANAB and MODIS on May 24, 2018 are included in Figs. 9, 10, and 11, respectively.

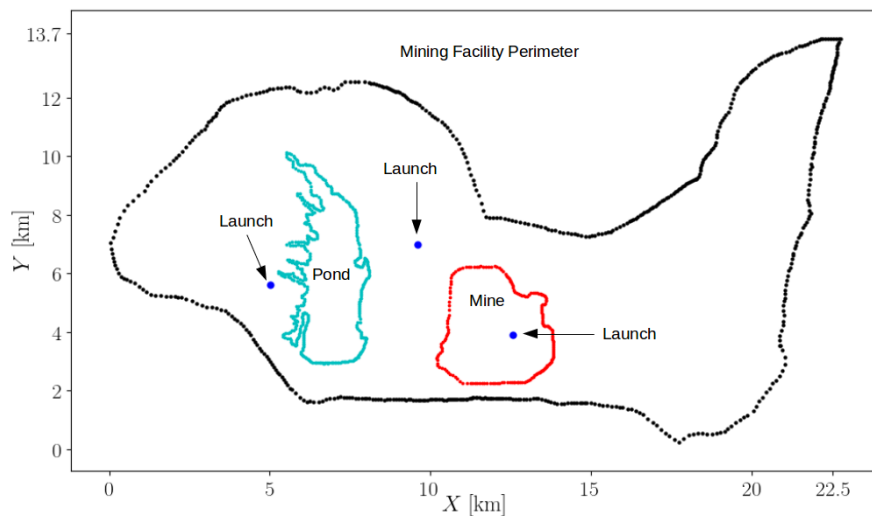


Figure 8: Geographical features of the mining facility as of May 2018.

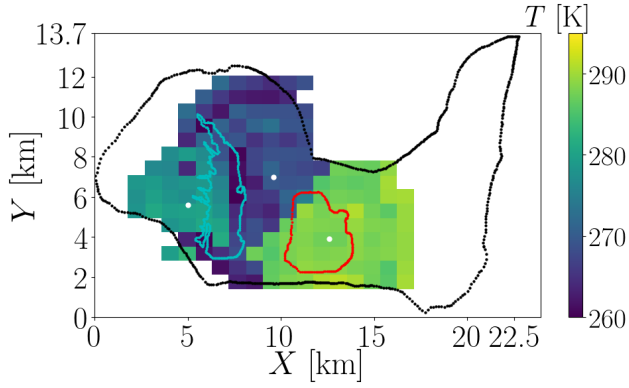
The updated figures, Fig. 9, 10, and 11 are added in the revised manuscript in Sect. 4.7. In Fig. 11, the resulting maximum relative percentage error in temperature for the corrected pond and mine boundaries and using fitted camera constants was calculated as 3.9%, while the median percentage error was calculated as 0.9%. In comparison to the previous calculation not using correct boundaries and fitted camera constants, these errors were 4.8% and 1.0%, respectively. Clearly, the modified method reduces errors.

6. Minor but significant points: when regressing it is best to pivot the data to reduce error.

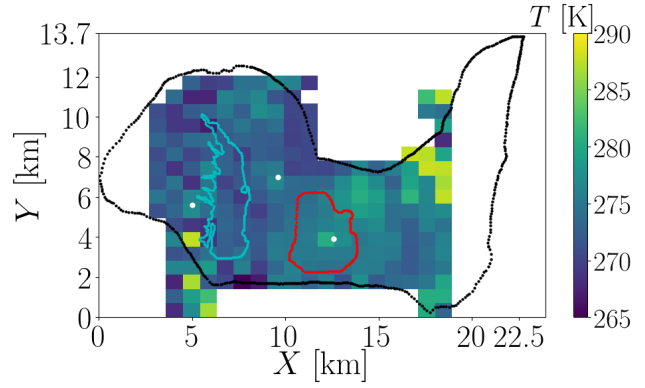
Response: We addressed this comment earlier. Please see our response to comment 5 of the same reviewer. For non-linear fitting of the camera constants, the residuals were minimized.

7. With such fundamental concerns over the methodology, I am unable to comment on the results.

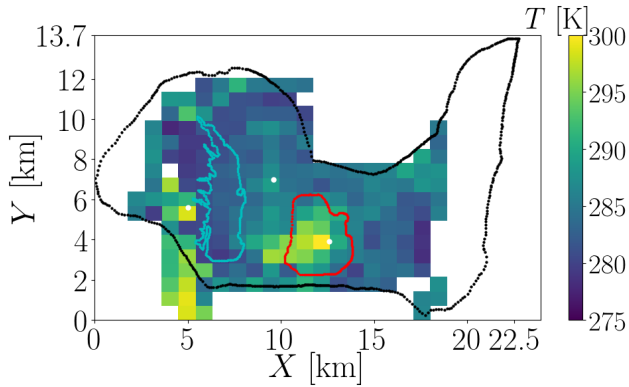
Response: Thank you very much for all your comments. We have worked rigorously to incorporate all your suggestions in the revised manuscript. We hope this new version meets the standards of



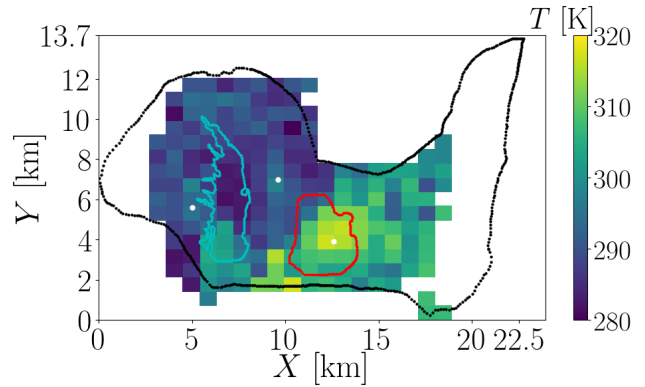
(a) 0000 – 0400 LDT



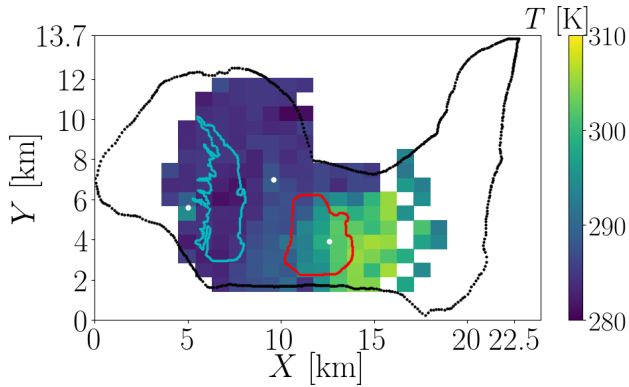
(b) 0400 – 0800 LDT



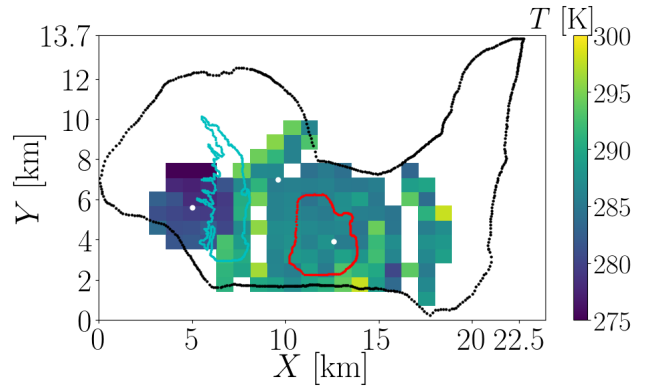
(c) 0800 – 1200 LDT



(d) 1200 – 1600 LDT



(e) 1600 – 2000 LDT



(f) 2000 – 2400 LDT

Figure 9: Median temperature maps for the site at different periods (four-hour intervals) of the day; median temperature calculated for tiles at a resolution of $1 \text{ km} \times 1 \text{ km}$.

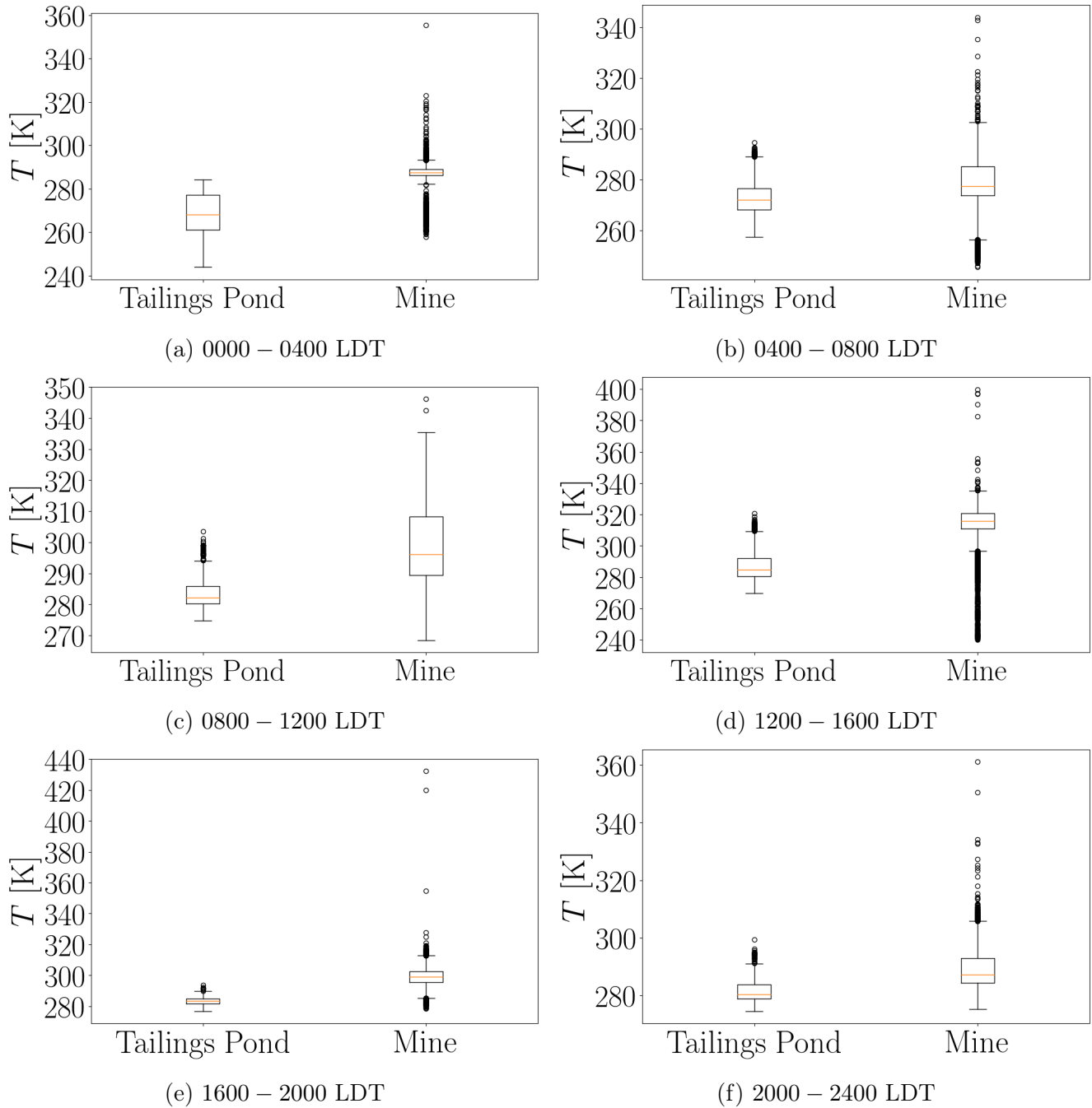


Figure 10: Box plot of temperatures for May 2018 tailings pond and mine boundaries for different periods (four-hour intervals) of the day.

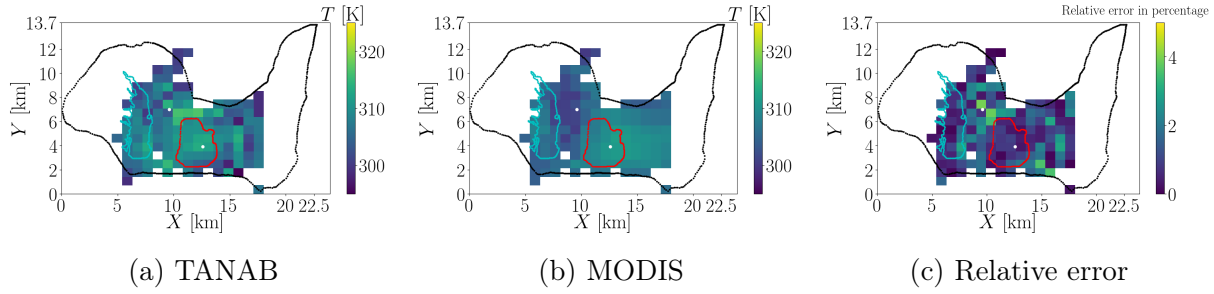


Figure 11: Comparison of median temperatures measured by TANAB and MODIS observations in the early afternoon on 24 May 2018; TANAB and MODIS temperatures calculated for tiles at a resolution of $1 \text{ km} \times 1 \text{ km}$.

the journal.

2 Reviewer 2

1. This paper needs some updates/inclusions/improvements in order to be suitable for publication detailed below.

Response: Thank you very much for your valuable comments that will help make the content and presentation of the manuscript better. We have performed our best to improve the manuscript based on the comments.

2. Use of sensors (lack of rigorous or appropriate calibration, and combining of sensor data to allow for appropriate analysis and conclusions to be drawn).

Response: We have performed rigorous calibration for the TriSonicaTM Mini and the DJI camera. We have addressed this comment. Please see our response to reviewer 1 comment 4 (calibration for the TriSonicaTM Mini) and comment 5 (calibration of DJI camera). We have also updated the manuscript rigorously.

3. GPS, there is no mention of ground control, differential or precise point processing (PPP), whichever is the chosen method of processing GPS and thus geolocating the collected data accurately for analysis and interpretation. The author may have carried this out but without a short in calibration of sensors, I cannot comment on the results.

Response: Establishment of physical Ground Control Points (GCP) at the remote mining site was not possible due to the complex nature of the environment. The remote site was actively being excavated during TANAB flights and physical access to desired GCP locations was prohibited. The following three paragraphs has been added to the Sect. 2.3.1 in the revised manuscript.

The N3 flight controller is equipped with two Inertial Measurement Units (IMUs), a Global Navigation Satellite System (GNSS), and Compass system.⁴ This flight controller is not capable of Real-Time Kinematic (RTK) positioning.

Post processing of GPS data with Precise Point Positioning (PPP) or RTK methods have been noted to reduce geographical positioning error down to a few centimetres (Satirapod et al., 2003; Remondino et al., 2011; Padró et al., 2019). On the other hand, georeferencing capabilities of GNSS and IMU systems are known to have horizontal geographical positional errors of a few meters (Bláha et al., 2011; Chiabrando et al., 2013; Zhuo et al., 2017). Direct georeferencing without the use of differential corrections provide GPS coordinates of a land point within 2 to 5 m of accuracy (Turner et al., 2014; Whitehead et al., 2014). For the purpose of the TANAB system, direct georeferencing with no corrections were used. Vertical positioning of GNSS/IMU systems have been noted in the literature to be prone to significant errors of up to 50 m especially when compared to other RTK and PPP methods (Eynard et al., 2012; Padró et al., 2019). As a result, vertical positioning of the TANAB gondola was completed by considering the hypsometric equation as per Eq. 6 using the airborne barometric pressure and temperature recorded by the ultrasonic anemometer with respect to ground level barometric pressure at the beginning of each

⁴http://dl.djicdn.com/downloads/N3/20170825/N3_User_Manual_En_v1.4.pdf, last access: 15 February 2019

TANAB launch.

Even without the use of RTK or PPP, the resulting temperature maps for the surface of the mining facility have a higher spatio-temporal resolution as compared to conventional satellite based sensors. MODIS⁵ located on both the Terra and Aqua satellites records two distinct thermal images daily, approximately three hours apart at a $1\text{ km} \times 1\text{ km}$ spatial resolution (Crosson et al., 2012; Kumar, 2014; Liu et al., 2017). The Advanced Baseline Imager located on the Geostationary Operational Environmental Satellite (GOES) satellites⁶, are capable of capturing thermal images every 5 min with a spatial resolution of $2\text{ km} \times 2\text{ km}$ (Cintineo et al., 2016; Schmit et al., 2017). Furthermore, Landsat satellites are capable of recording Thermal Infrared (TIR) images. The Landsat 7 Enhanced Thematic Mapper Plus⁷ can capture TIR images at a spatial resolution of $60\text{ m} \times 60\text{ m}$ and the Landsat 8 Thermal Infrared Sensor can record TIR images at a spatial resolution of $100\text{ m} \times 100\text{ m}$.⁸ Both Landsat satellites have a time resolution of 16 days (Chastain et al., 2019). Although errors are inherently introduced into the directly georeferenced surface temperatures, the advantages of collecting both high spatial and temporal resolution land surface temperature data from the TANAB platform outweigh geographical positioning error from the GNSS/IMU system.

4. IMU, there is no detail on the use of the IMU to determine the attitude and motion of the platform this is key to the later calibration and processing of anemometer u,v,w data into the reference of the earth.

Response: We have addressed this comment earlier as a response to reviewer 1 comment 4 (please see the section about gondola motion). We have added more detail in Sect. 2.1 in the revised manuscript. It was not desired to convert the wind velocity measurements to an earth-fixed reference frame. The system is intended to measure *along-wind*, *cross-wind*, and vertical components of wind velocity vector. Further, it was found that the gondola was mostly levelled within $\pm 5^\circ$ 90% of the time and only rotated in the yaw direction. We used IMU roll, pitch, and yaw at a frequency of 200 Hz to quantify the camera line of sight and ultimately performed pixel geographical positioning accordingly. For altitude, we used barometric pressure and temperature measured by the ultrasonic anemometer to calculate the altitude using the standard hypsometric equation (Bolanakis et al., 2015; Stull, 2015).

$$z_2 - z_1 \approx a \bar{T}_v \ln \left(\frac{P_1}{P_2} \right), \quad (6)$$

where P_1 and P_2 are the pressure measurement at two altitudes z_1 and z_2 . The system measured pressure in mBar although the equation is insensitive to the units of pressure. The unit of altitude is m. \bar{T}_v is the average virtual temperature between altitudes z_1 and z_2 . The constant $a = R_d/g$ is equal to 29.3 m K^{-1} (Stull, 2015). Given the uncertainty of temperature and pressure measurement, the uncertainty of altitude measurement is estimated as 1.2 m.

The uncertainty in altitude calculation is quantified using the theory of error propagation analy-

⁵<https://modis.gsfc.nasa.gov/about/>, last access: 20 March 2019

⁶<https://www.nasa.gov/content/goes-overview/index.html>, last access: 20 February 2019

⁷<https://landsat.gsfc.nasa.gov/the-enhanced-thematic-mapper-plus/>, last access: 20 February 2019

⁸<https://landsat.gsfc.nasa.gov/landsat-8/landsat-8-overview/>, last access: 20 February 2019

sis. For the ultrasonic anemometer, the uncertainty of temperature measurement is 2 K and the uncertainty of pressure measurement is 0.01 kPa. A sample calculation for the uncertainty of error on the hypsometric equation is detailed below in Eqs. 7, 8 and 9 assuming $P_2 = 100$ kPa, $P_1 =$ of 101.3 kPa, and $\overline{T}_v = 300$ K (Ku, 1966). The resulting uncertainty was calculated to be 1.2 m.

$$\Delta z_2 = \sqrt{\left(\frac{\partial z_2}{\partial \overline{T}_v}\right)^2 \Delta \overline{T}_v^2 + \left(\frac{\partial z_2}{\partial P_2}\right)^2 \Delta P_2^2}, \quad (7)$$

$$\frac{\partial z_2}{\partial \overline{T}_v} = a \ln \left(\frac{P_1}{P_2} \right), \quad (8)$$

$$\frac{\partial z_2}{\partial P_2} = a \overline{T}_v \left(\frac{-1}{P_2} \right). \quad (9)$$

5. Anemometer, though wind tunnel calibration had been carried out, it did not detail the means of use of processed IMU/GPS data to derive the u,v,w reference to the earth.

Response: We have already addressed this comment. Please see our response to reviewer 1 comment 4.

6. FLIR Zenmuse camera is an uncooled VOx microbolometer so reported measurement related to the total incoming IR radiation and requires calibration by means of accurately measuring a ground surface target. Any calibrated ground based temperature sensor measuring one of the ground targets temperature, probably easiest is to measure the lake with a thermometer.

Response: Thank you for your comments. We have addressed this comment in detail. Please see our response to reviewer 1 comment 5.

7. Balloons and blimps are not a novel platform and as platforms, there is over a centuries worth of documented use. There is no detail on why the Aero Drum balloon was chosen as opposed to a Unmanned Aerial Vehicle (UAV) platform that many of the other researchers in this field are choosing to use. I would expect a more in depth review and detail on why the balloon was the best platform, with references to other papers on the use of balloon, kites, or UAV as platforms and their use of for observing microclimates.

Response: Thank you for your comments. We have included a detailed literature review and references in the revised version of the manuscript in Sect. 1.1 (also please see our response to reviewer 1 comment 2.). We reiterate that we are proposing TANAB as a practical, simple, and low cost system for atmospheric turbulence measurements at lower elevation. Aero Drum balloon was chosen because of its low volume round-oval shape that is aerodynamic and requires less helium compared to larger common Zeppelins. We have explained the advantages of tethered balloon over UAVs as response to reviewer 1 comment 3.

8. On the choice of field site there needs to be considered and justified arguments why the characteristics of the mine are suitable for study of other microclimate environments.

Response: Open-pit mining involves altering surface topography and land use at large scales

beyond 10 to 20 km. Unlike urban neighbourhoods at micro scale, open-pit mining has a large footprint beyond the meso scale so meteorological observations require tools that are able to map such scales. e.g. land fills, industrial ponds, farms, dams, reservoirs, and airport. One cannot easily fly a UAV and map such areas. Also there are safety concerns (please see our response to reviewer 1 comment 3) with flying UAVs in such heavily industrialized and complex facilities. This can provide justification why the tethered balloon approach is useful.

References

- Alderfasi, A. A. and Nielsen, D. C. (2001). Use of crop water stress index for monitoring water status and scheduling irrigation in wheat. *Agr. Water Manage.*, 47(1):69–75.
- Aubry-Wake, C., Baraer, M., McKenzie, M., J., Mark, B. G., Wigmore, O., Hellström, R. A., Lautz, L., and Somers, L. (2015). Measuring glacier surface temperatures with ground-based thermal infrared imaging. *Geophys. Res. Lett.*, 42(20):8489–8497.
- Baker, E. A., Lautz, L. K., McKenzie, J. M., and Aubry-Wake, C. (2019). Improving the accuracy of time-lapse thermal infrared imaging for hydrologic applications. *J. Hydrol.*, 571:60–70.
- Berman, E. A. (1976). Measurements of temperature and downwind spectra in the “buoyant subrange”. *J. Atmos. Sci.*, 33(3):495–498.
- Bláha, M., Eisenbeiss, H., Grimm, D., and Limpach, P. (2011). Direct georeferencing of uavs. In *Int. Arch. Photogramm. Remote Sens. Spatial Inf. Sci.*, XXXCVIII-1/C22, pages 131–136.
- Bolanakis, D. E., Kotsis, K. T., and Laopoulos, T. (2015). Temperature influence on differential barometric altitude measurements. In *2015 IEEE 8th International Conference on Intelligent Data Acquisition and Advanced Computing Systems: Technology and Applications (IDAACS)*, volume 1, pages 120–124.
- Budzier, H. and Gerlach, G. (2015). Calibration of uncooled thermal infrared cameras. *J. Sens. Sens. Syst.*, 4:187–197.
- Caldwell, S. H., Kelleher, C., Baker, E. A., and Lautz, L. K. (2019). Relative information from thermal infrared imagery via unoccupied aerial vehicle informs simulations and spatially-distributed assessments of stream temperature. *Sci. Total Environ.*, 661:364–374.
- Canut, G., Couvreur, F., Lothon, M., Legain, D., Piguet, B., Lampert, A., Maurel, W., and Moulin, E. (2016). Turbulence fluxes and variances measured with a sonic anemometer mounted on a tethered balloon. *Atmos. Meas. Tech.*, 9(9):4375–4386.
- Cao, F., Liu, F., Guo, H., Kong, W., Zhang, C., and He, Y. (2018). Fast detection of *sclerotinia sclerotiorum* on oilseed rape leaves using low-altitude remote sensing technology. *Sensors-Basel*, 18(12):4464.
- Casten, T., Mousset-Jones, P., and Calizaya, F. (1995). *Ultrasonic anemometry in underground excavations*. In A.M. Wala (Ed.), Proc. 7th US Mine Ventilation Symposium, Cushing-Malloy Inc.
- Chastain, R., Housman, I., Goldstein, J., Finco, M., and Tenneson, K. (2019). Empirical cross sensor comparison of sentinel-2a and 2b msi, landsat-8 oli, and landsat-7 etm+ top of atmosphere spectral characteristics over the conterminous united states. *Remote Sens. Environ.*, 221:274–285.
- Chiabrando, F., Lingua, A., and Piras, M. (2013). Direct photogrammetry using uav: tests and first results. In *Int. Arch. Photogramm. Remote Sens. Spatial Inf. Sci.*, XL-1/W2, pages 81–86.
- Cintineo, R. M., Otkin, J. A., Jones, T. A., Koch, S., and Stensrud, D. J. (2016). Assimilation

- of synthetic goes-r abi infrared brightness temperatures and wsr-88d radar observations in a high-resolution osse. *Mon. Weather Rev.*, 144(9):3159–3180.
- Crosson, W. L., Al-Hamdan, M. Z., Hemmings, S. N., and Wade, G. M. (2012). A daily merged modis aqua-terra land surface temperature data set for the conterminous united states. *Remote Sens. Environ.*, 119(8):315–324.
- Davidson, B. (1968). The barbados oceanographic and meteorological experiment. *B. Am. Meteorol. Soc.*, 49(9):928–935.
- Egerer, U., Gottschalk, M., Siebert, H., Ehrlich, A., and Wendisch, M. (2019). The new beluga setup for collocated turbulence and radiation measurements using a tethered balloon: first applications in the cloudy arctic boundary layer. *Atmos. Meas. Tech.*, 12(7):4019–4038.
- Eynard, D., Vasseur, P., Demonceaux, C., and Frémont, V. (2012). Real time uav altitude, attitude and motion estimation from hybrid stereovision. *Auton. Robot.*, 33(1-2):157–172.
- FLIR-Systems (2012). *The ultimate infrared handbook for R&D professionals*. FLIR Systems.
- Friedman, H. A. and Callahan, W. S. (1970). The ESSA research flight facility’s support of environmental research in 1969. *Weatherwise*, 23(4):174–185.
- Gallardo-Saavedra, S., Hernández-Callejo, L., and Oscar, D.-P. (2018). Technological review of the instrumentation used in aerial thermographic inspection of photovoltaic plants. *Renew. Sust. Energ. Rev.*, 93:566–579.
- Garstang, M. and La Seur, N. E. (1968). the 1968 Barbados experiment. *B. Am. Meteorol. Soc.*, 49(6):627–635.
- Haugen, D. A., Kaimal, J. C., Readings, C. J., and Rayment, R. (1975). A comparison of balloon-borne and tower-mounted instrumentation for probing the atmospheric boundary layer. *J. Appl. Meteorol.*, 14(4):540–545.
- Horny, N. (2003). FPA camera standardisation. *Infrared Phys. Techn.*, 44(2):109–119.
- Kelly, J., Kljun, N., Olsson, P.-O., Mihai, L., Liljeblad, B., Weslien, P., Klemdtsson, L., and Eklundh, L. (2019). Challenges and best practices for deriving temperature data from an uncalibrated uav thermal camera. *Remote Sens-Basel*, 11:567.
- Ku, H. H. (1966). Notes on the use of propagation of error formulas. *J. Res. Nat. Bur. Stand. Sec. C: Eng. Inst.*, 70(4):263.
- Kumar, A. (2014). Long term (2003-2012) spatio-temporal modis (terra/aqua level 3) derived climatic variations of aerosol optical depth and cloud properties over a semi arid urban tropical region of northern india. *Atmos. Environ.*, 83:291–300.
- Lin, D., Maas, H.-G., Westfield, P., Budzier, H., and Gerlach, G. (2018). An advanced radiometric calibration approach for uncooled thermal cameras. *Photogramm. Rec.*, 33(161):30–48.
- Liu, L., Li, C., Lei, Y., Yin, J., and Zhao, J. (2017). Volcanic ash cloud detection from modis image based on cpiws method. *Acta Geophys.*, 65(1):151–163.
- Lothon, M., Lohou, F., Pino, D., Couvreux, F., Pardyjak, E. R., Reuder, J., Vilà-Guerau de Arellano, J., Durand, P., Hartogensis, O., Legain, D., Augustin, P., Gioli, B., Lenschow, D. H.,

- Falooona, I., Yagüe, C., Alexander, D. C., Angevine, W. M., Bargain, E., Barrié, J., Bazile, E., Bezombes, Y., Blay-Carreras, E., van de Boer, A., Boichard, J. L., Bourdon, A., Butet, A., Campistron, B., de Coster, O., Cuxart, J., Dabas, A., Darbieu, C., Deboudt, K., Delbarre, H., Derrien, S., Flament, P., Fourmentin, M., Garai, A., Gibert, F., Graf, A., Groebner, J., Guichard, F., Jiménez, M. A., Jonassen, M., van den Kroonenberg, A., Magliulo, V., Martin, S., Martinez, D., Mastrorillo, L., Moene, A. F., Molinos, F., Moulin, E., Pietersen, H. P., Piguet, B., Pique, E., Román-Cascón, C., Rufin-Soler, C., Saïd, F., Sastre-Marugán, M., Seity, Y., Steeneveld, G. J., Toscano, P., Traullé, O., Tzanos, D., Wacker, S., Wildmann, N., and Zaldei, A. (2014). The bllast field experiment: Boundary-layer late afternoon and sunset turbulence. *Atmos. Chem. Phys.*, 14(20):10931–10960.
- Luo, L., Ma, W., Zhao, W., Zhuang, Y., Zhang, Z., Zhang, M., Ma, D., and Zhou, Q. (2018). UAV-based spatiotemporal thermal patterns of permafrost slopes along the Qinghai-Tibet Engineering Corridor. *Landslides*, 15(11):2161–2172.
- Mallast, U. and Siebert, C. (2019). Combining continuous spatial and temporal scales for SGD investigations using UAV-based thermal infrared measurements. *Hydrol. Earth Syst. Sci.*, 23:1375–1392.
- Martikainen, A., Dougherty, H., Taylor, C., and Mazzella, A. (2010). Sonic anemometer airflow monitoring technique for use in underground mines. *In: Proceedings of the 13th U.S./North American mine ventilation symposium, Sudbury, Ontario, Canada, June 2010.*
- Martin, S., Bange, J., and Beyrich, F. (2011). Meteorological profiling of the lower troposphere using the research uav "m²av carolo". *Atmos. Meas. Tech.*, 4(4):705–716.
- Martiny, M., Schiele, R., Gritsch, M., Schulz, A., and Wittig, S. (1996). In situ calibration for quantitative infrared thermography. *Quant. Infr. Therm. J.*
- Murray, B., Anderson, D. T., Wescott, D. J., Moorhead, R., and Anderson, M. F. (2018). Survey and insights into unmanned aerial-vehicle-based detection and documentation of clandestine graves and human remains. *Hum. Biol.*, 90(1):45–61.
- Olbrycht, R. and Więcek, B. (2015). New approach to thermal drift correction in microbolometer thermal cameras. *Quant. Infr. Therm. J.*, 12(2):184–195.
- Padró, J.-C., Muñoz, F.-J., Planas, J., and Pons, X. (2019). Comparison of four uav georeferencing methods for environmental monitoring purposes focusing on the combined use with airborne and satellite remote sensing platforms. *Int. J. Appl. Earth Obs.*, 75:130–140.
- Palomaki, R. T., Rose, N. T., van den Bossche, M., Sherman, T. J., and De Wekker, S. F. J. (2017). Wind estimation in the lower atmosphere using multicopter aircraft. *J. Atmos. Ocean. Tech.*, 34(5):1183–1191.
- Poblete, T., Ortega-Farías, and Ryu, D. (2018). Automatic coregistration algorithm to remove canopy shaded pixels in UAV-borne thermal images to improve the estimation of crop water stress index of a drip-irrigated cabernet sauvignon vineyard. *Sensors-Basel*, 18(2):397.
- Pollard, R. T. (1978). The joint air-sea interaction experiment—jasin 1978. *B. Am. Meteorol. Soc.*, 59(10):1310–1318.

- Remondino, F., Barazzetti, L., Scaioni, M., and Sarazzi, D. (2011). Uav photogrammetry for mapping and 3d modeling - current status and future perspectives. In *Int. Arch. Photogramm. Remote Sens. Spatial Inf. Sci.*, XXXVIII-1/C22, pages 25–31.
- Ribeiro-Gomes, K., Hernández-López, D., Ortega, J. F., Ballesteros, R., Poblete, T., and Moreno, M. A. (2017). Uncooled thermal camera calibration and optimization of the photogrammetry process for UAV applications in agriculture. *Sensors-Basel*, 17(10):2173.
- Sagan, V., Maimaitijiang, M., Sidike, P., Eblimit, K., Peterson, K. T., Hartling, S., Esposito, F., Khanal, K., Newcomb, M., Pauli, D., Ward, R., Fritschi, F., Shakoob, N., and Mockler, T. (2019). UAV-Based high resolution thermal imaging for vegetation monitoring and plant phenotyping using ICI 8640 P, FLIR Vue Pro R 640 and thermoMap cameras. *Remote Sens-Basel*, 11(3):330.
- Satirapod, C., Trisirisatayawong, I., and Homniam, P. (2003). Establishing ground control points for high-resolution satellite imagery using gps precise point positioning. In *2003 IEEE International Geoscience and Remote Sensing Symposium. Proceedings*, pages 4486–4488.
- Schmit, T. J., Griffith, P., Gunshor, M. M., Daniels, J. M., Goodman, S. J., and J., L. W. (2017). A closer look at the abi on the goes-r series. *B. Am. Meteorol. Soc.*, 98(4):681–698.
- Sheng, H., Chao, H., Coopmans, C., Han, J., McKee, M., and Chen, Y. Q. (2010). Low-cost UAV-based thermal infrared remote sensing: platform, calibration and applications. In *Proceedings of 2010 IEEE/ASME International Conference on Mechatronic and Embedded Systems and Applications*, pages 38–43.
- Smith, F. B. (1961). An analysis of vertical wind-fluctuations at heights between 500 and 5,000 ft. *Q. J. Roy. Meteor. Soc.*, 87(372):180–193.
- Smith, G. M. and Milton, E. J. (1999). The use of the empirical line method to calibrate remotely sensed data to reflectance. *Int. J. Remote Sens.*, 13:2653–2662.
- Stevens, W. R., Squier, W., Mitchell, W., Gullett, B. K., and Pressley, C. (2013). Measurement of motion corrected wind velocity using an aerostat lofted sonic anemometer. *Atmos. Meas. Tech. Discussions*, 6:703–720.
- Stull, R. B. (2015). *Practical Meteorology: An Algebra-based Survey of Atmospheric Science*. Univ. of British Columbia.
- Tempelhahn, A., Budzier, H., Krause, V., and Gerlach, G. (2016). Shutter-less calibration of uncooled infrared cameras. *J. Sens. Sens. Syst.*, 5(1):9–16.
- Thompson, N. (1972). Turbulence measurements over the sea by a tethered-balloon technique. *Q. J. Roy. Meteor. Soc.*, 98(418):745–762.
- Thompson, N. (1980). Tethered balloons. In: *Dobson F., Hasse L., Davis R. (eds) Air-Sea Interaction*. Springer, Boston, MA, pages 589–604.
- Turner, D., Lucieer, A., and Wallace, L. (2014). Direct georeferencing of ultrahigh-resolution uav imagery. *IEEE T. Geosci. Remote*, 52(5):2738–2745.
- Usamentiaga, R., Venegas, P., Guerediaga, J., Vega, L., Molleda, J., and Bulnes, F. G. (2014).

- Infrared thermography for temperature measurement and non-destructive testing. *Sensors*, 14(7):12305–12348.
- Wan, Z., Hook, S., and Hulley, G. (2015). Mod11b3 modis/terra land surface temperature/emissivity monthly l3 global 6 km sin grid v006, [data set]. *NASA EOSDIS LP DAAC*.
- Wang, K., Wan, Z., Wang, P., Sparrow, M., Liu, J., Zhou, X., and Haginoya, S. (2005). Estimation of surface long wave radiation and broadband emissivity using moderate resolution imaging spectroradiometer (modis) land surface temperature/emissivity products. *J. Geophys. Res.-Atmos.*, 110(D11).
- Whitehead, K., Hugenholtz, C. H., Myshak, S., Brown, O., LeClair, A., and Tamminga, A. (2014). Remote sensing of the environment with small unmanned aircraft systems (UASs), part 2: scientific and commercial applications. *Journal of Unmanned Vehicle Systems*, 2(3):86.
- Zeise, B., Kleinschmidt, S. P., and Wagner, B. (2015). Improving the interpretation of thermal images with the aid of emissivity’s angular dependency. In *2015 IEEE International Symposium on Safety, Security and Rescue Robotics (SSRR)*, pages 1–8.
- Zeise, B. and Wagner, B. (2016). Temperature correction and reflection removal in thermal images using 3d temperature mapping. In *Proceedings of the 13th International Conference on Informatics in Control, Automation and Robotics*, 2:158–165.
- Zhong, Y., Xu, Y., Wang, X., Jia, T., Ma, A., and Zhang, L. (2019). Pipeline leakage detection for district heating systems using multisource data in mid- and high-latitude regions. *ISPRS J. Photogramm.*, 151:207–222.
- Zhuo, X., Koch, T., Kurz, F., Fraundorfer, F., and Reinartz, P. (2017). Automatic uav image georegistration by matching uav images to georeferenced image data. *Remote Sens-Basel*, 9(4):376.

A Tethered And Navigated Air Blimp (TANAB) for observing the microclimate over a complex terrain

Manoj K. Nambiar¹, Ryan A. E. Byerlay¹, Amir Nazem¹, M. Rafsan Nahian¹, Mohsen Moradi¹, and Amir A. Aliabadi¹

¹School of Engineering, University of Guelph, Guelph, ON, Canada

Correspondence: Amir A. Aliabadi (aliabadi@uoguelph.ca)

Abstract. This study presents the first environmental monitoring field campaign of a newly developed Tethered And Navigated Air Blimp (TANAB) system to investigate the microclimate over a complex terrain. The use of a tethered balloon in complex terrains such as mines and tailings ponds is novel and the focus of the present study. The TANAB system was fully developed and launched at a mine facility in northern Canada in May 2018. This study describes the key design features, the sensor payload onboard, [calibration](#), and the observations made by the TANAB system. The system measured meteorological conditions including wind speed in three directions, temperature, relative humidity, and pressure over the first few tens of meters of the atmospheric boundary layer. The system also performed earth surface thermal imaging, or temperature mapping, of the underlying surface. The measurements were made at two primary locations in the facility: i) near a tailings pond and ii) in a mine pit. TANAB measured the dynamics of the atmosphere at different diurnal times (e.g. day versus night) and locations (near tailings pond versus inside the mine). Such dynamics include mean and turbulence statistics pertaining to flow momentum and energy, and they are crucial in the understanding of emission fluxes from the facility in future studies. In addition, TANAB can provide boundary conditions and validation datasets to support mesoscale dispersion modelling or **Computational Fluid Dynamics (CFD)** [computational fluid dynamics](#) simulations for various transport models.

1 Introduction

The Atmospheric Boundary Layer (ABL) is the lowest portion of the air near the earth surface that responds to surface processes in one hour or less (Stull, 1988; Aliabadi, 2018). The understanding of the atmospheric turbulent processes governing the transfer of heat, moisture, and momentum ~~between the surface and the free troposphere in the surface layer~~ is of practical importance for many applications such as weather and climate prediction, pollution dispersion ~~modelling~~, and urban air quality studies (Zilitinkevich and Baklanov, 2002; Pichugina et al., 2008; Aliabadi et al., 2016b, c). Most of the research in atmospheric turbulence have been focused on relatively smooth terrain and horizontally homogeneous environments mainly due to the limitation in the availability of adequate observation platforms and difficulty in acquiring data from the complex environments. However, the study of the ABL and surface-atmosphere interaction over complex terrain is very important for many applications. Surface heterogeneity can cause horizontal gradients of momentum or temperature, and it can influence or complicate the horizontal and vertical transport mechanisms, for instance driven by slopes or thermals (Mahrt and Vickers,

2005; Medeiros and Fitzjarrald, 2014). In addition, model parameterizations of ~~turbulence~~turbulent processes established for atmospheric flows over smooth and homogeneous surfaces often fail when applied over inhomogeneous and complex terrains (Roth, 2000).

5 1.1 ~~Technology Gaps~~Literature Review

Two types of ABL observations of the meteorological parameters are key: atmospheric properties and earth surface properties (Mäkiranta et al., 2011; Manoj et al., 2014). Conventional techniques measuring the atmospheric properties such as remote sensing (e.g. satellite, RADARS¹, LIDARS², SODARS³, radiometers) and in situ measurements (meteorological masts, aircraft, or sounding balloons) are widely-used for observing parameters such as wind, humidity, and temperature (Pichugina et al., 2008; Legain et al., 2013; Aliabadi et al., 2016b, 2018a). The main disadvantages of such conventional techniques are the low frequency of turbulence measurements (SODARs and LIDARs), cost (aircraft and satellites), difficulty of navigation (sounding balloons), intermittency of observation (Aircraft, sounding balloons, and non-geostationary satellites), low spatial resolution (geostationary satellites), and limited spatial coverage (meteorological towers) (Fernando and Weil, 2010; Medeiros and Fitzjarrald, 2014). In addition, measuring the surface layer within the ABL poses a serious challenge to aircraft that cannot fly at altitudes lower than 150 m in many jurisdictions for safety reasons (Mayer et al., 2012).

Airborne systems are increasingly being used for atmospheric measurements (Martin et al., 2011; Palomaki et al., 2017) although recently their use is being regulated more restrictively. For instance, rotary or fixed-wing drones are not permitted to fly in complex environments such as busy urban areas and airports. On the other hand, tethered balloon-based atmospheric measurement techniques have been used widely for obtaining the turbulence structure as well as the mean vertical profiles of the ABL in complex environments (Thompson, 1980). One of the main advantages of a tethered balloon system is its ability to profile a significant portion of the planetary boundary layer starting from the surface, which is not possible or economical by ground-based or aircraft-based atmospheric measurement techniques (Egerer et al., 2019). The use of ultrasonic anemometers in tethered balloons have been reported in many studies (Stevens et al., 2013; Canut et al., 2016). In comparison, one of the disadvantage of Pitot tubes is their inability to measure the low wind speeds. So they require a fast flying probe which cannot fly in a complex environment for safety and logistic reasons. Ultrasonic anemometers, on the other hand, are popular because of their continuous measurement characteristics, high accuracy, and their ability to be levitated to measure low velocities (Casten et al., 1995; Martikainen et al., 2010). In addition, studies have shown that tethered balloon-based probes can be used for continuous measurement of the important parameters in the ABL without influencing the flow compared to tower-mounted instruments, where the tower structure can perturb the flow measurement, or presence of complex topography or nearby buildings that can influence the measurement (Haugen et al., 1975; Stevens et al., 2013).

Tethered balloon-borne atmospheric turbulence measurements have a long history of observations over the land (Smith, 1961) and sea (Thompson, 1972) to measure fluxes of heat and moisture at heights up to a few hundred metres. The most notable tethered

¹Radio Detection And Ranging

²Light Detection And Ranging

³Sonic Detection And Ranging

balloon systems deployed collected data in campaigns in the late 1960s and 1970s including the Barbados Oceanographic and Meteorological Experiment (BOMEX) (Davidson, 1968; Garstang and La Seur, 1968; Friedman and Callahan, 1970), the Joint Air-Sea Interaction (JASIN) Experiment (Pollard, 1978), and the Global Atmospheric Research Programme (GARP) Atlantic Tropical Experiment (GATE) (Berman, 1976). In BOMEX a tethered balloon system was operated from the deck, which measured temperature, wind, and humidity continuously, at different levels in the range of 0 to 600 m in the ocean area north and east of the Island of Barbados. In JASIN tethered balloons were used to measure the structure of ABL to understand the air-sea interaction in the North Atlantic. In the recent past, tethered balloon systems have been used in Boundary-Layer Late Afternoon and Sunset Turbulence (BLLAST) field campaign that was conducted in southern France (Lothon et al., 2014). Canut et al. (2016) used an ultrasonic anemometer mounted on a tethered balloon system for turbulent flux and variance measurements. Egerer et al. (2019) used the BELUGA (Balloon-bornE modulArUtility) tethered balloon system for profiling the lower Atmosphere by turbulence and radiation measurements in the Arctic.

As far as earth surface properties are concerned, Land Surface Temperature (LST) is a crucial meteorological parameter to be measured that influences the energy budget and dynamics of the atmosphere. ~~H-LST~~ LST has historically been derived from conventional satellite-based sensors such as the MODerate resolution Imaging Spectroradiometer (MODIS) on the Terra and Aqua satellites, the Advanced Baseline Imager on the Geostationary Operational Environmental Satellites (GOES), the Enhanced Thematic Mapper Plus (ETM+) on Landsat 7 and the Thermal Infrared Sensor (TIRS) on Landsat 8 (Tomlinson et al., 2011; Chastain et al., 2019). These sensors however, only either record images with a high spatial resolution and a low temporal resolution (ETM+ and TIRS) or a high temporal resolution and a low spatial resolution (GOES) (Irons et al., 2012; Chastain et al., 2019; Cintineo et al., 2016; Schmit et al., 2017) (Irons et al., 2012; Cintineo et al., 2016; Schmit et al., 2017). Furthermore, satellite-based sensors are known to have missing and skewed data due to a variety of environmental factors including atmospheric effects, land surface emissivity, and sensor failure (Li et al., 2013; Malamiri et al., 2018).

Recent advancements of Unmanned Aerial ~~Vehicles (UAVs)~~ Systems (UAS) and miniaturization of thermal imaging technology, have allowed researchers to remotely sense the environment for more reliable and precise LST measurements (Malbêteau et al., 2018). With the inclusion of Inertial Measurement Units ~~and Global Positioning Systems on UAVs~~ (IMU) and Global Navigation Satellite System (GNSS) for UAS, airborne images can be directly georeferenced without Ground Control Points (GCP) (Turner et al., 2014). Quantitative data from images recorded from ~~UAV systems~~ UAS can be readily derived from proprietary software including PhotoScan Professional, Pix4Dmapper, and MATLAB (Verykokou and Ioannidis, 2018). Open source direct georeferencing and LST calculation software programs are not commonly used.

From literature, the use of uncooled thermal cameras for quantification of relative surface temperatures have been documented many times for a variety of applications. Improvements in UAS and thermal imaging technology have allowed waterbodies to be mapped with a high spatiotemporal resolution. Specifically, understanding the spatial and temporal variation of thermal plumes from sources, such as influent stormwater or geothermal activity, on waterbodies is of significant importance for many hydrological applications (Baker et al., 2019). Water temperature is also a parameter used to quantify water quality as it is known to impact aquatic organisms (Caldwell et al., 2019). Localized areas of higher surface water temperature were effectively identified by using a DJI Zenmuse XTR uncooled thermal camera without additional radiometric calibration

(Caldwell et al., 2019). Mallast and Siebert (2019) utilized a UAS-based FLIR Tau 2 thermal camera to spatially map submarine groundwater discharge in the Dead Sea, Israel. The intrusion of cooler groundwater rising to the surface of the Dead Sea was captured by the thermal camera, and the variation of spatial perturbations with respect to time were represented. Similarly, uncooled microbolometer thermal imaging systems have been employed to quantify the spatial distribution of surface temperatures of glaciers (Aubry-Wake et al., 2015). This data can be used to increase the accuracy of energy budget models developed for glaciers (Aubry-Wake et al., 2015). Luo et al. (2018) used a Zenmuse XT uncooled thermal camera to spatially map surface temperature variations of permafrost slopes. Understanding the variation of surface temperature of permafrost slopes is very important for infrastructure management and planning of railways, pipelines, and roads constructed on permafrost (Luo et al., 2018).

Uncooled microbolometer thermal cameras have also been used extensively in the agricultural industry, especially in the emerging precision agriculture sector. Poblete et al. (2018) used a FLIR Tau 2 640 uncooled thermal camera to quantify plant water stress which is a measure of water availability for crops (Alderfasi and Nielsen, 2001). A FLIR Tau 2 640 uncooled microbolometer thermal camera was used by Cao et al. (2018) to image plant leaf temperatures to identify *Sclerotinia sclerotiorum* on the leaves of oilseed rape plants.

UAS-based microbolometer thermal imaging cameras have also been noted to have some niche applications in literature. For example, Murray et al. (2018) successfully conducted a study using the FLIR Systems Vue Pro to identify relative temperature variations between human remains and the surrounding environment. Gallardo-Saavedra et al. (2018) detailed numerous studies where uncooled microbolometer thermal cameras were used to inspect photovoltaic panels and quantify performance of photovoltaic plants. Zhong et al. (2019) completed a study using a FLIR Tau 2 640 to assist in identifying pipeline leakages within a district heating system.

It is well reported in literature that uncooled microbolometer temperature measurements are impacted by variation of sensor, camera, and ambient temperatures (FLIR-Systems, 2012; Budzier and Gerlach, 2015; Lin et al., 2018). Considering these three sources of measurement error, it is not acceptable to consider calculated surface temperatures from uncooled microbolometers to be absolute without a calibration. Conversely, cooled thermal cameras are designed to measure temperatures with a high degree of accuracy such that absolute temperatures could be determined (Ribeiro-Gomes et al., 2017). Although cooled thermal cameras are very accurate, they are significantly heavier, more expensive, and require more power to operate (Sheng et al., 2010; Ribeiro-Gomes et al., 2017). As a result, cooled thermal cameras are not commonly used for small UAS (such as drones and blimps) (Sheng et al., 2010).

1.2 Objectives

There are only a few comprehensive field studies that focus on the ABL over a mine environment while the structure of ABL in an orographically complex terrain such as a mine can be complicated (Rotach and Zardi, 2007; Medeiros and Fitzjarrald, 2014, 2015). In the surface layer, flows are highly influenced by the terrain geometry, while Coriolis effects have still negligible influences (Arroyo et al., 2014). Much less, the authors are only aware of two tethered balloon-based earth surface temperature quantification studies (Vierling et al., 2006; Rahaghi et al., 2019). These gaps in the literature motivated this work.

The Tethered And Navigated Air Blimp (TANAB), developed by the authors, is a ~~unique~~-mobile sensing platform for the investigation of surface layer within ABL overcoming some of the ~~above limitations~~ limitations mentioned in the literature review. TANAB is lifted by the buoyancy force and requires no propulsion power for navigation compared to drones. This allows turbulence measurements over long periods without disturbing the surrounding air. It provides accurate in-situ measurements unlike remote sensing technologies such as LIDARs, SODARs, and satellites. It is safer to operate at low altitudes compared to manned aircraft. It can be navigated and redeployed using a tether, unlike radiosondes, and it is very cost effective. TANAB can collect high time-resolution observations of the weather to characterize the turbulence properties in low altitudes in almost all weather conditions. In case of extreme wind, TANAB can still be used with the help of additional stabilizing tethers (usually up to three). The variables it measures include wind speed in three directions, temperature, relative humidity, and pressure. It also performs earth surface thermal imaging, or temperature mapping, of the underlying terrain.

TANAB observations can be utilized in numerous ways. Atmospheric dynamics as measured by TANAB can determine transport mechanisms that drive emission fluxes (Stuedler et al., 1991). Factors such as mean wind speed, atmospheric diffusion coefficient, and thermal stability, greatly influence emission fluxes (Bowden et al., 1993), all of which are measured by TANAB. It can also provide boundary conditions and validation datasets to support ABL simulations using ~~Computational Fluid Dynamics (CFD)~~ computational fluid dynamics or mesoscale modelling. Furthermore, the environmental data collected can be used to develop and validate microclimate and dispersion models in complex mining or urban environments (Krayenhoff and Voogt, 2007; Bueno et al., 2012; Holnicki and Nahorski, 2015; Aliabadi et al., 2017).

~~There are only a few comprehensive field studies that focus on the ABL over a mine environment while the structure of ABL in an orographically complex terrain such as a mine can be complicated (Rotach and Zardi, 2007; Medeiros and Fitzjarrald, 2014, 2015). In this study, the TANAB system is demonstrated while being tested to reveal the surface layer meteorology of a complex terrain in a mining facility. In the surface layer, flows are highly influenced by the terrain geometry, while Coriolis effects have still negligible influences (Arroyo et al., 2014). TANAB measurements are reported at different diurnal times (e.g. day versus night) and locations (near tailings pond versus inside the mine).~~

1.3 Structure of the Paper

The structure of the paper is organized as follows. Section 2 briefly describes the TANAB system and the sensors payload. Calibration experiments are explained in Sect. 3. Section 4 presents field experiments and results of the environmental monitoring campaign where TANAB was used in a complex mining facility. Conclusions and future recommendations are provided in Sect. 5.

2 Tethered And Navigated Air Blimp (TANAB) Specification

TANAB consists of fixed and variable payloads. The fixed payload is comprised of a helium balloon, the navigation tether, a tether reel, and a gondola platform housing the sensors. The variable payload is comprised of microclimate sensors, such as a

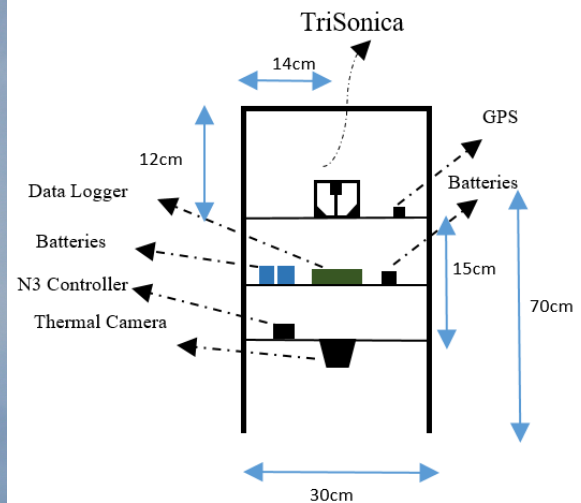
5 mini weather station and a thermal camera, and a flight controller. While the fixed payload is the same for every mission, the variable payload can be altered to use different sensors suitable for a particular application.

2.1 Envelop and Platform

The balloon envelop is manufactured by Aero Drum Ltd.⁴ It is an ellipsoid made out of polyurethane with dimensions of 2.8 m × 2.8 m × 1.9 m providing axisymmetric aerodynamic stability. The envelop is filled with up to 8 m³ of balloon grade helium capable of lifting 5 kg of payload although at least 1.5 kg of surplus lift is recommended for stable performance. The polyurethane envelop provides a good seal and results in only up to a maximum 0.5 % volume helium loss per day, enabling the system to be used up to 24 hr before a helium recharge is necessary. The tethered navigation system enables deployment of the balloon at a location of interest while controlling the ascend or descend rate. A close-up of the TANAB system during sampling and a system schematic can be seen in Fig. 1.



(a) TANAB



(b) Schematic of gondola and sensors

Figure 1. Left: close-up of the Tethered And Navigated Air Blimp (TANAB) system during sampling ; right: and the schematic of the TANAB gondola with all the sensors.

15 The gondola is a part of the tethered balloon system controlled by multiple ropes on the ground. The acting forces on the system are 1) the lift force due to the helium-filled balloon, 2) the force of gravity, 3) the tension forces due to the ropes, and 4) the drag forces due to the wind. In the absence of the drag force the remaining forces are acting in the vertical direction and the system ascends up or down, but the presence of the drag force displaces the system in the horizontal direction. At all times these forces are balanced so that the TANAB is in a quasi-stationary position.

⁴<https://www.rc-zepplin.com/>, last access: 15 February 2019

The balloon is equipped with a net that helps facing the balloon against the main wind direction at any moment. The net guides the air on one side, and the pressure force stops the balloon from rotating. In case of wind direction changing, the pressure force builds up on the net creating a torque around the centre of rotation that repositions the balloon facing the main wind. Up to three ropes are used to tether the balloon to help with stabilizing the system, especially during high winds associated with convective boundary layers. The ropes, however, impose extra weight on the system so that the vertical range of the system reduces when three ropes are used as opposed to one.

The evidence that the net mechanism succeeds in aligning the balloon against the main wind direction can be found in Fig. 2. The wind-rose shows the wind direction records by TriSonica™ Mini (at TriSonica™ Mini's coordinate) for over 56 hr of flight. According to the wind-rose the gondola mostly faces against the main wind direction because wind direction is recorded from the local north direction most of the time. Note that TriSonica™ Mini's north axis is the sensor local coordinate. If desired, this reading can be converted into the fixed inertial body of reference. For this to occur, the sensor yaw, pitch, and roll angles need to be used. This conversion, however, was not desired in the present analysis.

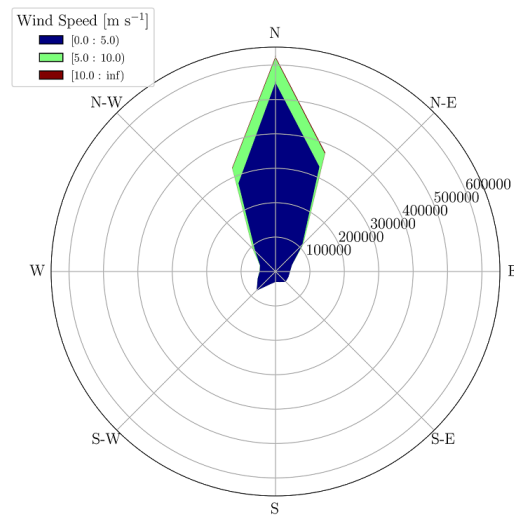
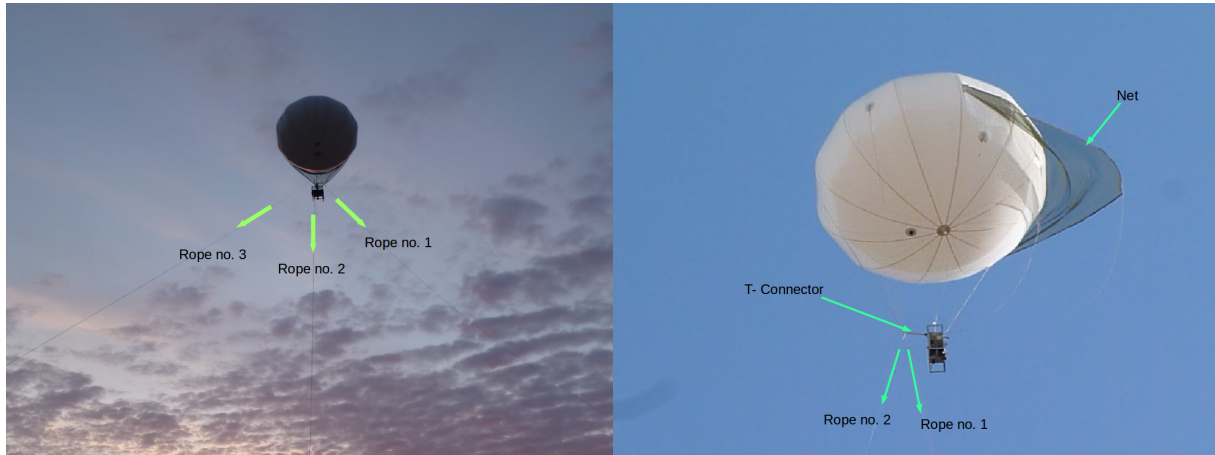


Figure 2. The wind-rose corresponding to 56 hours of flight, reported in the local coordinate system of the sensor. The numbers on the plot indicate sampling records collected at 10 Hz.

Figure 3a shows the balloon operation in an unstable atmosphere with high winds when three ropes are used to stabilize it. A sudden drag force on the gondola may drive the system out of its stable position momentarily. Hence it may affect the quality of measurements by creating instabilities. Such phenomenon can be prevented by deploying extra ropes connecting the gondola directly to ground operators. The tension in these ropes balances the sudden drag force exerted on the system. This arrangement places the gondola in a quasi-stationary position in the air that indeed helps the stability of measurement in gusty

conditions. Figure 3b shows the balloon operation in a stable atmosphere with low winds when only two ropes are used to stabilize it.



(a) TANAB and three stabilizing ropes

(b) TANAB and two stabilizing ropes

Figure 3. TANAB at different atmospheric stability conditions tethered with two or three stabilization ropes in the mining facility.

10 A T-connector connects the balloon to the gondola using ropes allowing the gondola to hang freely while minimizing the pitch and roll angles to result in better measurements from a levelled gondola. Figure 4 shows the distributions for pitch and roll angles recorded by TriSonica™ Mini's compass over 56 flight hours. According to the bar charts, the gondola is level within $\pm 5^\circ$ of pitch and roll angles more than 90% of the time. The gondola only rotates in the yaw direction when the main wind direction changes. The gondola is positioned 2 m below the balloon, so the effects of the balloon motion on the gondola are reduced.

15 2.2 Mini Weather Station

The TriSonica™ Mini weather station is an ultrasonic anemometer manufactured by Anemoment™ and is mounted onto the gondola of TANAB^{5, 5}. This mini weather station is ideal for applications that require a miniature, lightweight, and low velocity anemometer, and are suitable particularly for airborne systems. It has a measurement path length of 35 mm and a weight of 50 gr. The light weight makes it an ideal candidate to use with the TANAB system. It can measure the 3D wind speed, air temperature, relative humidity, and the barometric pressure at a sampling rate up to 10 Hz. The open path provides the least possible distortion of the wind field. Its design with four measurement pathways provides a redundant measurement and the path with the most distortion is removed from the calculations to provide accurate wind measurements. It is also equipped with a compass and a tilt sensor. Because of its low power consumption (only 30 mA at 12 V), it is highly power efficient and can record data for hours.

⁵

⁵<https://www.anemoment.com/>, last access: 10 January 2019

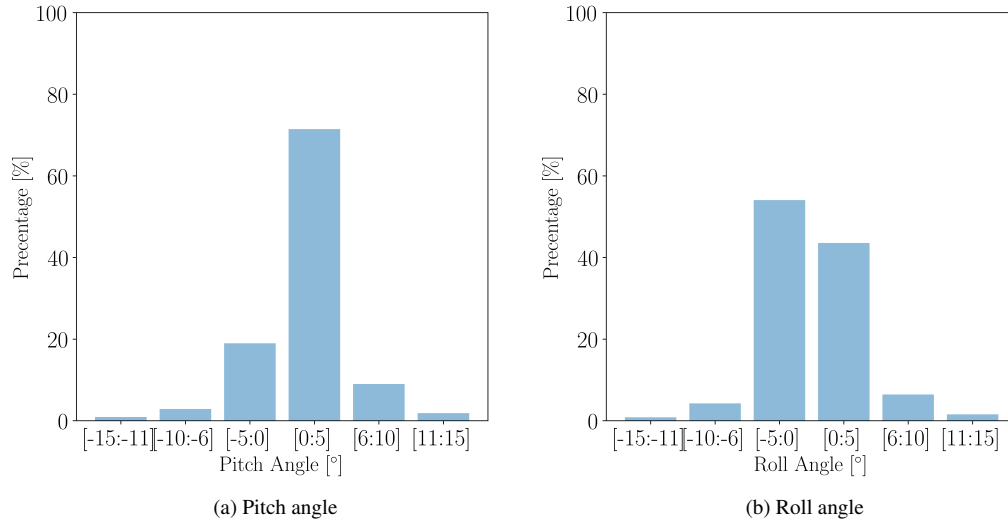


Figure 4. Distribution of pitch and roll angles recorded by TriSonica™ Mini's compass.

25 A data logger by Applied Technologies Inc.⁶ is used as the data synchronization and data collection device for the TriSonica™ Mini weather station. This data logger records the measurements on an SD card onboard that can be retrieved after every flight. In addition, the TriSonica™ Mini can be monitored or programmed using serial communication via the data logger. The TriSonica™ Mini weather station and the data logger are powered using a 12 V Lithium-Polymer (LiPo) battery.

The anemometer measures wind speed in the range $0 - 30 \text{ m s}^{-1}$ at a resolution of 0.1 m s^{-1} . The accuracy of the measurement is $\pm 0.1 \text{ m s}^{-1}$ ($0 - 15 \text{ m s}^{-1}$) or $\pm 2\%$ ($15 - 30 \text{ m s}^{-1}$). Wind direction is measured at a resolution of 1° and an accuracy of $\pm 1^\circ$. Vertical winds are measured appropriately if the approach elevation angle is within $\pm 30^\circ$, a condition that is typically met under calm wind conditions in-over smoothly varying topography. Temperature is measured in a range from -25°C to $+80^\circ\text{C}$ with a resolution of 0.1°C and an accuracy of $\pm 2^\circ\text{C}$. Pressure is measured in the range $50 - 115 \text{ Pa}$ with an accuracy of $\pm 1 \text{ kPa}$. The tilt sensor measures the pitch and roll with an accuracy of $\pm 0.5^\circ$. The compass measures the magnetic heading with an accuracy of $\pm 5^\circ$.

2.3 Thermal Camera and Flight Controller

The uncooled thermal camera used is the Zenmuse XT, 19-mm lens, manufactured by FLIR-Systems⁷:DJI.⁷ This radiometric camera has a resolution of 640×512 , and it is capable of capturing thermal images at 30 Hz. This camera is powered by DJI and mounted underneath the gondola of the TANAB using a gimbal kit. The camera is operated by the DJI N3 flight controller⁸

⁶<http://www.apptech.com/>, last access: 10 March 2019

⁷

⁷<https://www.dji.com/ca/zenmuse-xt>, last access: 15 February 2019

⁸<https://www.dji.com/>, last access: 15 February 2019

with associated hardware securely attached to the gondola of the TANAB. This aerial imaging device is designed to be mounted and operated using drone aircraft systems ~~while it is the first time such a camera has been considered for a balloon system~~. The camera gimbal system compensates for gondola movement due to wind to keep the camera orientation. The camera system roll angle is generally very close to zero due to the self-stabilization of the device. Nevertheless, the gondola itself is connected to the balloon using ropes and a swivel mechanism to hang freely without being influenced by aerodynamic vibrations of the balloon envelop. The gondola is designed to include a safety feature to protect the camera from impact damage. The DJI Lightbridge 2 (LB2) controller is used with either an iOS or Android device to communicate with the N3 and Zenmuse XT during flight. The LB2 has a maximum communicable range for image transmission of 5 km. Pictures and videos can be recorded with precision while the gondola is in flight as the camera can move independently with respect to the gondola. During flight, the N3 and DJI Zenmuse XT function in parallel such that the GPS location and altitude of the gondola as well as tilt and heading angles of the camera are recorded by the N3 and are included in the ~~meta-data~~ metadata of each image. All GPS information and associated gondola parameters are recorded and stored within the N3 controller and can be retrieved for later analysis using a mini USB connection. The N3 flight controller is equipped with two IMUs, a GNSS, and Compass system.⁹ This flight controller is not capable of Real-Time Kinematic (RTK) positioning.

Post processing of GPS data with Precise Point Positioning (PPP) or RTK methods have been noted to reduce geographical positioning error down to a few centimetres (Satirapod et al., 2003; Remondino et al., 2011; Padró et al., 2019). On the other hand, georeferencing capabilities of GNSS and IMU systems are known to have horizontal geographical positional errors of a few meters (Bláha et al., 2011; Chiabrando et al., 2013; Zhuo et al., 2017). Direct georeferencing without the use of differential corrections provide GPS coordinates of a land point within 2 to 5 m of accuracy (Turner et al., 2014; Whitehead et al., 2014). For the purpose of the TANAB system, direct georeferencing with no corrections were used. Vertical positioning of GNSS/IMU systems have been noted in the literature to be prone to significant errors of up to 50 m especially when compared to other RTK and PPP methods (Eynard et al., 2012; Padró et al., 2019). As a result, vertical positioning of the TANAB gondola was completed by considering the hypsometric equation as per Eq. 7 using the airborne barometric pressure and temperature recorded by the ultrasonic anemometer with respect to ground level barometric pressure at the beginning of each TANAB launch.

Even without the use of RTK or PPP, the resulting temperature maps for the surface of the mining facility have a higher spatio-temporal resolution as compared to conventional satellite based sensors. The MODIS¹⁰ located on both the Terra and Aqua satellites records two distinct thermal images daily, approximately three hours apart at a 1 km × 1 km spatial resolution (Crosson et al., 2012; Kumar, 2014; Liu et al., 2017). The Advanced Baseline Imager located on the GOES satellites¹¹, are capable of capturing thermal images every 5 min with a spatial resolution of 2 km × 2 km (Cintineo et al., 2016; Schmit et al., 2017). Furthermore, Landsat satellites are capable of recording Thermal Infrared (TIR) images. The Landsat 7 ETM+¹² can capture TIR images at a spatial resolution of 60 m × 60 m and the Landsat 8 TIRS can record TIR images at a spatial resolution of 100

⁹http://dl.djicdn.com/downloads/N3/20170825/N3_User_Manual_En_v1.4.pdf, last access: 15 February 2019

¹⁰<https://modis.gsfc.nasa.gov/about/>, last access: 20 March 2019

¹¹<https://www.nasa.gov/content/goes-overview/index.html>, last access: 20 February 2019

¹²<https://landsat.gsfc.nasa.gov/the-enhanced-thematic-mapper-plus/>, last access: 20 February 2019

m \times 100 m.¹³ Both Landsat satellites have a time resolution of 16 days (Chastain et al., 2019). Although errors are inherently introduced into the directly georeferenced surface temperatures, the advantages of collecting both high spatial and temporal resolution LST data from the TANAB platform outweigh geographical positioning error from the GNSS/IMU system.

15 The images taken by the thermal camera are saved to an onboard micro SD card. The thermal camera can record images in four different file types including JPEG, R-JPEG, TIFF T-Linear Low, and TIFF T-Linear High. In our study we used R-JPEG. Using the recorded information for each image, the GPS coordinates (latitude and longitude) for individual pixels within each image can be derived. Through using additional software, surface temperature from individual pixels are calculated.

2.3.1 Image Processing Methodology

20 The images obtained from field observations were processed utilizing Python (version 3.6), ExifTool (version 10.94), ImageMagick (version 7.07), and mathematical relationships to ~~calculate Land Surface Temperature (LST)~~ LST in Kelvin from pixels for each image. Furthermore, mathematical and trigonometric relationships were employed to directly georeference the image pixels according to the World Geodetic System 1984 (WGS84) datum by deriving decimal degree latitude and longitude values. ExifTool is a software package used to read, write, and edit metadata from images. Within ExifTool, different tags are
25 used depending on the camera manufacturer to extract relevant metadata. Using the FLIR tag in ExifTool, important metadata from each image was derived from the onboard airborne flight controller. ExifTool is executed through the Linux terminal window. ImageMagick is a software used to edit and create images. When extracting the raw data signal value recorded by the thermal camera, ImageMagick is used in conjunction with the ExifTool tag function. ExifTool specifies the data to return from each image and ImageMagick specifies the exact pixel to extract from the image.

30 Through using ExifTool, the following metadata parameters from each image are obtained: latitude of camera gimbal, longitude of camera gimbal, camera gimbal ~~roll degree, camera gimbal~~ yaw degree, camera gimbal pitch degree, gondola roll degree, gondola ~~yaw degree, gondola~~ pitch degree, ~~Planck constant R_1 , Planck constant R_2 , Planck constant B , offset Planck constant O , Planck constant F~~ , date image was recorded, altitude of the gondola (only if the TriSonica™ Mini was not operational when the image was captured), the raw signal value recorded by the thermal camera, and the reflected apparent temperature. When airborne, the thermal camera is stabilized, as a result, the camera system is independent of the gondola up to the camera's mechanical range. As a result, images beyond the mechanical extent of the camera were omitted (gondola roll
5 greater than 45 ° or less than -45 ° ~~and, gondola~~ pitch greater than 45 ° and less than -135 °, and gimbal pitch greater than or equal to 0 °, where the recorded pitch angle is located at the center-centre of the image, as measured from the horizontal plane). Positive pitch angles primarily include the sky and negative pitch angles primarily include the Earth's surface. Furthermore, camera gimbal pitch angles greater than -2 ° were removed from the image processing technique as these images were very oblique and would have contributed to LST errors. Camera gimbal pitch angles greater than -30 ° are known to introduce
10 possible errors into the LST calculation¹⁴.¹⁴ Since the TANAB was flown up to a maximum of 150-200 m above grade

¹³<https://landsat.gsfc.nasa.gov/landsat-8/landsat-8-overview/>, last access: 20 February 2019

¹⁴

¹⁴https://dl.djicdn.com/downloads/zenmuse_xt/en/sUAS_Radiometry_Technical_Note.pdf, last access: 15 February 2019

ground level, only some images greater than -30° were omitted from the image analysis as a compromise between LST spatial distribution and LST accuracy. Additionally, any images with incorrect latitude or longitude values were omitted. For georeferencing simplicity, images recorded with a camera gimbal pitch less than or equal to -76° were omitted (including nadir images) to ensure that the pitch angle for the bottom of each image was greater than -90° . As per the thermal camera specifications, the vertical field of view of the camera is 26° and the pitch angle for the bottom of an image is equivalent to the camera gimbal pitch angle minus one half of the vertical field of view. This condition was included to avoid negative horizontal distances with respect to the camera/gondola. ~~The altitude of the gondola and camera were derived from atmospheric pressures recorded by the TriSonicaTM according to the pressure height equation (Eqn. 7).~~ Timestamps from each image and the TriSonicaTM Mini data were compared to determine the altitude of the gondola when each image was recorded. The pixel row for images that correspond to sky are calculated such that pixels including sky are omitted.

With georeferencing completed, LST values were derived for every 64th pixel across each row. Pixel rows were selected based on a geometric step function such that the majority of the calculated LST coordinates were located near the top of each image. This ~~was~~ method was chosen as the pixels closer to the top of the image would cover more land surface area.

Although the camera utilized in this paper used an uncooled microbolometer to record thermal energy, it was calibrated against known surface temperatures. The use of the Stefan-Boltzmann Law is not applicable because the DJI Zenmuse XT is based on FLIR radiometric thermal imaging technology where the recorded microbolometer value is represented as a signal value comprising energy recorded from the surface, reflected energy from the surface, and atmospheric radiation energy (Zeise et al., 2015). Furthermore, it should be noted that many FLIR radiometric thermal imaging cameras (including the DJI Zenmuse XT) have a 14-bit radiometric resolution capable of recording pixel signal values derived from the camera's A/D converter between 0 and 16383 (FLIR-Systems, 2012; Sagan et al., 2019).¹⁵ The radiometric image pixel signal values can be converted to temperature in Kelvin by performing a radiometric calibration between the recorded pixel signal values and corresponding object surface temperatures (Budzier and Gerlach, 2015). The relationship between the radiometric signal value and the object temperature can be approximated with a Planck curve, as noted by Horny (2003) and similar to Martiny et al. (1996), in Eq. 1 (Budzier and Gerlach, 2015)

$$U_{\text{Obj}} = \frac{R}{\exp\left(\frac{B}{T_{\text{Obj}}}\right) - F} - O, \quad (1)$$

where U_{Obj} represents the radiometric pixel signal value, T_{Obj} represents the surface temperature of the object, R represents the uncooled camera system response, B is a constant derived from Planck's Radiation Law, F accounts for the non-linear nature of the thermal camera system, and O represents an offset (Budzier and Gerlach, 2015). Eq. 1 is rearranged to solve for T_{Obj} as per Eq. 2 (Budzier and Gerlach, 2015; Tempelhahn et al., 2016)

$$T_{\text{Obj}} = \frac{B}{\ln\left(\frac{R}{U_{\text{Obj}} + O} + F\right)}. \quad (2)$$

¹⁵<https://www.dji.com/ca/zenmuse-xt> last access: 15 February 2019

These four values, R , B , F and O were calculated by the camera manufacturer through the completion of a non-linear regression from the radiometric calibration data (the blackbody surface temperature and the corresponding radiometric pixel signal value) (Budzier and Gerlach, 2015). However, the imaged surface and R represents numerical constants that are dependent on physical camera parameters as determined by the manufacturer during calibration (Martiny et al., 1996). authors of this study performed a non-linear regression to fit the $R = R_1/R_2$, B , O , and F constants based on land use type and known surface temperatures in an off-site calibration activity. Note that the complex mining environment did not allow an on-site calibration activity due to access restrictions and safety measures. The raw signal values-value (U_{Tot}) recorded by the camera is governed by Eq. 3 as described by FLIR-Systems (2010) Usamentiaga et al. (2014)

$$U_{Tot} = \epsilon\tau U_{Obj} + \tau(1 - \epsilon)U_{Refl} + (1 - \tau)U_{Atm}, \quad (3)$$

where U_{obj} - U_{Obj} is the raw output voltage of a blackbody recorded by the thermal camera, U_{tot} is the total raw output voltage recorded by the thermal camera, U_{refl} in a laboratory calibration experiment in the absence of reflection and atmospheric influence in the measured signal. To back calculate U_{Obj} , U_{Refl} and U_{Atm} must be determined. U_{Refl} is the theoretical raw camera output voltage for a blackbody based on the assumed reflective temperature and U_{atm} of temperature T_{Refl} according to the calibration. T_{Refl} is the effective temperature of the object surroundings or the reflected ambient temperature. U_{Atm} is the theoretical raw output voltage of a blackbody based on the assumed atmospheric temperature. ϵ is the emissivity of the blackbody-object and τ is the atmospheric transmissivity. The transmissivity of the atmosphere is generally close to 1.0 (Usamentiaga et al., 2014) under clear weather conditions, so U_{Atm} does not have to be calculated. From the camera metadata, the assumed reflective temperature (T_{Refl}) was 22 °C. This value was extracted using ExifTool. The U_{refl} - U_{Refl} value was calculated using (Zeise and Wagner, 2016) the same Eq. 1 (Zeise and Wagner, 2016)

$$U_{Refl} = \frac{R}{\exp\left(\frac{B}{T_{Refl}}\right) - F} - O, \quad (4)$$

where $R = R_1/R_2$, B , F and O are Planck constants of the camera that could be extracted through ExifTool as detailed above (default constants) or set using fitted constants separately as detailed in Sect. 3.3.

The Emissivity-emissivity of the land surface was determined to be a function of geographic position. The Moderate Resolution Imaging Spectroradiometer (MODIS) instrument-MOD11B3 data product acquired from MODIS was used to derive Land Surface Emissivity (LSE) (Wan et al., 2015). The monthly data product with a resolution of 6 km was used to derive LSE for data collected during the observation campaign in May 2018. The emissivity values were calculated using bands 29, 31, and 32-values-32. Since the thermal camera used a Longwave Infrared Radiation (LWIR) detector, radiation within the 7.5 μm to 13.5 μm spectral range was included in the camera voltage output^{16, 16}. MODIS band 29 records radiation within the 8.4 μm to 8.7 μm spectral range, band 31 records radiation within the 10.78 μm to 11.28 μm spectral range, and band 32 records radiation within the 11.77 μm to 12.27 μm spectral range. These three bands are used in conjunction with the Broad

¹⁶

¹⁶<https://www.dji.com/zenmuse-xt/info/>, last access: 15 February 2019

~~Band-BroadBand~~ Emissivity (BBE) derivation to calculate emissivity as a function of geographical area (Wang et al., 2005).

The BBE formula used is

$$BBE = a\epsilon_{29} + b\epsilon_{31} + c\epsilon_{32}, \quad (5)$$

where a , b , and c are constants that vary based on the land surface material. Wang et al. (2005) determined that the constants a , b , and c do not vary significantly between soil, vegetation, or anthropogenic materials. However, water~~ice~~, ~~ice~~, and snow resulted in noticeably different BBE coefficients. Based on Wang et al. (2005), the BBE coefficients for a , b , and c were chosen to be 0.2122, 0.3859, and 0.4029, respectively.

~~The output voltage value for the object was then calculated. Finally, the LST value as per the thermal camera was derived using~~ After quantifying U_{Ref} , it is possible to back calculate U_{Obj} by rearranging Eq. 3 and finally calculate T_{Obj} via Eq. 2.

20 3 Calibration Experiments

~~In order to check the validity of the high frequency data from the anemometer onboard of TANAB, the anemometer performance was validated against calibrated sensors prior to the field campaign in a series of wind tunnel and outdoor calibration experiments.~~

25 3.1 Wind Velocity Calibration ~~The mounted anemometer performance was characterized in a highly turbulent flow generated by a wind tunnel at the University of Guelph.~~

All the experiments were conducted in the University of Guelph's wind tunnel, which is an open circuit tunnel designed for turbulent boundary layer research. The cross sectional area is $1.2 \text{ m} \times 1.2 \text{ m}$. The tunnel is 10 m long. The tunnel's air speed is controlled by a gauge that sets the fan speed. The tunnel achieves wind speeds up to 10 m s^{-1} . The turbulence intensity is typically less than 2 % if no roughness blocks are placed upstream of the flow. The Reynolds number characterizes the turbulence level of the fluid flow and is defined as the ratio of the inertial to viscous forces given by $Re = \frac{\rho \times U \times L}{\mu}$, where U is the flow velocity, L is the characteristic length scale of the system (commonly, the hydraulic diameter of the wind tunnel), and μ and ρ are the dynamic viscosity and density of the fluid, respectively. In the present study, the wind tunnel's Re number varied between 150,000 and 1,100,000. Considering the size of the wind tunnel, it is capable of generating eddies as large as its physical dimensions.

The performance of the gondola (or the effects of the frame on TriSonica™ Mini measurements) in reading the mean and turbulence statistics of the flow field is studied with respect to the R.M. YOUNG 81000 ultrasonic anemometer, which is already calibrated, ~~is and~~ used for cross comparison to derive the calibration coefficients for the ~~anemometer~~ TriSonica™ Mini using line fits. By adding multiple degrees of freedom, the set-up for this test was designed to further simulate the gondola's movements in the real atmosphere. The gondola is attached to the ceiling with two ropes (featuring the ropes to the balloon) and a single rope to the bottom floor (resembling the ground controller). Now, the gondola faces the main flow (as it does in the real atmosphere), but it has some degrees of freedom to slightly wobble. The azimuth angle, elevation angle, and wind

levels were changed, independently, to derive calibration coefficients for both mean and turbulence statistics as measured by the TriSonica™ Mini and calibrated against the R.M. YOUNG 81000. Both sensors were set up at similar airflow condition while wind speed was varied at ~~three or ten different wind speed~~ ~~few wind~~ levels in the range ~~2—10~~ ~~2-10~~ m s^{-1} . At each wind speed level, data recording continued for 5 min. Each recording was time averaged to calculate mean and turbulence statistics. ~~It is customary to use notation associated with Reynolds averaging to decompose a signal~~

In this study the velocity along the X into mean \bar{X} and turbulent x components such that $X = \bar{X} + x$. The calibration factors were derived for the x , y , and z components of mean velocity, i.e. \bar{U} , \bar{V} and \bar{W} , in separate experiments Y , and Z directions are denoted by U , V , and W . Further, Reynolds decomposition is used to express each velocity component as the sum of the time-averaged and fluctuating components: $U = \bar{U} + u$, $V = \bar{V} + v$, and $W = \bar{W} + w$, where the over-lined quantities are time averages and lower case quantities are instantaneous fluctuations. Furthermore variance and covariances of the fluctuations are represented by $\overline{u^2}$, \overline{uv} , etc. The calibration equations obtained are used for correcting the field measurement data from the TANAB.

3.2 Temperature Calibration

~~Temperature~~ ~~Temperatures~~ measured by TriSonica™ ~~is~~ ~~Mini~~ are calibrated with respect to the Campbell Scientific HMP60 sensor¹⁷.¹⁷ The latter collected minute-averaged temperatures, to which the TriSonica™ ~~Mini~~ temperatures were also averaged and compared. The experiment was carried out under a set of ~~climate~~ ~~weather~~ conditions to cover a wide range of temperatures outdoors.

3.3 Thermal Camera Calibration

In an attempt to quantify surface temperature measurement inaccuracies of DJI Zenmuse XT, an experiment was conducted to fit the R , ~~which can be corrected~~ B , O and F parameters as per Eq. 2. Three radiometric images were recorded approximately thirty seconds apart every hour between 0600 Local Daylight Time (LDT) and 2300 LDT over a two day period for four distinct surfaces including water, soil, developed land (urban surfaces), and grass. Each radiometric image captured included a certified thermometer, which measured a corresponding temperature for each land surface. The time delay of approximately thirty seconds between each consecutive image was chosen as Olbrycht and Więcek (2015) noted that uncooled thermal cameras without recent calibration experienced temperature drift as much as 1 K per minute.

FLIR Tools was used to calculate surface temperatures from the radiometric images recorded by the DJI Zenmuse XT on top of the certified thermometer. For each hourly interval, the average of the surface temperatures from the thermal camera were calculated and were used in the following calculations and figures. The pixel value (U_{Obj}) was calculated using Eq. 1, where constants R , B , O and F were defined during camera factory calibration and stored in the metadata of each image. As per Table 1 these values are referred to as the default camera constants. The temperatures recorded by the calibrated thermometer were scaled appropriately as the outdoor field test occurred in Guelph, Ontario, Canada which is 334 m above sea level.

¹⁷

¹⁷<https://www.campbellsci.com/>, last access: 10 January 2019

The empirical line method as described by Smith and Milton (1999) was used to relate A/D Counts to the corresponding certified temperatures to calibrate (fit) the R , B , O and F constants as in Fig. 5. Using the Non-Linear Least-Squares Minimization and Curve-Fitting for Python (LMFIT) library,¹⁸ the constants were fitted and residuals were minimized for each specific surface material imaged during the calibration experiment using Eq. 2. The default and calibrated camera constants are detailed in Table 1. Fig. 5 displays the experimental, default, and calibrated temperatures as a function of camera pixel signal value for water, soil, developed land, and grass, respectively. The non-linear curve fitting library used the certified temperature obtained during the experiment, the corresponding pixel signal value, and Eq. 2 to derive the calibrated camera parameters.

Table 1. Default and calibrated camera constants.

Camera Parameters	R	B	O	F
Default	366545	1428	-342	1
Calibrated Water	549789	1507	-171	1.5
Calibrated Soil	549800	1510	-171	1.5
Calibrated Developed Land	247614	1322	-513	1.5
Calibrated Grass	314531	1391	-513	1.5

Fitting of the camera constants for each material resulted in reduced bias and Root Mean Square Error (RMSE) values for water, soil, developed land, and grass, respectively, as compared to the bias and RMSE values considering default camera constants, as shown in Table 2. Gallardo-Saavedra et al. (2018) reported that the manufacturer stated accuracy of the FLIR Vue Pro 640 thermal camera was ± 5 K. Kelly et al. (2019) also used the empirical line calibration method for a FLIR Vue Pro 640 thermal camera and determined that the accuracy of the thermal camera was ± 5 K, which is in agreement with our findings.

Table 2. Error statistics, bias, and Root Mean Square Error (RMSE), in temperature measurement associated with default and calibrated camera constants.

Surface	Water	Soil	Developed Land	Grass
Default bias	5.18	4.81	1.83	2.07
Default RMSE	5.83	5.34	3.91	2.34
Calibrated bias	0.27	-0.09	0.13	-0.24
Calibrated RMSE	2.40	1.57	3.31	1.11

The fitted R , B , O and F constants for water, soil, developed land, and grass were applied to surfaces in the actual mining facility with coordinates corresponding to the closest land use categories. Furthermore, the emissivity of the surface was considered by applying the BBE Eq. 5 derived by Wang et al. (2005). The boundaries for each land use type were determined by visually inspecting the Landsat 8 Operational Land Imager image recorded on May 17, 2018 with a pixel resolution of 30

¹⁸<https://lmfit.github.io/lmfit-py/index.html>, last access: 10 April 2019

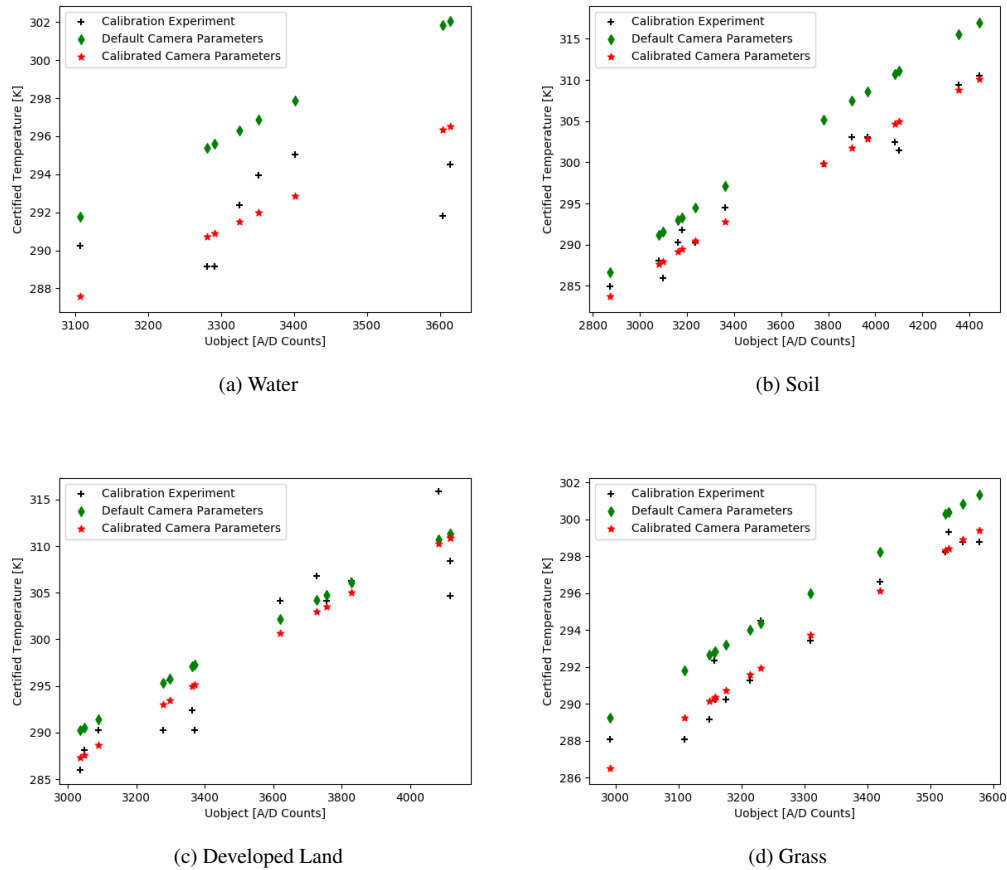


Figure 5. Certified temperature compared to radiometric image pixel signal value for Water, Soil, Developed Land, and Grass.

m. In QGIS, land use type corresponding to geographic coordinates with a spatial resolution of 1 km were applied and the surface temperatures were calculated according to Fig. 6.

10 4 Field Experiments and Results

The TANAB system was launched at a mine facility in northern Canada (above 56 °N) for an environmental monitoring field campaign in May 2018. A schematic of the mine facility can be seen in Fig. 6. The depth of the mine is approximately 100 m.

TANAB flew for ~~more than 50~~ 56 hr collecting data. The objectives of the measurements were to determine dynamics of the atmosphere at different diurnal times (e.g. day versus night) and locations (near tailings pond versus inside the mine). Such dynamics determine the transport of green house gases (GHGs) and therefore emission fluxes. Measurements of the GHG fluxes were not the objective of this paper and will be addressed elsewhere.

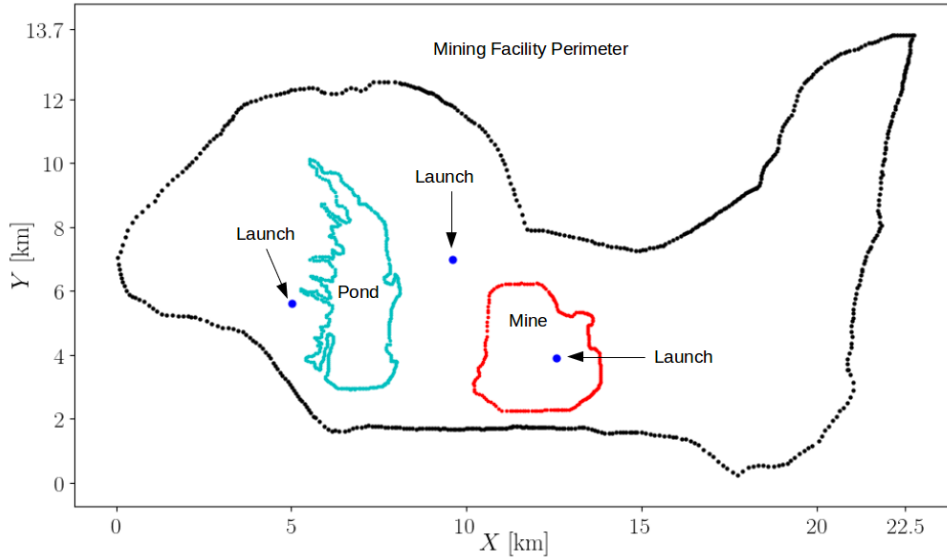


Figure 6. A schematic of the mine facility. The black dots represent the outline of the entire facility. The green dots represent the outline of the tailings pond, and the red dots represent the outline of the mine. The blue dots are the balloon launch locations.

Surface level transport mechanisms strongly depend on atmospheric dynamics. Factors such as wind speed, atmospheric diffusion coefficient, and thermal stability greatly influence emission fluxes. As a result, the particular focus of this study is measurement of surface level meteorology in the lowest 200 m ~~altitudes~~ altitude and earth surface temperature. The launch details are summarized in Table 3.

Vertical transport of momentum and heat are predominant processes within the ~~the~~ surface layer of the ABL (Businger et al., 1971) and deriving the vertical fluxes of momentum and heat from wind speed and temperature profile measurements can be achieved using TANAB. Turbulence kinetic energy is one of the key measures of turbulence in the atmosphere as it controls the vertical and horizontal mixing (Lenschow et al., 1980; Svensson et al., 2011; Shin et al., 2013; Canut et al., 2016). It is also used for the parameterization of small-scale turbulent transport processes, such as vertical fluxes, when the smaller scale motions are not modelled directly (Aliabadi et al., 2018b). The equation that represents turbulence kinetic energy is

$$k = \frac{1}{2}(\overline{u^2} + \overline{v^2} + \overline{w^2}), \quad (6)$$

where $\overline{u^2}$, $\overline{v^2}$, and $\overline{w^2}$ are variances of turbulent velocity fluctuations along the along-wind (x -), cross-wind (y - and), and in the vertical (z) directions. Another coordinate system to analyze mean wind velocity components and wind velocity fluctuations is

Table 3. Tethered And Navigated Air Blimp (TANAB) ~~Launch~~ launch details. Times are in Local Daylight Time (LDT).

Experiment	Location	Start Date	Start time	End time	No. of profiles	Experiment time
1	Tailings pond	2018:05:07	21:41:00	02:47:00	14	05:06:00
2	Tailings pond	2018:05:09	03:30:00	04:00:00	02	00:30:00
3	Tailings pond	2018:05:10	02:30:00	08:30:00	21	06:00:00
4	Tailings pond	2018:05:15	04:55:00	11:00:00	22	06:05:00
5	Mine	2018:05:18	04:12:00	11:12:00	20	07:00:00
6	Mine	2018:05:19	18:52:00	23:15:00	17	04:23:00
7	Mine	2018:05:21	11:00:00	12:17:00	04	01:17:00
8	Mine	2018:05:23	01:47:00	05:30:00	10	02:43:00
9	Mine	2018:05:24	11:19:00	14:25:00	12	03:06:00
10	Mine	2018:05:27	14:38:00	17:50:00	18	03:12:00
11	Tailings pond	2018:05:30	10:55:00	18:57:00	24	08:02:00
12	Tailings pond	2018:05:31	11:07:00	14:43:00	08	03:36:00

the *along-wind* coordinate system, in which the horizontal axis is rotated toward the direction for mean horizontal wind velocity vector (Aliabadi et al., 2016e) directions. We used the hypsometric equation to calculate the altitude of the measurement above surface (Bolanakis et al., 2015; Stull, 2015)

$$z_2 - z_1 \approx a \bar{T}_v \ln \left(\frac{P_1}{P_2} \right), \quad (7)$$

where P_1 and P_2 are the pressure measurement at two altitudes z_1 and z_2 . The system measured pressure in mBar although the equation is insensitive to the units of pressure. The unit of altitude is m. \bar{T}_v is the average virtual temperature between altitudes z_1 and z_2 . The constant $a = R_d/g$ is equal to 29.3 mK^{-1} (Stull, 2015). Given the uncertainty of temperature and pressure measurement, the uncertainty of altitude measurement is estimated as 1.2 m.

4.1 Sampling Time

TANAB measured wind speed, the turbulence kinetic energy, variances, and fluxes for both momentum and heat rigorously. Each balloon launch lasted approximately 15–30 min while the tether was carefully controlled to obtain a profile with constant ascent and descent rates. The sampling time for calculating the mean and turbulence quantities were 3 min while typically it is 10 to 30 min for flux tower measurements (Aliabadi et al., 2018a). For turbulence statistics, the time series is first detrended to ensure that background weather variations that have inherently very large time and length scales are filtered out without influencing the turbulence statistics calculations. It is known that finite time sampling, instead of ensemble averaging, will introduce random and systematic errors in the prediction of turbulence statistics such as variances and fluxes (Lenschow et al., 1994). While random errors could result in overprediction or underprediction of turbulence statistics, the systematic errors

always underpredict the magnitude of the turbulence statistic. These errors have been reported in an aircraft campaign to be anywhere in the range 10 to 90 %-% of the measured value (Aliabadi et al., 2016b). While repeated measurements, increasing the averaging time, and detailed error analysis are possible to eliminate such errors from predictions, the focus of this study was not to investigate errors associated with finite sampling time. Nevertheless, operating the TANAB involves a delicate choice of the sampling time. On one hand, short sampling times have inherent large errors but provide profiles at high vertical resolutions. On the other hand, long sampling times have inherent small errors but provide profiles at low vertical resolutions.

5 4.2 Diurnal Variation in Wind Speed and Turbulence Statistics

It was observed that both wind speed (Fig. 7) and turbulence kinetic energy (Fig. 8) exhibited a significant diurnal variation, indicating calm conditions at nights and early mornings, when atmospheric diffusion coefficient is low, and gusty conditions in the mid-afternoons when the atmospheric diffusion coefficient is high. When calculating statistical percentiles, the data is combined over all altitudes and aggregated for both the mine and tailings pond locations.

10 Similar diurnal variations can be also observed in the case of other turbulence statistics such as ~~vertical momentum flux (or Reynolds stress) \overline{sw}~~ along-wind and cross-wind vertical momentum fluxes, \overline{uw} and \overline{vw} , respectively, vertical sensible kinematic heat flux $\overline{w\theta}$, potential temperature variance $\overline{\theta^2}$, and vertical velocity variance $\overline{w^2}$ (Fig. 9). The measurement of weak turbulence in the nocturnal boundary layer is also very important as it leads to weak turbulent dispersion and large accumulation of heat or atmospheric constituents in the lower part of the stable boundary layer (Mahrt and Vickers, 2003, 2006). Periods of strong
15 stability with intermittent turbulence can also occur in the nocturnal boundary layer (Businger et al., 1971; Mahrt, 1999).

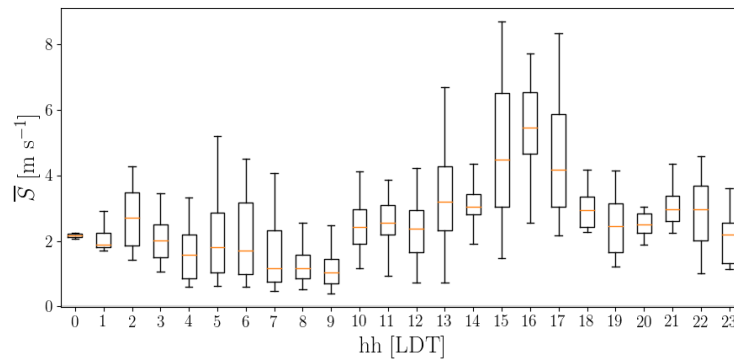


Figure 7. Diurnal variation of wind speed. At each hour observations are plotted using statistical percentiles (5th, 25th, 50th, 75th, and 95th); Local Daylight Time (LDT).

4.3 Vertical Variation of Mean and Turbulence Statistics

Figure 10 shows the vertical profiles of turbulence statistics for different diurnal periods (4-hr intervals) of the day. 50th percentiles are shown for all observations. Data is binned in 20-m height intervals. The vertical structure of the atmosphere

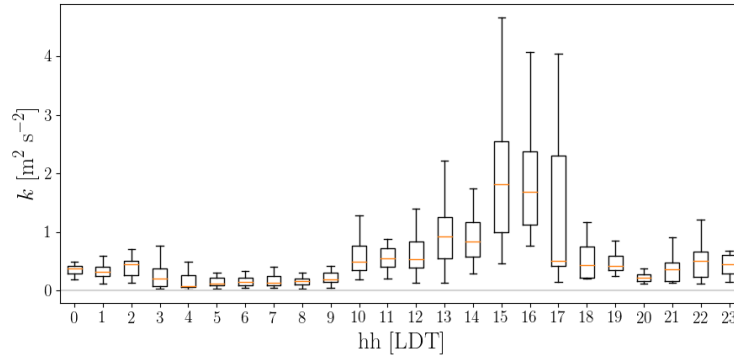


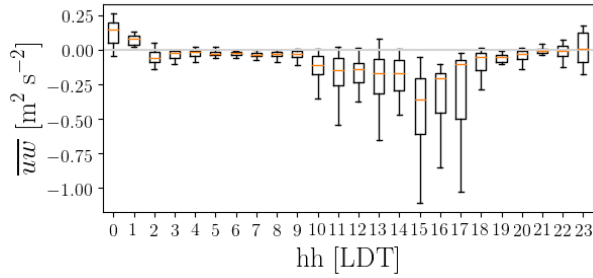
Figure 8. Diurnal variation of turbulence kinetic energy. At each hour observations are plotted using statistical percentiles (5th, 25th, 50th, 75th, and 95th); Local Daylight Time (LDT).

near the surface can be understood while analyzing the turbulence kinetic energy k , ~~variance of along-wind horizontal wind velocity s^2 , vertical momentum flux $\overline{w\theta}$ and cross-wind vertical momentum fluxes, \overline{uw} and \overline{vw} , respectively~~, vertical sensible kinematic heat flux $\overline{w\theta}$, variance of potential temperature $\overline{\theta^2}$, and variance of vertical wind velocity $\overline{w^2}$.

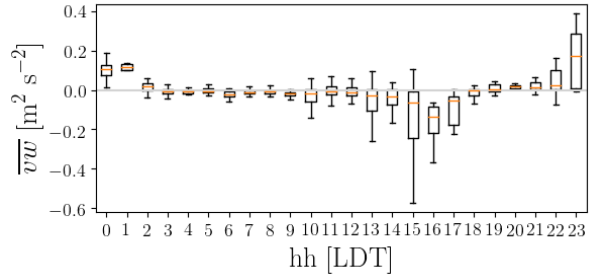
It is noteworthy that maximum flight altitude is usually less under windy conditions, therefore most profiles obtained under windy conditions in mid day are shorter than those obtained under calm conditions at night and early mornings. It is observed that in the surface layer within ABL the highest gradients of turbulence properties occur at the lowest 100 m. This statement must be considered with caution. Certainly it is only valid for the short length and time scales considered as a result of the 3-min time averaging. The diurnal variation of turbulence statistics are clear from the plots. The magnitude for most statistics are greatest during mid day time interval 1200–1600 LDT due to gusty conditions, while the magnitudes are smallest during night-time and early-morning time interval 0400–0800 LDT associated with calm conditions. The along-wind vertical momentum flux \overline{uw} is always negative, confirming boundary layer physics that imply momentum should sink to the surface due to skin drag with turbulent processes. This also implies confidence in the measurement of velocity fluctuation covariance. The vertical sensible kinematic heat flux $\overline{w\theta}$ is negative at night time but positive during day time. ~~This confirms that the earth surface acts as a heat sink at night time due to heat loss by radiation to the sky, and that the earth surface acts as a heat source during day time due to heat gain by radiation from the sky.~~ The variance of potential temperature $\overline{\theta^2}$ is not strictly diminished under calm night time conditions. This can be interpreted as the presence of differential near surface horizontal gradients of temperature due to thermal structures caused. It is expected that such gradients must exist because of the heterogeneity of land surface and anthropogenic activities in such a complex terrain of a mining facility.

5 4.4 Variation of Thermal Stability and Wind Speed as a Function of Diurnal Time

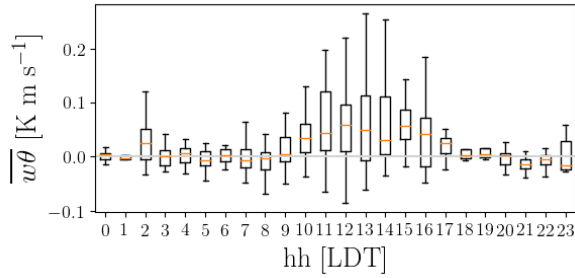
The atmospheric dynamical condition can be described using two parameters: 1) wind speed and 2) thermal stability. The wind speed determines mechanical advection and usually the higher the wind speed the greater is, the greater will be the



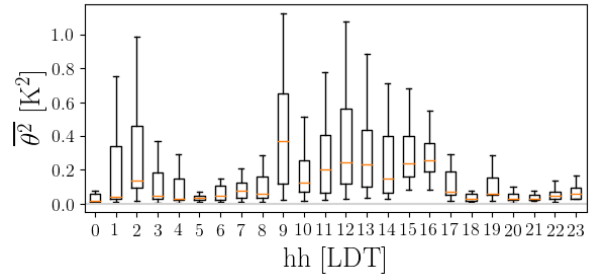
(a) Along-wind vertical momentum flux



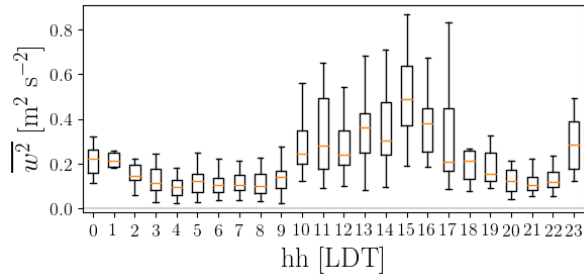
(b) Cross-wind vertical momentum flux



(c) Vertical sensible kinematic heat flux

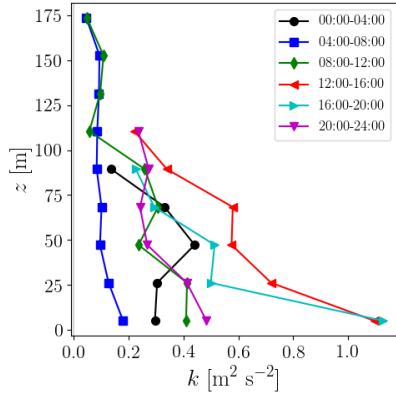


(d) Variance of potential temperature

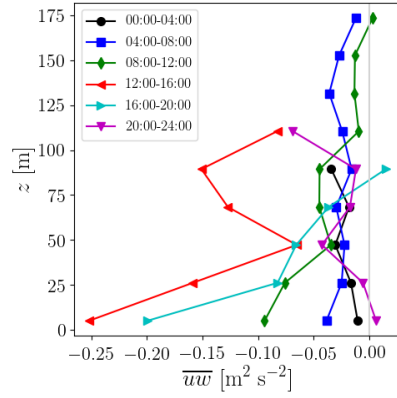


(e) Variance of vertical wind velocity

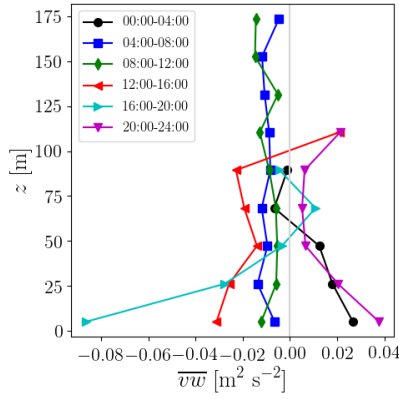
Figure 9. Diurnal variation of different turbulence statistics. At each hour observations are plotted using statistical percentiles (5th, 25th, 50th, 75th, and 95th); Local Daylight Time (LDT).



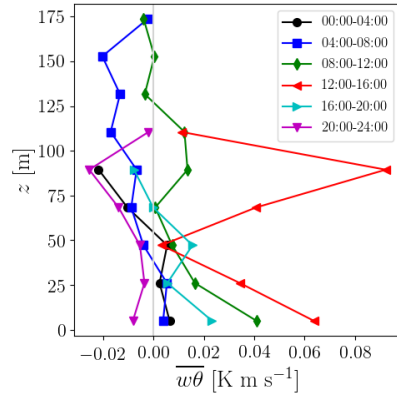
(a) Turbulence kinetic energy



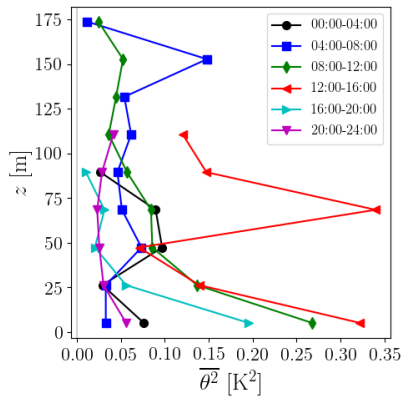
(b) Along-wind vertical momentum flux



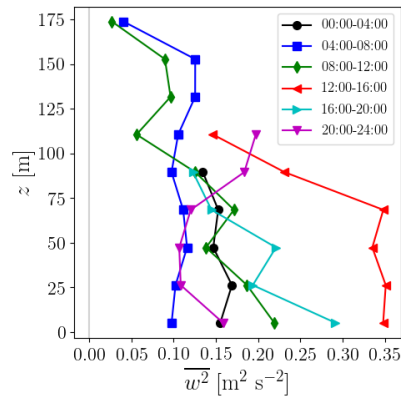
(c) Cross-wind vertical momentum flux



(d) Vertical sensible kinematic heat flux



(e) Variance of potential temperature



(f) Variance of vertical wind velocity

Figure 10. Vertical profiles of different turbulence statistics for different diurnal time periods (4-hr intervals) of the day; times in Local Daylight Time (LDT).

atmospheric transport and diffusion coefficient. Thermal stability determines the buoyant transport in the vertical direction in the atmosphere. Thermal stability is reported using various methods such as i) the vertical gradients of the potential temperature (Liu and Liang, 2010), ii) the bulk Richardson number (Mahrt, 1981; Aliabadi et al., 2016a), or iii) Monin-Obukhov length (Obukhov, 1971; Wilson, 2008).

If vertical gradients of the potential temperature or the bulk Richardson number are positive, the atmosphere is stable and the buoyant transport is suppressed. This occurs during the nights and early mornings. If the vertical gradients of the potential temperature and bulk Richardson number are negative, the atmosphere is unstable and buoyant transport is enhanced. This occurs during the mid afternoons. If the vertical gradients of potential temperature and bulk Richardson number are close to zero, the atmosphere is neutral, in which case buoyant transport is still present but weak.

Figures 11 and 12 show evidence for the variation of vertical profiles of ~~thermal stability~~ potential temperature and wind speed as a function of diurnal time, respectively. Here the data is statistically processed in 3-min intervals, such that a median is calculated for each 3-min interval. Since observations for these plots are not aggregated over many days, the height interval is not binned. The thermal stability and magnitude of wind speed differences between day and night are clearly evident. However, the profiles of wind speed do not exhibit the expected power law or logarithmic law as a function of height. This is likely due to limited time of sampling.

4.5 Atmospheric Dynamical Condition

As shown in Fig. 13, all observations were used to determine the atmospheric dynamical condition on a two-dimensional map consisting of thermal stability, i.e. bulk Richardson number Ri_b , and mean wind speed \bar{S} . Here the bulk Richardson number is defined as

$$Ri_b = \frac{gH}{(\bar{S}_H - \bar{S}_S)^2} \frac{\bar{\Theta}_H - \bar{\Theta}_S}{\bar{\Theta}_A}, \quad (8)$$

where g is gravitational acceleration, H is the maximum altitude for each launch, \bar{S}_H is mean horizontal wind speed at maximum altitude, \bar{S}_S is mean horizontal wind speed near the surface, $\bar{\Theta}_H$ is mean potential temperature at maximum altitude, $\bar{\Theta}_S$ is mean potential temperature near the surface, and $\bar{\Theta}_A$ is mean potential temperature for the entire launch.

The frequency plot shows the most frequent status of the atmosphere by providing a normalized count of each pair of observed Ri_b and \bar{S} , while the colour plot shows the median value for turbulence kinetic energy k given as a function of each pair of observed Ri_b and \bar{S} . It is found that the atmosphere spends a considerable amount of time under near-neutral and stable condition at nights and early mornings where $Ri_b \geq 0$, possibly with the same likelihood of unstable state during ~~mid day~~ midday where $Ri_b < 0$. The colour plot for turbulence kinetic energy shows that the highest values are observed under near-neutral conditions where $Ri_b \sim 0$ and mean wind speed is high such that $\bar{S} > 5 \text{ m s}^{-1}$. A few spurious high frequency of observations are detected for very large Richardson numbers $Ri_b \sim 10$ and very low wind speeds $\bar{S} \sim 1 - 2 \text{ m s}^{-1}$. These are likely due to the inability of TANAB to detect mean wind speed gradients under calm conditions. These plots demonstrate that

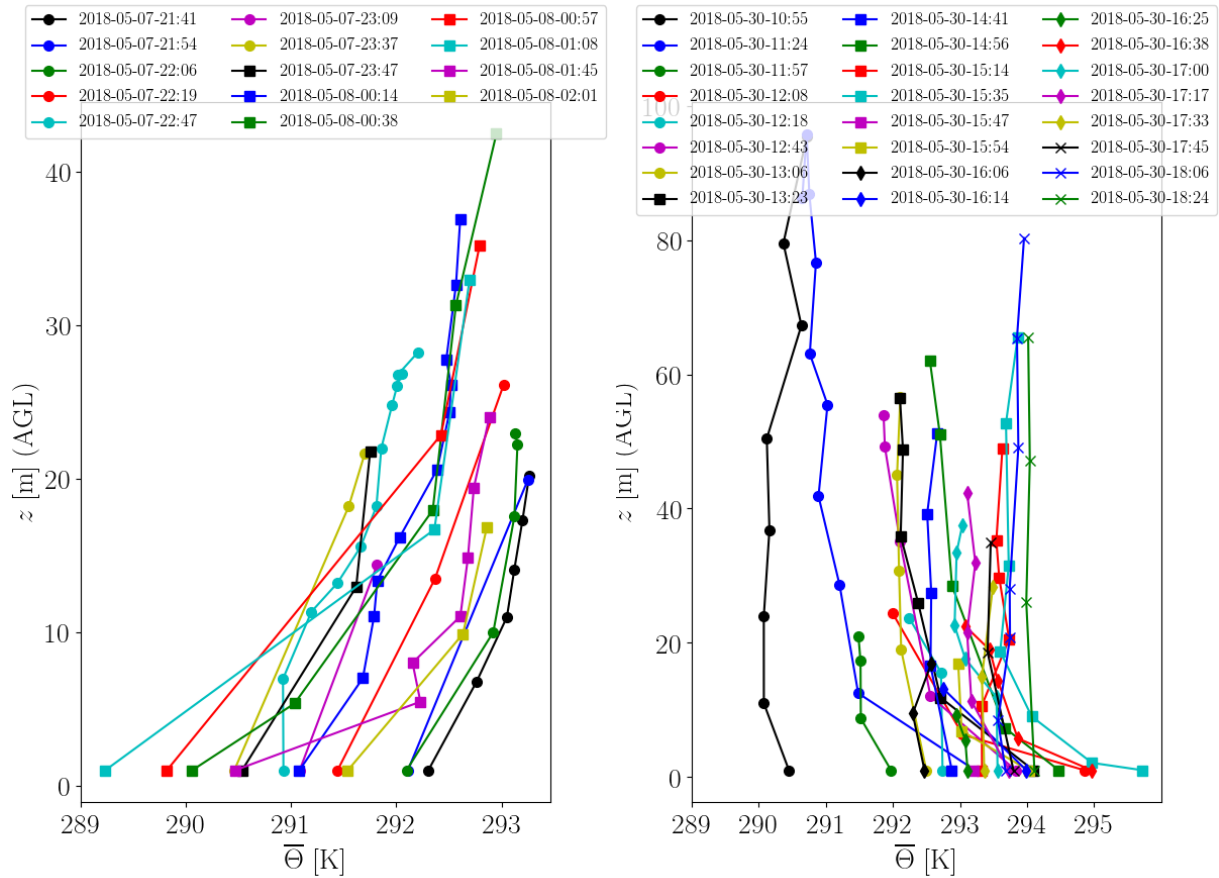


Figure 11. Vertical profiles of potential temperature on 7 May 2018 and 30 May 2018; Left: thermally stable condition at night and early morning when the gradients are positive near the surface; Right: thermally unstable condition at mid day when the gradients are negative near the surface. [Times are in Local Daylight Time \(LDT\).](#)

10 the atmosphere in the surface layer has *preferred* states. For instance, it was never observed to be very stable and gusty at the same time.

4.6 Comparison Between the Mine and the Tailings Pond

Almost the same number of hours were ~~spend~~spent measuring the surface layer at the mine and near the tailings pond using TANAB. The measurements attempted to cover a 24-hr time period in three to four days so that ~~it~~TANAB would capture the diurnal variations completely. Note that due to logistical difficulties, it was impossible to measure the surface layer in either
 15 ~~center~~centre of the mine, while the base location near the pond was on the east side. We have compared the diurnal variations

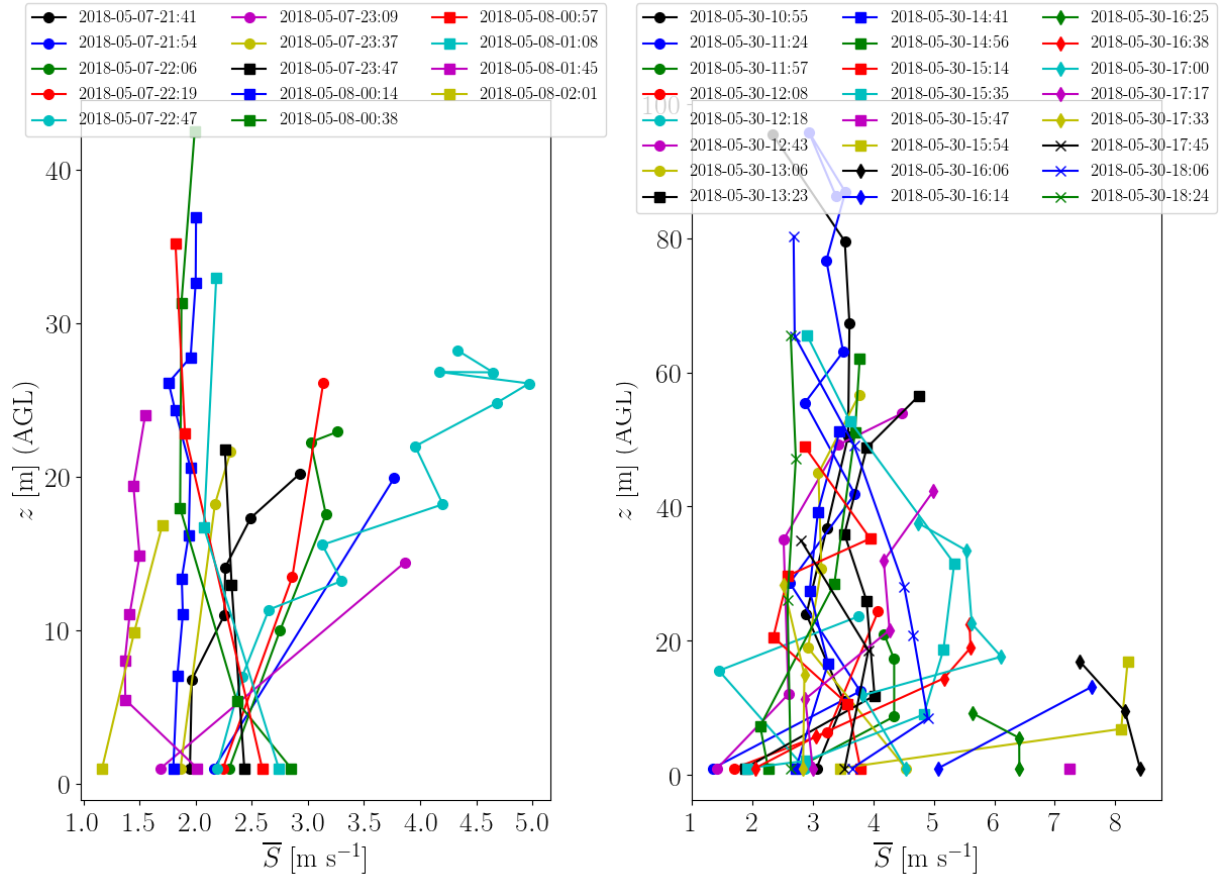


Figure 12. Vertical profiles of wind speed on 7 May 2018 and 30 May 2018. Left: thermally stable condition at night and early morning, Right: thermally unstable condition at midday. [Times are in Local Daylight Time \(LDT\).](#)

in various surface layer properties between the mine and near the pond observations. These include the mean horizontal wind speed, turbulence kinetic energy, vertical momentum flux, vertical sensible kinematic heat flux, variance of vertical velocity vector, and variance of potential temperature. We have also compared the atmospheric dynamical condition in terms of the bulk Richardson number and mean wind speed. The idea behind this comparison was to quantify any differences in surface layer

5 properties as a result of terrain complexity and land use.

4.6.1 Comparison of Diurnal Variation of Turbulence Properties

TANAB captured the diurnal variation of mean and turbulence statistics in the mine as well as near the tailings pond. In [Fig. Figs. 14 and 15](#) we plot the diurnal variations for the mine in red and near the tailings pond in blue. It is observed that, for both in the mine and near the tailings pond, all the turbulence parameters exhibit a significant diurnal variation, indicating

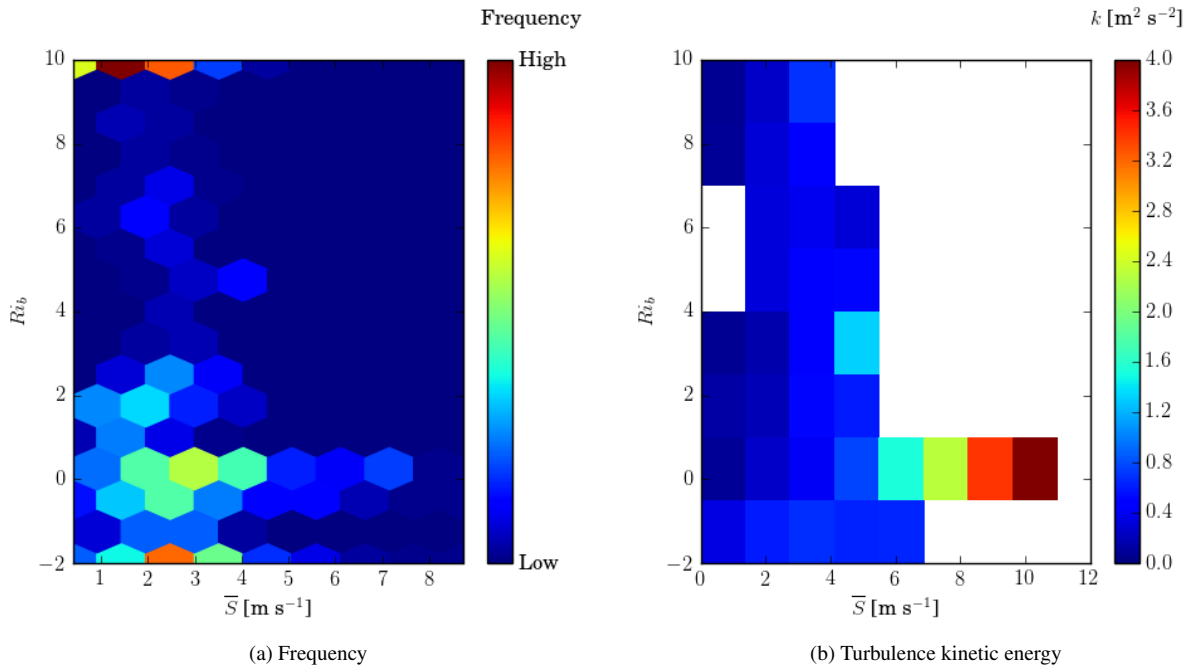


Figure 13. Left: frequency a) Frequency plot of atmospheric dynamical condition as a function of bulk Richardson number Ri_b and mean wind speed \bar{S} ; Right: b) turbulence kinetic energy k as a function of the same parameters.

10 calm conditions at nights and early mornings, when atmospheric diffusion coefficient is low, and gusty conditions in the mid afternoons when the atmospheric diffusion coefficient is high. The data is aggregated for all altitudes.

There are subtle differences between observations at the mine and near the tailings pond. The trends in mean wind speed \bar{S} and turbulence kinetic energy k suggest that the mine experiences calm conditions at early morning hours, i.e. from 0500 to 0700 LDT, when the atmospheric stability is at its maximum, while at the same time near the pond, higher mean wind speeds and turbulence kinetic energy are observed. During early afternoons and under unstable conditions, i.e. from 1500 to 1700 LDT, near the pond higher mean wind speeds, lower mean wind speed and turbulence kinetic energy are observed in comparison to the mine. Even though day to day variations of meteorological conditions may contribute to this, there is evidence that such features can also result from terrain complexity and land surface heterogeneity. As far as the vertical sensible kinematic heat flux $\overline{w\theta}$ and variance of potential temperature $\overline{\theta^2}$ are concerned, the mine shows significantly higher activities compared to the location near the pond. In fact, the mine shows significantly positive vertical heat flux and substantial potential temperature variance from 0200 to 0300 LDT. It is known that excavation activities using heavy machinery is very active in the mine over night, possibly explaining the significance of heat flux and potential temperature variance.

5

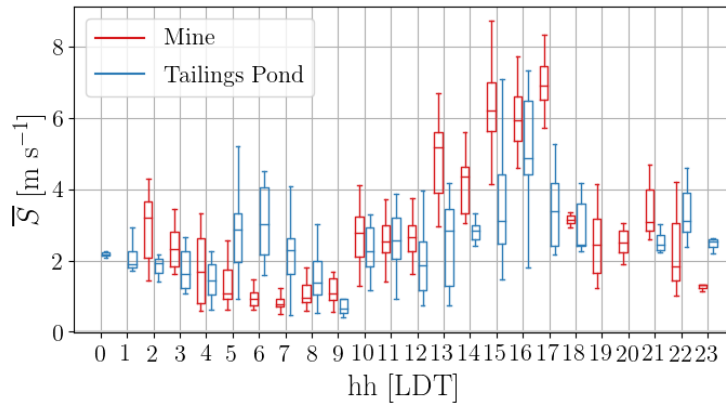


Figure 14. [Diurnal variation of mean wind speed. At each hour observations are plotted using statistical percentiles \(5th, 25th, 50th, 75th, and 95th\); Local Daylight Time \(LDT\).](#)

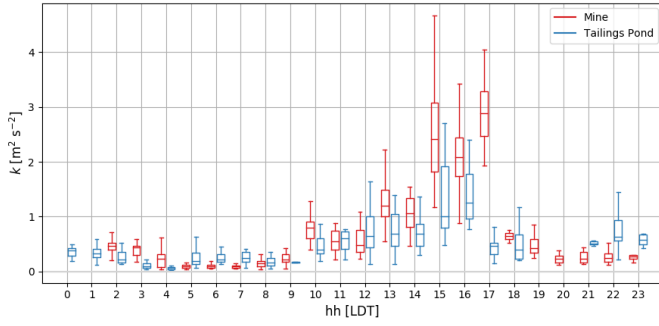
10 4.6.2 Comparison of Atmospheric Dynamical Condition

Figure 16 shows the frequency plots of atmospheric dynamical condition as a function of the bulk Richardson number Ri_b and mean wind speed \bar{S} in the mine and near the tailings pond separately. It was found that in the case of tailings pond, the atmosphere spends a considerable amount of time under near-neutral and unstable conditions in comparison to the mine. Again, the frequency plots should be read with care at $Ri_b \sim 10$ due to the lack of a reliable TANAB predictions for vertical mean wind speed gradients under calm conditions.

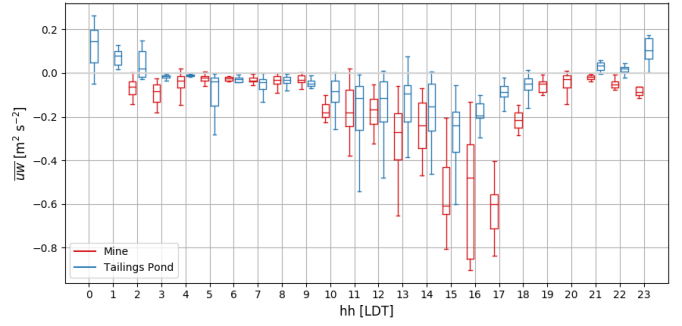
4.7 Earth Surface Thermal Imaging

An important measurement of the TANAB system was the earth surface thermal imaging. The surface temperature values and thermal gradients at the mining site are important physical parameters that can potentially drive unique airflow patterns. For instance, hot spots can create rising thermal structures in the boundary layer that subsequently carry surface-level atmospheric constituents, such as GHGs, upward. On the other hand, cold spots can create stable boundary layers and initiate subsiding flow that prevent mixing of gaseous compounds within the boundary layer. Inevitably, the thermal condition places a significant impact on the gaseous emission fluxes. TANAB took more than 10,000 thermal images during the May 2018 campaign, all of which are processed in detail to determine the surface temperature characteristics of the site during different diurnal times and at different locations. An analysis of selected thermal images is included below.

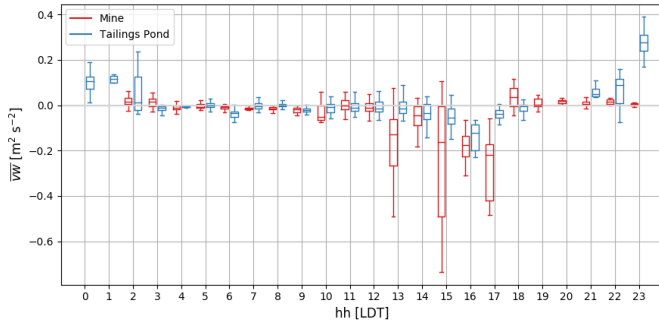
Figure 17 shows the median temperature maps for the site for different diurnal periods (4-hr intervals) of the day. Data is aggregated over all observations measured by the experiments as mentioned in Table 3. The diurnal variation of the temperature is evident. The surface temperature is the greatest during mid day time interval 1200 – 1600 LDT, while the magnitudes are smallest during night time and early morning time interval 0400 – 0800 LDT.



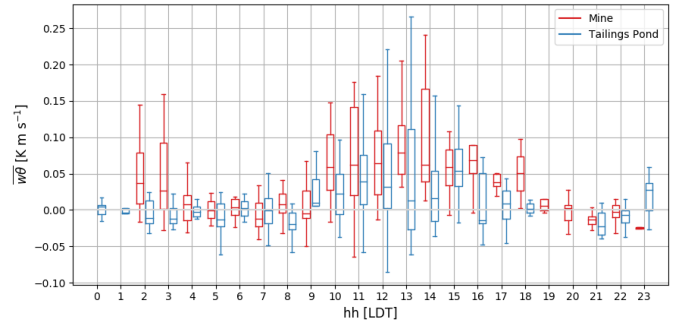
(a) Diurnal variation of turbulence kinetic energy



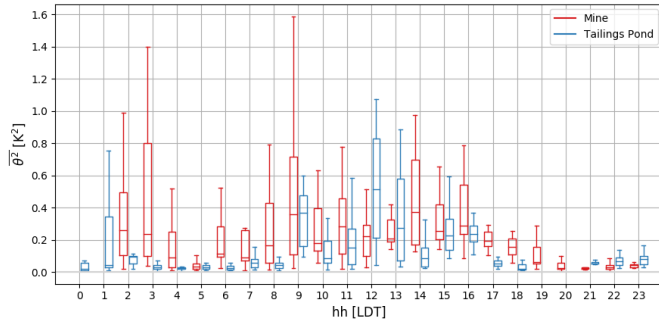
(b) Along-wind vertical momentum flux



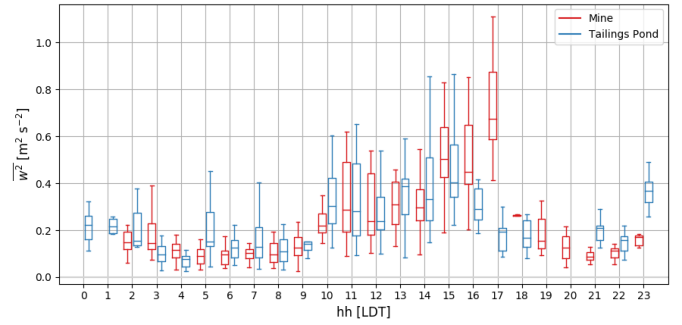
(c) Cross-wind vertical momentum flux



(d) Vertical sensible kinematic heat flux



(e) Variance of potential temperature



(f) Variance of vertical wind velocity

Figure 15. Diurnal variation of different mean and turbulence statistics; at each hour observations are plotted using statistical percentiles (5th, 25th, 50th, 75th, and 95th); Local Daylight Time (LDT).

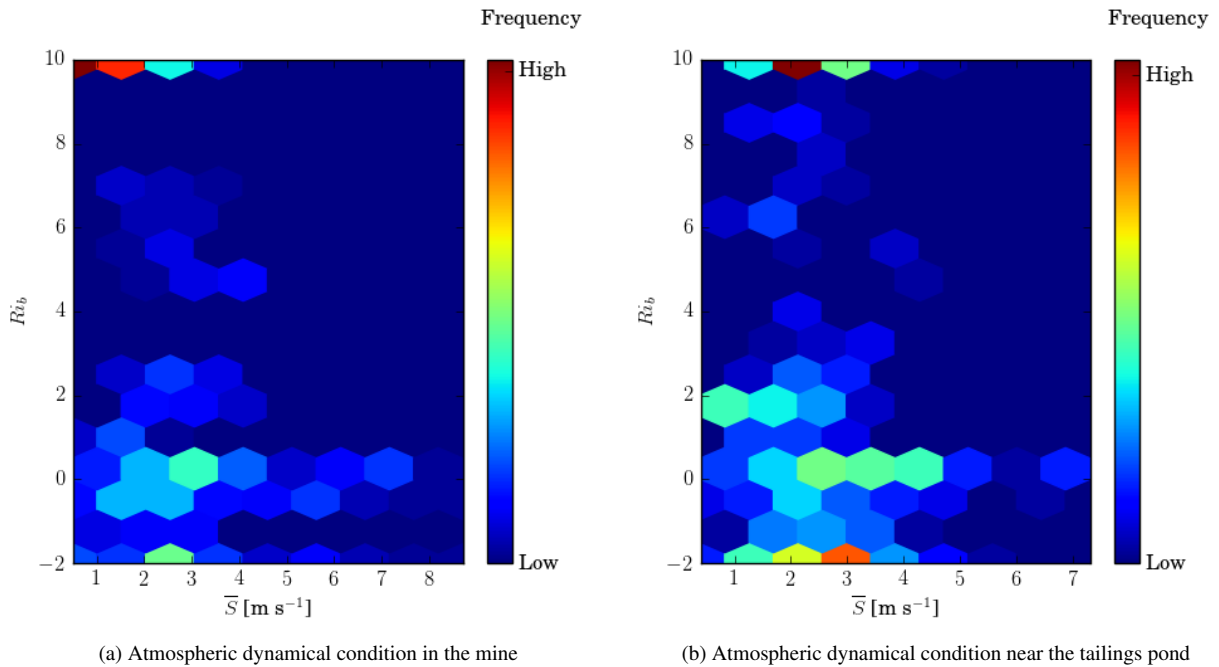


Figure 16. Frequency plots of atmospheric dynamical condition as a function of bulk Richardson number Ri_b and mean wind speed \bar{S} in the mine (left) and near the tailings pond (right).

In order to quantify the difference in temperatures as a consequence of terrain heterogeneity and other complexities between the mine and tailings pond, we have compared the surface temperatures using box plots in Fig. 18 at different diurnal periods (4-hr intervals) aggregated over the entire observation period as detailed in Table 3. The thermal imaging data is in agreement with the TriSonicaTM Mini data as plotted in Fig. 15. For many periods the mine shows higher activity in heat related turbulence statistics such as the turbulent kinematic vertical heat flux during 0800–2000 LDT and variance of potential temperature during 0000–0400 LDT. These time intervals correspond to periods when the mine shows a statistically significant higher surface temperature than the pond using the box plots.

The median temperatures measured by TANAB are compared with satellite measurements of MODIS on 24 May 2018. For this comparison, the selected images for TANAB were captured during 1211–1401 LDT, and for MODIS the selected data source corresponded to 1230 LDT. The horizontal resolution for this comparison was 1 km × 1 km. The comparison and the calculated percentage relative error are shown in Fig. 19. The percentage relative error is less than 6.3.9% everywhere within the perimeter of the mining facility and the median relative error within the mining facility is 1.10.9%. However, the LST errors are higher in areas between the mine and the northwest direction and lower in the southeast direction. These directions are along the topographical height variation, which is highest in the northwest and lowest in the southeast pond. It appears that TANAB temperature predictions in the northwest direction this region result from more oblique-angle observations, which are

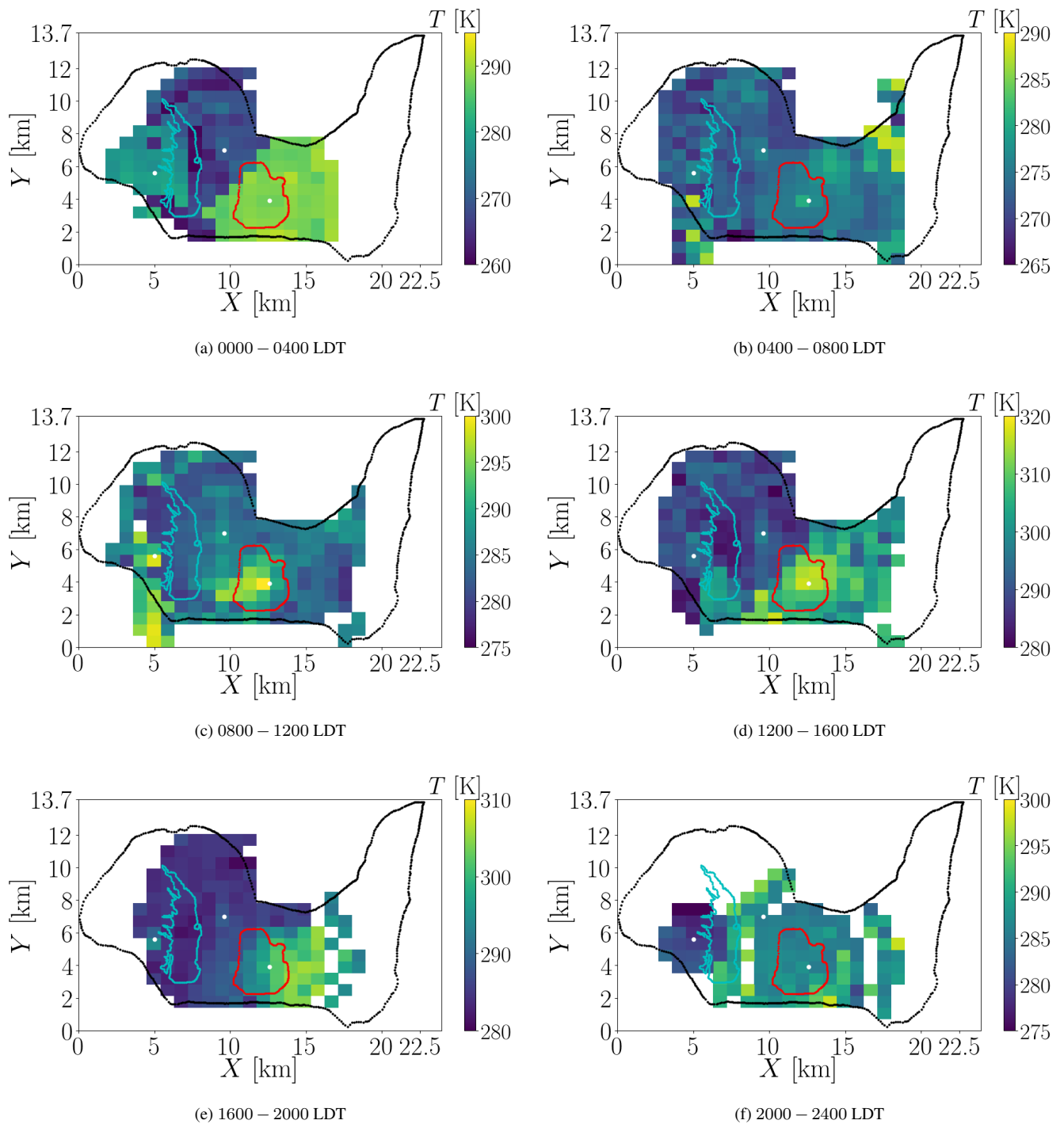


Figure 17. Median temperature maps for the site at different periods (4-hr intervals) of the day; median temperature temperatures calculated for tiles at a resolution of $1 \text{ km} \times 1 \text{ km}$; times are in Local Daylight Time (LDT).

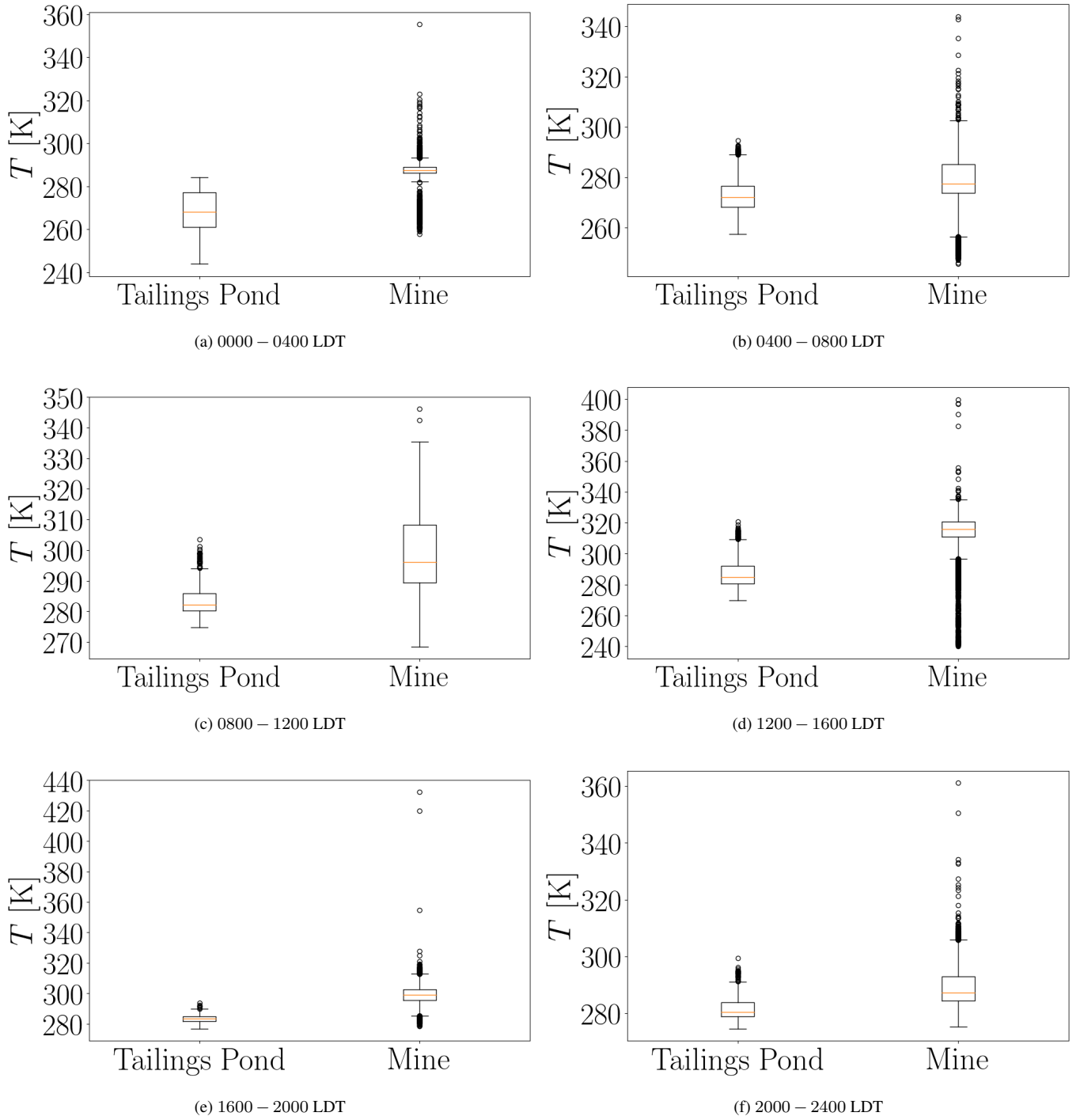


Figure 18. Boxplot-Box plot of temperatures for tailings pond and mine for different periods (4-hr intervals) of the day; times are in Local Daylight Time (LDT).

prone to a higher error. It should be noted that the land elevation in this region changes drastically from the mine to the pond such that images recorded during the mine launches did not capture LST at the top of this region accurately.

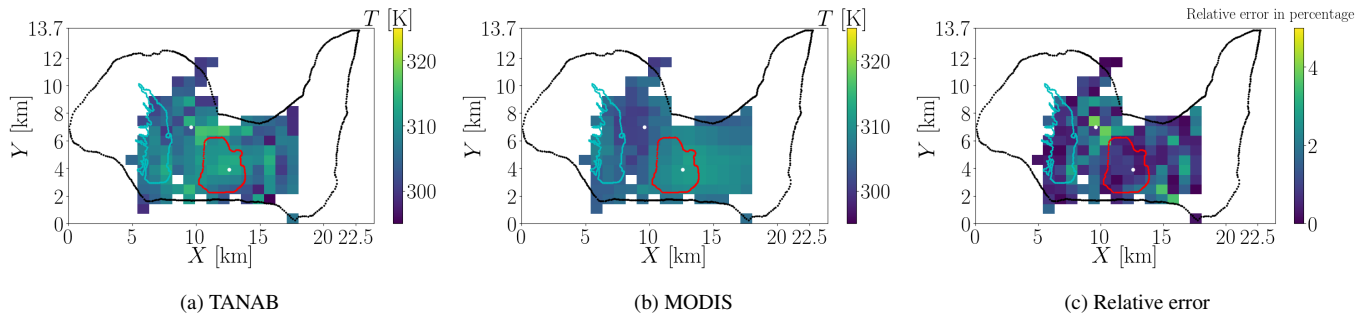


Figure 19. Comparison of median temperatures measured by TANAB and MODIS observations in the early afternoon on 24 May 2018; TANAB and MODIS temperatures calculated for tiles at a resolution of $1 \text{ km} \times 1 \text{ km}$.

As shown by this surface temperature analysis, TANAB offers many advantages over existing satellite systems that attempt to observe the earth surface temperatures. On the one hand, geostationary satellites, such as the GOES-R, exhibit ~~very~~-low horizontal resolutions ($\sim 1 - 2 \text{ km}$) and high temporal resolutions (15 minutes) at such high altitudes (Cintineo et al., 2016; Schmit et al., 2017). On the other hand, orbiting satellites capable of thermal imaging at high horizontal resolutions ($\sim 10 - 100 \text{ m}$), such as the LANDSAT group of satellites, pass over northern sites very intermittently once every ~~sixteen days~~-16 days (Weng, 2012; Chastain et al., 2019). The TANAB overcomes these difficulties by allowing frequent observations at high horizontal resolutions.

20 5 Conclusions and Future Work

The vertical structure of the Atmospheric Boundary Layer (ABL) in an orographically complex terrain, such as a mine, can be complicated. The Tethered And Navigated Air blimp (TANAB) has provided an acceptable platform for the meteorological measurements inside the surface layer within ABL and atmospheric dynamical condition over a complex terrain of a mining facility. The field campaign occurred in May 2018 in northern Canada. In the surface layer, most atmospheric transport mechanisms are highly influenced by the terrain ~~geometry~~complexity. TANAB measured the microclimate in the complex terrain by quantifying mean and turbulence statistics of the atmospheric meteorology. This was achieved by sensing wind speed, wind direction, temperature, relative humidity, and pressure. The calculated parameters included mean horizontal wind speed, turbulence kinetic energy, vertical momentum flux, vertical sensible kinematic heat flux, variance of potential temperature, and variance of vertical wind velocity. In addition, TANAB performed earth surface thermal imaging (temperature mapping) to further characterize how the surface layer interacted with surface temperatures. TANAB further determined the atmospheric dynamical condition by specifying the combination of the thermal stability state (bulk Richardson number) and mean horizontal wind speed.

TANAB observed that both wind speed and turbulence kinetic energy exhibit a significant diurnal variation, indicating calm conditions at nights and early mornings, when atmospheric diffusion coefficient is low, and gusty conditions in the mid afternoons, when the atmospheric diffusion coefficient is high. TANAB also revealed the vertical structure of the atmosphere near the surface for most meteorological parameters. The highest turbulence kinetic energies occurred in the lowest 100 m above the surface, albeit for small fluctuation time and length scales probed. Experiments provided evidence for the variation of thermal stability and wind speed as a function of diurnal time. The atmosphere spent a considerable amount of time under near-neutral and stable conditions, with implications on atmospheric diffusion coefficient and emission fluxes of atmospheric constituents released near the surface. The experiments specifically observed differences in the microclimate in the mine pit in comparison to near the tailings pond. The overall pattern of diurnal variation was found to be similar for both the mine and the tailings pond, but subtle meteorological differences were observed. The mean wind speed and turbulence kinetic energy were comparatively lower in the mine than near the tailings pond in early morning hours, suggesting that the mine boundary layer may have been isolated from the boundary layer above grade. In addition, significantly positive potential temperature variance and turbulent heat fluxes were observed in the mine in various diurnal time windows in comparison to the area near the pond. This was likely due to terrain complexity and anthropogenic activities in the mine. TANAB detected a significant horizontal temperature difference between the mine and ~~surrounding surroundings~~ in comparison to the tailings pond. The mine exhibited greater surface temperatures in many diurnal time periods, likely due to land surface modifications and anthropogenic activities. Higher surface temperatures at the mine could explain the meteorological effects observed in the surface layer of the mine.

A particular challenge in operating the TANAB system is the proper choice of sampling time. On the one hand, short sampling times impose inherent errors in mean and turbulence statistics predictions while enable high resolution vertical measurements. On the other hand, long sampling times impose less inherent errors in mean and turbulence statistics predictions but they only enable low vertical resolution measurements. Another drawback of TANAB system is that it is not autonomous, so it requires intensive operator effort to fly it. Future development requires advanced techniques for autonomous control of TANAB.

Overall, TANAB offers a simple and cost-effective platform for microclimate measurements within the atmospheric surface layer. The light high-frequency weather sensor onboard enables measurement of mean and turbulence statistics of the atmospheric transport. This configuration allows a wide spatiotemporal coverage compared to fixed flux towers. The thermal imaging system enables high resolution temperature mapping of remote environments frequently, thus overcoming current limitations of satellite systems. TANAB can potentially provide meteorological data as boundary conditions or validation datasets for developing high resolution ~~Computational Fluid Dynamics (CFD)~~ computational fluid dynamics and other mesoscale models that attempt simulating meteorological processes and emission fluxes from large complex terrains of mining and other similar facilities.

Code and data availability. The supporting environmental field monitoring data can be requested from the Principal Investigator, Amir A. Aliabadi, at the Atmospheric Innovations Research (AIR) Laboratory at the University of Guelph (<http://aaa-scientists.com/>, aliabadi@uoguelph.ca), via the authorization of data owners.

5 *Author contributions.* The field experimental data was collected by MKN, AN, RB, MRN, and AAA. The analysis of anemometer data was performed by MKN and AAA. The analysis of thermal imaging was performed by RB. Anemometer calibration was performed by AN, MM, and AAA. The funding was acquired by AAA. Supervision of the study was performed by AAA. The manuscript was written and edited by MKN, RB, and AAA with feedback and review by all co-authors.

Competing interests. The authors declare that they have no conflict of interest.

10 *Acknowledgements.* The authors would like to thank Denis Clement, Jason Dorssers, Katharine McNair, James Stock, Darian Vyriotes, Amanda Pinto, and Phillip Labarge for their contribution in the design of the gondola and thermal camera implementation and analysis. Assistance of Joanne Ryks and Ryan Smith in trial testing of TANAB is appreciated. Useful discussions with John Wilson and Thomas Flesch at the University of Alberta are acknowledged. Useful discussions with Françoise Robe at RWDI are acknowledged. Field support from Michelle Seguin (RWDI), Andrew Bellavie (RWDI), and James Ravenhill at Southern Alberta Institute of Technology (SAIT) is appreciated. Field assistance from Nick Veriotes ~~and Mohsen Moradi~~ is appreciated. The authors are indebted to Steve Nyman, Chris Duiker,
15 Peter Purvis, Manuela Racki, Jeffrey Defoe, Joanne Ryks, Ryan Smith, James Bracken, and Samantha French at the University of Guelph, who helped with the campaign logistics. Special credit is directed toward Amanda Sawlor, Esra Mohamed, Di Cheng, Randy Regan, Margaret Love, Angela Vuk, and Carolyn Dowling-Osborn at the University of Guelph for administrative support. The computational platforms were set up with the assistance of Jeff Madge, Joel Best, and Matthew Kent at the University of Guelph. In-kind technical support for this work was provided by Rowan Williams Davies and Irwin Inc. (RWDI).

20 This work was supported by the Discovery Grant program (401231) from the Natural Sciences and Engineering Research Council (NSERC) of Canada; Government of Ontario through the Ontario Centres of Excellence (OCE) under the Alberta-Ontario Innovation Program (AOIP) (053450); and Emission Reduction Alberta (ERA) (053498). OCE is a member of the Ontario Network of Entrepreneurs (ONE).

References

- 25 Alderfasi, A. A. and Nielsen, D. C.: Use of crop water stress index for monitoring water status and scheduling irrigation in wheat, *Agr. Water Manage.*, 47, 69–75, 2001.
- Aliabadi, A. A.: Theory and applications of turbulence: A fundamental approach for scientists and engineers, Amir Abbas Aliabadi Publications, 2018.
- Aliabadi, A. A., Staebler, R. M., de Grandpré, J., Zadra, A., and Vaillancourt, P. A.: Comparison of estimated atmospheric boundary layer mixing height in the Arctic and southern Great Plains under statically stable conditions: experimental and numerical aspects, *Atmos.-Ocean*, 54, 60–74, <https://doi.org/10.1080/07055900.2015.1119100>, 2016a.
- Aliabadi, A. A., Staebler, R. M., Liu, M., and Herber, A.: Characterization and parametrization of Reynolds stress and turbulent heat flux in the stably-stratified lower Arctic troposphere using aircraft measurements, *Bound.-Lay. Meteorol.*, 161, 99–126, <https://doi.org/10.1007/s10546-016-0164-7>, 2016b.
- 5 Aliabadi, A. A., Thomas, J. L., Herber, A. B., Staebler, R. M., Leaitch, W. R., Schulz, H., Law, K. S., Marelle, L., Burkart, J., Willis, M. D., Bozem, H., Hoor, P. M., Köllner, F., Schneider, J., Lévassieur, M., and Abbatt, J. P. D.: Ship emissions measurement in the Arctic by plume intercepts of the Canadian Coast Guard icebreaker *Amundsen* from the *Polar 6* aircraft platform, *Atmos. Chem. Phys.*, 16, 7899–7916, <https://doi.org/10.5194/acp-16-7899-2016>, 2016c.
- Aliabadi, A. A., Krayenhoff, E. S., Nazarian, N., Chew, L. W., Armstrong, P. R., Afshari, A., and Norford, L. K.: Effects of roof-edge roughness on air temperature and pollutant concentration in urban canyons, *Bound.-Lay. Meteorol.*, 164, 249–279, <https://doi.org/10.1007/s10546-017-0246-1>, 2017.
- 10 Aliabadi, A. A., Moradi, M., Clement, D., Lubitz, W. D., and Gharabaghi, B.: Flow and temperature dynamics in an urban canyon under a comprehensive set of wind directions, wind speeds, and thermal stability conditions, *Environ. Fluid Mech.*, 19, 81–109, <https://doi.org/10.1007/s10652-018-9606-8>, 2018a.
- 15 Aliabadi, A. A., Veriotes, N., and Pedro, G.: A Very Large-Eddy Simulation (VLES) model for the investigation of the neutral atmospheric boundary layer, *J. Wind Eng. Ind. Aerod.*, 183, 152–171, 2018b.
- Arroyo, R. C., Rodrigo, J. S., and Gankarski, P.: Modelling of atmospheric boundary-layer flow in complex terrain with different forest parameterizations, *Journal of Physics: Conference Series*, 524, 012 119, <https://doi.org/http://stacks.iop.org/1742-6596/524/i=1/a=012119>, 2014.
- 20 Aubry-Wake, C., Baraer, M., McKenzie, M., J., Mark, B. G., Wigmore, O., Hellström, R. A., Lautz, L., and Somers, L.: Measuring glacier surface temperatures with ground-based thermal infrared imaging, *Geophys. Res. Lett.*, 42, 8489–8497, 2015.
- Baker, E. A., Lautz, L. K., McKenzie, J. M., and Aubry-Wake, C.: Improving the accuracy of time-lapse thermal infrared imaging for hydrologic applications, *J. Hydrol.*, 571, 60–70, 2019.

- Berman, E. A.: Measurements of temperature and downwind spectra in the “Buoyant Subrange”, *J. Atmos. Sci.*, 33, 495–498, [https://doi.org/10.1175/1520-0469\(1976\)033<0495:MOTADS>2.0.CO;2](https://doi.org/10.1175/1520-0469(1976)033<0495:MOTADS>2.0.CO;2), 1976.
- 25 Bláha, M., Eisenbeiss, H., Grimm, D., and Limpach, P.: Direct georeferencing of UAVs, in: *Int. Arch. Photogramm. Remote Sens. Spatial Inf. Sci.*, XXXCVIII-1/C22, pp. 131–136, 2011.
- Bolanakis, D. E., Kotsis, K. T., and Laopoulos, T.: Temperature influence on differential barometric altitude measurements, in: 2015 IEEE 8th International Conference on Intelligent Data Acquisition and Advanced Computing Systems: Technology and Applications (IDAACS), vol. 1, pp. 120–124, <https://doi.org/10.1109/IDAACS.2015.7340711>, 2015.
- 30 Bowden, R. D., Castro, M. S., Melillo, J. M., Steudler, P. A., and Aber, J. D.: Fluxes of greenhouse gases between soils and the atmosphere in a temperate forest following a simulated hurricane blowdown, *Biogeochemistry*, 21, 61–71, <https://doi.org/10.1007/BF00000871>, 1993.
- Budzier, H. and Gerlach, G.: Calibration of uncooled thermal infrared cameras, *J. Sens. Sens. Syst.*, 4, 187–197, 2015.
- Bueno, B., Norford, L., Hidalgo, J., and Pigeon, G.: The urban weather generator, *J. Build. Perf. Simulat.*, 6, 269–281, <https://doi.org/10.1080/19401493.2012.718797>, 2012.
- 5 Businger, J. A., Wyngaard, J. C., Izumi, Y., and Bradley, E. F.: Flux-profile relationships in the atmospheric surface layer, *J. Atmos. Sci.*, 28, 181–189, [https://doi.org/10.1175/1520-0469\(1971\)028<0181:FPRITA>2.0.CO;2](https://doi.org/10.1175/1520-0469(1971)028<0181:FPRITA>2.0.CO;2), 1971.
- Caldwell, S. H., Kelleher, C., Baker, E. A., and Lautz, L. K.: Relative information from thermal infrared imagery via unoccupied aerial vehicle informs simulations and spatially-distributed assessments of stream temperature, *Sci. Total Environ.*, 661, 364–374, 2019.
- 10 Canut, G., Couvreur, F., Lothon, M., Legain, D., Pigué, B., Lampert, A., Maurel, W., and Moulin, E.: Turbulence fluxes and variances measured with a sonic anemometer mounted on a tethered balloon, *Atmos. Meas. Tech.*, 9, 4375–4386, <https://doi.org/10.5194/amt-9-4375-2016>, 2016.
- Cao, F., Liu, F., Guo, H., Kong, W., Zhang, C., and He, Y.: Fast detection of *Sclerotinia Sclerotiorum* on oilseed rape leaves using low-altitude remote sensing technology, *Sensors-Basel*, 18, 4464, 2018.
- 15 Casten, T., Mousset-Jones, P., and Calizaya, F.: Ultrasonic anemometry in underground excavations, In A.M. Wala (Ed.), *Proc. 7th US Mine Ventilation Symposium*, Cushing-Malloy Inc., 1995.
- Chastain, R., Housman, I., Goldstein, J., Finco, M., and Tenneson, K.: Empirical cross sensor comparison of Sentinel-2A and 2B MSI, Landsat-8 OLI, and Landsat-7 ETM+ top of atmosphere spectral characteristics over the conterminous United States, *Remote Sens. Environ.*, 221, 274–285, 2019.
- 20 Chiabrando, F., Lingua, A., and Piras, M.: Direct photogrammetry using UAV: tests and first results, in: *Int. Arch. Photogramm. Remote Sens. Spatial Inf. Sci.*, XL-1/W2, pp. 81–86, 2013.
- Cintineo, R. M., Otkin, J. A., Jones, T. A., Koch, S., and Stensrud, D. J.: Assimilation of synthetic GOES-R ABI infrared brightness temperatures and WSR-88D radar observations in a high-resolution OSSE, *Mon. Weather Rev.*, 144, 3159–3180, 2016.

- Crosson, W. L., Al-Hamdan, M. Z., Hemmings, S. N., and Wade, G. M.: A daily merged MODIS Aqua-Terra land surface temperature data set for the conterminous United States, *Remote Sens. Environ.*, 119, 315–324, 2012.
- Davidson, B.: The Barbados oceanographic and meteorological experiment, *B. Am. Meteorol. Soc.*, 49, 928–935, <https://doi.org/10.1175/1520-0477-49.9.928>, 1968.
- Egerer, U., Gottschalk, M., Siebert, H., Ehrlich, A., and Wendisch, M.: The new BELUGA setup for collocated turbulence and radiation measurements using a tethered balloon: first applications in the cloudy Arctic boundary layer, *Atmos. Meas. Tech.*, 12, 4019–4038, <https://doi.org/10.5194/amt-12-4019-2019>, 2019.
- Eynard, D., Vasseur, P., Demonceaux, C., and Frémont, V.: Real time UAV altitude, attitude and motion estimation from hybrid stereovision, *Auton. Robot.*, 33, 157–172, 2012.
- Fernando, H. J. S. and Weil, J. C.: Whither the stable boundary layer?: A shift in the research agenda, *B. Am. Meteorol. Soc.*, 91, 1475–1484, <https://doi.org/10.1175/2010BAMS2770.1>, 2010.
- FLIR-Systems: Installation manual: A3XX series FLIR and A6XX series, FLIR Systems, 2010.
- FLIR-Systems: The ultimate infrared handbook for R&D professionals, FLIR Systems, 2012.
- Friedman, H. A. and Callahan, W. S.: The ESSA research flight facility’s support of environmental research in 1969, *Weatherwise*, 23, 174–185, <https://doi.org/10.1080/00431672.1970.9932889>, 1970.
- Gallardo-Saavedra, S., Hernández-Callejo, L., and Oscar, D.-P.: Technological review of the instrumentation used in aerial thermographic inspection of photovoltaic plants, *Renew. Sust. Energ. Rev.*, 93, 566–579, 2018.
- Garstang, M. and La Seur, N. E.: the 1968 Barbados Experiment, *B. Am. Meteorol. Soc.*, 49, 627–635, <https://doi.org/10.1175/1520-0477-49.6.627>, 1968.
- Haugen, D. A., Kaimal, J. C., Readings, C. J., and Rayment, R.: A Comparison of balloon-borne and tower-mounted instrumentation for probing the atmospheric boundary layer, *J. Appl. Meteorol.*, 14, 540–545, [https://doi.org/10.1175/1520-0450\(1975\)014<0540:ACOBBA>2.0.CO;2](https://doi.org/10.1175/1520-0450(1975)014<0540:ACOBBA>2.0.CO;2), 1975.
- Holnicki, P. and Nahorski, Z.: Emission data uncertainty in urban air quality modeling—case study, *Environ. Model. Assess.*, 20, 583–597, <https://doi.org/10.1007/s10666-015-9445-7>, 2015.
- Horny, N.: FPA camera standardisation, *Infrared Phys. Techn.*, 44, 109–119, 2003.
- Irons, J. R., Dwyer, J. L., and Barsi, J. A.: The next Landsat satellite: the Landsat data continuity mission, *Remote Sens. Environ.*, 122, 11–21, 2012.
- Kelly, J., Kljun, N., Olsson, P.-O., Mihai, L., Liljeblad, B., Weslien, P., Klemdtsson, L., and Eklundh, L.: Challenges and best practices for deriving temperature data from an uncalibrated UAV thermal camera, *Remote Sens.-Basel*, 11, 567, 2019.

- Krayenhoff, E. S. and Voogt, J. A.: A microscale three-dimensional urban energy balance model for studying surface temperatures, *Bound.-Lay. Meteorol.*, 123, 433–461, <https://doi.org/10.1007/s10546-006-9153-6>, 2007.
- 25 Kumar, A.: Long term (2003–2012) spatio-temporal MODIS (Terra/Aqua level 3) derived climatic variations of aerosol optical depth and cloud properties over a semi arid urban tropical region of Northern India, *Atmos. Environ.*, 83, 291–300, 2014.
- Legain, D., Bousquet, O., Douffet, T., Tzanos, D., Moulin, E., Barrie, J., and Renard, J.-B.: High-frequency boundary layer profiling with reusable radiosondes, *Atmos. Meas. Tech.*, 6, 2195–2205, <https://doi.org/10.5194/amt-6-2195-2013>, 2013.
- 30 Lenschow, D. H., Wyngaard, J. C., and Pennell, W. T.: Mean-field and second-moment budgets in a baroclinic, convective boundary layer, *J. Atmos. Sci.*, 37, 1313–1326, [https://doi.org/10.1175/1520-0469\(1980\)037<1313:MFASMB>2.0.CO;2](https://doi.org/10.1175/1520-0469(1980)037<1313:MFASMB>2.0.CO;2), 1980.
- Lenschow, D. H., Mann, J., and Kristensen, L.: How long is long enough when measuring fluxes and other turbulence statistics?, *J. Atmos. Ocean. Tech.*, 11, 661–673, [https://doi.org/10.1175/1520-0426\(1994\)011<0661:HLILEW>2.0.CO;2](https://doi.org/10.1175/1520-0426(1994)011<0661:HLILEW>2.0.CO;2), 1994.
- Li, Z.-L., Tang, B.-H., Wu, H., Ren, H., Yan, G., Wan, Z., Trigo, I. F., and Sobrino, J. A.: Satellite-derived land surface temperature: Current 5 status and perspectives, *Remote Sens. Environ.*, 131, 14–37, 2013.
- Lin, D., Maas, H.-G., Westfield, P., Budzier, H., and Gerlach, G.: An advanced radiometric calibration approach for uncooled thermal cameras, *Photogramm. Rec.*, 33, 30–48, 2018.
- Liu, L., Li, C., Lei, Y., Yin, J., and Zhao, J.: Volcanic ash cloud detection from MODIS image based on CPIWS method, *Acta Geophys.*, 65, 151–163, 2017.
- 10 Liu, S. and Liang, X.-Z.: Observed diurnal cycle climatology of planetary boundary layer height, *J. Climate*, 21, <https://doi.org/10.1175/2010JCLI3552.1>, 2010.
- Lothon, M., Lohou, F., Pino, D., Couvreux, F., Pardyjak, E. R., Reuder, J., Vilà-Guerau de Arellano, J., Durand, P., Hartogensis, O., Legain, D., Augustin, P., Gioli, B., Lenschow, D. H., Faloona, I., Yagüe, C., Alexander, D. C., Angevine, W. M., Bargain, E., Barrié, J., Bazile, E., Bezombes, Y., Blay-Carreras, E., van de Boer, A., Boichard, J. L., Bourdon, A., Butet, A., Campistron, B., de Coster, O., Cuxart, J., 15 Dabas, A., Darbieu, C., Deboudt, K., Delbarre, H., Derrien, S., Flament, P., Fourmentin, M., Garai, A., Gibert, F., Graf, A., Groebner, J., Guichard, F., Jiménez, M. A., Jonassen, M., van den Kroonenberg, A., Magliulo, V., Martin, S., Martinez, D., Mastrotillo, L., Moene, A. F., Molinos, F., Moulin, E., Pietersen, H. P., Pignatelli, B., Pique, E., Román-Cascón, C., Rufin-Soler, C., Saïd, F., Sastre-Marugán, M., Seity, Y., Steeneveld, G. J., Toscano, P., Traullé, O., Tzanos, D., Wacker, S., Wildmann, N., and Zaldei, A.: The BLLAST field experiment: Boundary-Layer Late Afternoon and Sunset Turbulence, *Atmos. Chem. Phys.*, 14, 10931–10960, [https://doi.org/10.5194/acp-14-10931-](https://doi.org/10.5194/acp-14-10931-2014) 20 2014, 2014.
- Luo, L., Ma, W., Zhao, W., Zhuang, Y., Zhang, Z., Zhang, M., Ma, D., and Zhou, Q.: UAV-based spatiotemporal thermal patterns of permafrost slopes along the Qinghai-Tibet Engineering Corridor, *Landslides*, 15, 2161–2172, 2018.
- Mahrt, L.: Modelling the depth of the stable boundary-layer, *Bound.-Lay. Meteorol.*, 21, <https://doi.org/10.1007/BF00119363>, 1981.

- Mahrt, L.: Stratified atmospheric boundary layers, *Bound.-Lay. Meteorol.*, 90, 375–396, <https://doi.org/10.1023/A:1001765727956>, 1999.
- 25 Mahrt, L. and Vickers, D.: Formulation of turbulent fluxes in the stable boundary layer, *J. Atmos. Sci.*, 60, 2538–2548, [https://doi.org/10.1175/1520-0469\(2003\)060<2538:FOTFIT>2.0.CO;2](https://doi.org/10.1175/1520-0469(2003)060<2538:FOTFIT>2.0.CO;2), 2003.
- Mahrt, L. and Vickers, D.: Boundary-layer adjustment over small-scale changes of surface heat flux, *Bound.-Lay. Meteorol.*, 116, 313–330, <https://doi.org/10.1007/s10546-004-1669-z>, 2005.
- Mahrt, L. and Vickers, D.: Extremely weak mixing in stable conditions, *Bound.-Lay. Meteorol.*, 119, 19–39, <https://doi.org/10.1007/s10546-005-9017-5>, 2006.
- Mäkiranta, E., Vihma, T., Sjöblom, A., and Tastula, E.-M.: Observations and modelling of the atmospheric boundary layer over sea-ice in a Svalbard Fjord, *Bound.-Lay. Meteorol.*, 140, 105–123, <https://doi.org/10.1007/s10546-011-9609-1>, 2011.
- Malamiri, H. R. G., Rousta, I., Olafsson, H., Zare, H., and Zhang, H.: Gap-filling of MODIS time series Land Surface Temperature (LST) products using Singular Spectrum Analysis (SSA), *Atmosphere-Basel*, 9, 334, 2018.
- 5 Malbêteau, Y., Parkes, S., Aragon, B., Rosas, J., and McCabe, M. F.: Capturing the diurnal cycle of land surface temperature using an unmanned aerial vehicle, *Remote Sens-Basel*, 10, 1407, 2018.
- Mallast, U. and Siebert, C.: Combining continuous spatial and temporal scales for SGD investigations using UAV-based thermal infrared measurements, *Hydrol. Earth Syst. Sci.*, 23, 1375–1392, 2019.
- 10 Manoj, K. K., Tang, Y., Deng, Z., Chen, D., and Cheng, Y.: Reduced-rank sigma-point Kalman filter and its application in ENSO model, *J. Atmos. Ocean. Tech.*, 31, 2350–2366, <https://doi.org/10.1175/JTECH-D-13-00172.1>, 2014.
- Martikainen, A., Dougherty, H., Taylor, C., and Mazzella, A.: Sonic anemometer airflow monitoring technique for use in underground mines, In: *Proceedings of the 13th U.S./North American mine ventilation symposium*, Sudbury, Ontario, Canada, June 2010, 2010.
- Martin, S., Bange, J., and Beyrich, F.: Meteorological profiling of the lower troposphere using the research UAV "M²AV Carolo", *Atmos. Meas. Tech.*, 4, 705–716, <https://doi.org/10.5194/amt-4-705-2011>, 2011.
- 15 Martiny, M., Schiele, R., Gritsch, M., Schulz, A., and Wittig, S.: In situ calibration for quantitative infrared thermography, *Quant. Infr. Therm. J.*, 1996.
- Mayer, S., Sandvik, A., Jonassen, M., and Reuder, J.: Atmospheric profiling with the UAS SUMO: a new perspective for the evaluation of fine-scale atmospheric models, *Meteorol. Atmos. Phys.*, 116, 15–26, <https://doi.org/10.1007/s00703-010-0063-2>, 2012.
- 20 Medeiros, L. E. and Fitzjarrald, D. R.: Stable boundary layer in complex Terrain. Part I: Linking fluxes and intermittency to an average stability index, *J. Appl. Meteorol. Clim.*, 53, 2196–2215, <https://doi.org/10.1175/JAMC-D-13-0345.1>, 2014.
- Medeiros, L. E. and Fitzjarrald, D. R.: Stable boundary layer in complex terrain. Part II: Geometrical and sheltering effects on mixing, *J. Appl. Meteorol. Clim.*, 54, 170–188, <https://doi.org/10.1175/JAMC-D-13-0346.1>, 2015.

- Murray, B., Anderson, D. T., Wescott, D. J., Moorhead, R., and Anderson, M. F.: Survey and insights into unmanned aerial-vehicle-based
25 detection and documentation of clandestine graves and human remains, *Hum. Biol.*, 90, 45–61, 2018.
- Obukhov, A. M.: Turbulence in an atmosphere with a non-uniform temperature, *Bound.-Lay. Meteorol.*, 2, 7–29,
<https://doi.org/10.1007/BF00718085>, 1971.
- Olbrycht, R. and Więcek, B.: New approach to thermal drift correction in microbolometer thermal cameras, *Quant. Infr. Therm. J.*, 12,
184–195, 2015.
- 30 Padró, J.-C., Muñoz, F.-J., Planas, J., and Pons, X.: Comparison of four UAV georeferencing methods for environmental monitoring pur-
poses focusing on the combined use with airborne and satellite remote sensing platforms, *Int. J. Appl. Earth Obs.*, 75, 130–140, 2019.
- Palomaki, R. T., Rose, N. T., van den Bossche, M., Sherman, T. J., and De Wekker, S. F. J.: Wind Estimation in the Lower Atmosphere Using
Multirotor Aircraft, *J. Atmos. Ocean. Tech.*, 34, 1183–1191, <https://doi.org/10.1175/JTECH-D-16-0177.1>, 2017.
- Pichugina, Y. L., Tucker, S. C., Banta, R. M., Brewer, W. A., Kelley, N. D., Jonkman, B. J., and Newsom, R. K.: Horizontal-velocity and
5 variance measurements in the stable boundary layer using doppler lidar: sensitivity to averaging procedures, *J. Atmos. Ocean. Tech.*, 25,
1307–1327, <https://doi.org/10.1175/2008JTECHA988.1>, 2008.
- Poblete, T., Ortega-Fafias, and Ryu, D.: Automatic coregistration algorithm to remove canopy shaded pixels in UAV-borne thermal images
to improve the estimation of crop water stress index of a drip-irrigated cabernet sauvignon vineyard, *Sensors-Basel*, 18, 397, 2018.
- Pollard, R. T.: The Joint Air-Sea Interaction Experiment—JASIN 1978, *B. Am. Meteorol. Soc.*, 59, 1310–1318, <https://doi.org/10.1175/1520->
10 0477-59.10.1310, 1978.
- Rahaghi, A. I., Lemmin, U., Sage, D., and Barry, D. A.: Achieving high-resolution thermal imagery in low-contrast lake surface waters by
aerial remote sensing and image registration, *Remote Sens. Environ.*, 221, 773–783, 2019.
- Remondino, F., Barazzetti, L., Scaioni, M., and Sarazzi, D.: UAV photogrammetry for mapping and 3D modeling - current status and future
perspectives, in: *Int. Arch. Photogramm. Remote Sens. Spatial Inf. Sci.*, XXXVIII-1/C22, pp. 25–31, 2011.
- 15 Ribeiro-Gomes, K., Hernández-López, D., Ortega, J. F., Ballesteros, R., Poblete, T., and Moreno, M. A.: Uncooled thermal camera calibration
and optimization of the photogrammetry process for UAV applications in agriculture, *Sensors-Basel*, 17, 2173, 2017.
- Rotach, M. W. and Zardi, D.: On the boundary-layer structure over highly complex terrain: Key findings from MAP, *Q. J. Roy. Meteor. Soc.*,
133, 937–948, <https://doi.org/10.1002/qj.71>, 2007.
- Roth, M.: Review of atmospheric turbulence over cities, *Q. J. Roy. Meteor. Soc.*, 126, 941–990, <https://doi.org/10.1002/qj.49712656409>,
20 2000.
- Sagan, V., Maimaitijiang, M., Sidike, P., Eblimit, K., Peterson, K. T., Hartling, S., Esposito, F., Khanal, K., Newcomb, M., Pauli, D., Ward, R.,
Fritschi, F., Shakoor, N., and Mockler, T.: UAV-Based high resolution thermal imaging for vegetation monitoring and plant phenotyping
using ICI 8640 P, FLIR Vue Pro R 640 and thermoMap cameras, *Remote Sens-Basel*, 11, 330, 2019.

- Satirapod, C., Trisirisatayawong, I., and Homniam, P.: Establishing ground control points for high-resolution satellite imagery using GPS precise point positioning, in: 2003 IEEE International Geoscience and Remote Sensing Symposium. Proceedings, pp. 4486–4488, 2003.
- 25 Schmit, T. J., Griffith, P., Gunshor, M. M., Daniels, J. M., Goodman, S. J., and J., L. W.: A closer look at the ABI on the GOES-R series, *B. Am. Meteorol. Soc.*, 98, 681–698, 2017.
- Sheng, H., Chao, H., Coopmans, C., Han, J., McKee, M., and Chen, Y. Q.: Low-cost UAV-based thermal infrared remote sensing: platform, calibration and applications, in: Proceedings of 2010 IEEE/ASME International Conference on Mechatronic and Embedded Systems and Applications, pp. 38–43, 2010.
- 30 Shin, H. H., Hong, S.-Y., Noh, Y., and Dudhia, J.: Derivation of turbulent kinetic energy from a first-Order nonlocal planetary boundary layer parameterization, *J. Atmos. Sci.*, 70, 1795–1805, <https://doi.org/10.1175/JAS-D-12-0150.1>, 2013.
- Smith, F. B.: An analysis of vertical wind-fluctuations at heights between 500 and 5,000 ft, *Q. J. Roy. Meteor. Soc.*, 87, 180–193, <https://doi.org/10.1002/qj.49708737207>, 1961.
- 5 Smith, G. M. and Milton, E. J.: The use of the empirical line method to calibrate remotely sensed data to reflectance, *Int. J. Remote Sens.*, 13, 2653–2662, 1999.
- Stuedler, P. A., Melillo, J. M., Bowden, R. D., Castro, M. S., and Lugo, A. E.: The effects of natural and human disturbances on soil nitrogen dynamics and trace gas fluxes in a Puerto Rican wet forest, *Biotropica*, 23, 356–363, <https://doi.org/10.2307/2388252>, 1991.
- Stevens, W. R., Squier, W., Mitchell, W., Gullett, B. K., and Pressley, C.: Measurement of motion corrected wind velocity using an aerostat lofted sonic anemometer, *Atmos. Meas. Tech. Discussions*, 6, 703–720, <https://doi.org/10.5194/amtd-6-703-2013>, 2013.
- 10 Stull, R. B.: An introduction to boundary layer Meteorology, Kluwer Academic Publishers, Dordrecht, The Netherlands, 1988.
- Stull, R. B.: Practical Meteorology: An Algebra-based Survey of Atmospheric Science, Univ. of British Columbia, 2015.
- Svensson, G., Holtslag, A. A. M., Kumar, V., Mauritsen, T., Steeneveld, G. J., Angevine, W. M., Bazile, E., Beljaars, A., de Bruijn, E. I. F., Cheng, A., Conangla, L., Cuxart, J., Ek, M., Falk, M. J., Freedman, F., Kitagawa, H., Larson, V. E., Lock, A., Mailhot, J., Masson, V., Park, S., Pleim, J., Söderberg, S., Weng, W., and Zampieri, M.: Evaluation of the diurnal cycle in the atmospheric boundary layer over land as represented by a variety of single-column models: The second GABLS experiment, *Bound.-Lay. Meteorol.*, 140, 177–206, <https://doi.org/10.1007/s10546-011-9611-7>, 2011.
- 15 Tempelhahn, A., Budzier, H., Krause, V., and Gerlach, G.: Shutter-less calibration of uncooled infrared cameras, *J. Sens. Sens. Syst.*, 5, 9–16, 2016.
- 20 Thompson, N.: Turbulence measurements over the sea by a tethered-balloon technique, *Q. J. Roy. Meteor. Soc.*, 98, 745–762, <https://doi.org/10.1002/qj.49709841804>, 1972.
- Thompson, N.: Tethered Balloons, In: Dobson F., Hasse L., Davis R. (eds) *Air-Sea Interaction*. Springer, Boston, MA, pp. 589–604, https://doi.org/10.1007/978-1-4615-9182-5_32, 1980.

- Tomlinson, C. J., Chapman, L., Thornes, J. E., and Baker, C.: Remote sensing land surface temperature for meteorology and climatology: a review, *Meteorol. Appl.*, 18, 296–306, 2011.
- Turner, D., Lucieer, A., and Wallace, L.: Direct georeferencing of ultrahigh-resolution UAV imagery, *IEEE T. Geosci. Remote*, 52, 2738–2745, 2014.
- Usamentiaga, R., Venegas, P., Guerediaga, J., Vega, L., Molleda, J., and Bulnes, F. G.: Infrared thermography for temperature measurement and Non-destructive testing, *Sensors*, 14, 12 305–12 348, <https://doi.org/10.3390/s140712305>, 2014.
- Verykokou, S. and Ioannidis, C.: Oblique aerial images: a review focusing on georeferencing procedures, *Int. J. Remote Sens.*, 39, 3452–3496, 2018.
- Vierling, L. A., Fersdahl, M., Chen, X., Li, Z., and Zimmerman, P.: The Short Wave Aerostat-Mounted Imager (SWAMI): A novel platform for acquiring remotely sensed data from a tethered balloon, *Remote Sens. Environ.*, 103, 255–264, 2006.
- Wan, Z., Hook, S., and Hulley, G.: MOD11B3 MODIS/Terra land surface temperature/emissivity monthly L3 global 6 km SIN grid V006, [Data set], NASA EOSDIS LP DAAC, <https://doi.org/10.5067/MODIS/MOD11B3.006>, 2015.
- Wang, K., Wan, Z., Wang, P., Sparrow, M., Liu, J., Zhou, X., and Haginoya, S.: Estimation of surface long wave radiation and broadband emissivity using Moderate Resolution Imaging Spectroradiometer (MODIS) land surface temperature/emissivity products, *J. Geophys. Res.-Atmos.*, 110, <https://doi.org/10.1029/2004JD005566>, 2005.
- Weng, Q.: Remote sensing of impervious surfaces in the urban areas: requirements, methods, and trends, *Remote Sens. Environ.*, 117, 34–49, 2012.
- Whitehead, K., Hugenholtz, C. H., Myshak, S., Brown, O., LeClair, A., and Tamminga, A.: Remote sensing of the environment with small unmanned aircraft systems (UASs), part 2: scientific and commercial applications., *Journal of Unmanned Vehicle Systems*, 2, 86, 2014.
- Wilson, J. D.: Monin-Obukhov functions for standard deviations of velocity, *Bound.-Lay. Meteorol.*, 129, 353–369, 2008.
- Zeise, B. and Wagner, B.: Temperature correction and reflection removal in thermal images using 3D temperature mapping, In *Proceedings of the 13th International Conference on Informatics in Control, Automation and Robotics*, 2, 158–165, <https://doi.org/10.5220/0005955801580165>, 2016.
- Zeise, B., Kleinschmidt, S. P., and Wagner, B.: Improving the interpretation of thermal images with the aid of emissivity’s angular dependency, in: *2015 IEEE International Symposium on Safety, Security and Rescue Robotics (SSRR)*, pp. 1–8, 2015.
- Zhong, Y., Xu, Y., Wang, X., Jia, T., Ma, A., and Zhang, L.: Pipeline leakage detection for district heating systems using multisource data in mid- and high-latitude regions, *ISPRS J. Photogramm.*, 151, 207–222, 2019.
- Zhuo, X., Koch, T., Kurz, F., Fraundorfer, F., and Reinartz, P.: Automatic UAV image geo-registration by matching UAV images to georeferenced image data, *Remote Sens-Basel*, 9, 376, 2017.

910 Zilitinkevich, S. and Baklanov, A.: Calculation of the height of the stable boundary layer in practical applications, *Bound.-Lay. Meteorol.*, 105, 389–409, <https://doi.org/10.1023/A:1020376832738>, 2002.